Summer 8-7-2012

Stability Analysis of Phase-Locked Bursting in Inhibitory Neuron Networks

Sajiya Jesmin Jalil
Georgia State University

STABILITY ANALYSIS OF PHASE-LOCKED BURSTING IN INHIBITORY NEURON NETWORKS

by

SAJIYA JALIL

Under the Direction of Drs. Igor Belykh and Andrey Shilnikov

ABSTRACT

Networks of neurons, which form central pattern generators (CPGs), are important for controlling animal behaviors. Of special interest are configurations or CPG motifs composed of reciprocally inhibited neurons, such as half-center oscillators (HCOs). Bursting rhythms of HCOs are shown to include stable synchrony or in-phase bursting, which is a phase-locked state that has zero phase difference. This in-phase bursting can co-exist with anti-phase bursting, commonly expected as the single stable state in HCOs that are connected with fast non-delayed synapses. The finding contrasts with the classical view that reciprocal inhibition has to be slow or time-delayed to synchronize such bursting neurons. Phase-locked rhythms are analyzed via Lyapunov exponents estimated with variational equations, and through the convergence rates estimated with Poincaré return maps. A new mechanism underlying multistability is proposed that is based on the spike interactions, which confer a dual property on the fast non-delayed reciprocal inhibition; this reveals the role of spikes in generating multiple co-existing phase-locked rhythms. In particular, it demonstrates that the number and temporal characteristics of spikes determine the number and stability of the multiple phase-locked states in weakly coupled HCOs. The generality of the multistability phenomenon is demonstrated by analyzing

diverse models of bursting networks with various inhibitory synapses; the individual cell models include the reduced leech heart interneuron, the Sherman model for pancreatic beta cells, the Purkinje neuron model and Fitzhugh-Rinzel phenomenological model. Finally, hypothetical and experiment-based CPGs composed of HCOs are investigated, and predictions that may be verified by electrophysiologists studying the sensory-motor systems are made. This study is relevant for various applications that use CPGs such as robotics, prosthetics, and artificial intelligence.

INDEX WORDS: Bursting, Central pattern generator, Fast threshold modulation, Half-center oscillator, Inhibition, Lyapunov exponents, Multistability, Networks, Neurons, Phase-locking, Poincaré return maps, Synchrony, Variational equations

STABILITY ANALYSIS OF PHASE-LOCKED BURSTING IN INHIBITORY NEURON NETWORKS

by

SAJIYA JALIL

A Dissertation Submitted in Partial Fulfillment of the Requirements for the Degree of

Doctor of Philosophy

in the College of Arts and Sciences

Georgia State University

2012

STABILITY ANALYSIS OF PHASE-LOCKED BURSTING IN INHIBITORY NEURON NETWORKS

by

SAJIYA JALIL

Committee Chair: Dr. Andrey Shilnikov

Committee: Dr. Igor Belykh

Dr. Vladimir Bondarenko

Dr. Robert Clewley

Electronic Version Approved:

Office of Graduate Studies

College of Arts and Sciences

Georgia State University

August 2012

DEDICATION

Dedicated to my daughter Raida Anonnah, husband Faisal As-Safa, parents Arjumand Shaheda and Abdul Jalil.

ACKNOWLEDGEMENTS

I thank my advisers Drs. Igor Belykh and Andrey Shilnikov, and committee members Drs. Vladimir Bondarenko and Rob Clewley for their support and guidance. This work was supported by the GSU Brains and Behavior program, jointly offered by the department of Mathematics & Statistics, and the Neuroscience Institute. Other funding agencies, namely RFFI grants No 050100558, No 09-01-00498-a, No. 2100-065268, No. 08-01-00083, and NSF grant DMS-1009744, DMS-1009591. I would like to thank the Shilnikov lab members and associates Dane Allen, Paul Channel, Bryce Chung, Enis Gunay, Aaron Kelley, Justus Schwabedal, Jeremy Wojcik, Tingli Xing, Joe Youker, and Kristie Young for offering various helpful comments and technical supports; as well as, Tasnuva Jhileek for proof reading. Finally, I thank numerous faculty and staff members, friends and family members who have made themselves available for supporting in various capacities.

TABLE OF CONTENTS

LIST OF TABLES

LIST OF FIGURES

LIST OF ABBREVIATIONS

- 1-D - one dimensional
- 2-D - two dimensional
- 3-D - three dimensional
- Burster - a model or a neuron that can generate bursting behavior
- Bursting behavior - voltage traces consisting of spiking and silent phases
- CPG - central pattern generator
- Depolarized - highly positive or positive change in the membrane potential
- Elliptic burster - silent phase above minimum and below maximum level of spikes
- FTM - fast threshold modulation
- HCO - half center oscillator
- Hyperpolarized - highly negative or negative change in the membrane potential
- Lyapunov exponents - a measure of separation between solution trajectories over time
- Monotonic - lacks oscillation; either increases or decreases but not both
- Network cycle - the period of time needed for the network to repeat an activity pattern
- ODEs - ordinary differential equations
- Phase-locked - constant time delay between spikes of different neurons
- Silent phase - hyperpolarized voltage trace with small or no oscillations
- Square wave burster - silent phase below minimum level of spikes

- Synchrony - identical patterns generated by different neurons
- Variational equations - a system of ODEs that measures variations in the variables from synchrony

Chapter 1

INTRODUCTION

Neurons, composing the nervous system of an animal, are highly specialized cells. These cells, unlike most other cells, show electrical activities. They have many projections that are similar to wires and are capable of passing on the electrical signals to each other. The paradigm for mathematically capturing these electrical activities was introduced in the 1950s by two scientists, namely Alan L. Hodgkin and Andrew Huxley. Following their electrophysiological studies and the proposed mathematical model of the activities of the neurons, there has been much development in the areas of computational and mathematical neuroscience. Mathematical quantities including the rates of changes or the time scales of the flow of ions in the neurons are now used to categorize diverse groups of neurons. A system of ordinary differential equations (ODEs), obtained from these measures, represent an individual neuron, and can be used to study network functions and mechanisms.

Animal behaviors are thought to be controlled by networks of neurons. In particular, groups of neurons can be found that demonstrate correlated electrical activities during the behavior. Such groups are connected in some fashion forming networks, called the central pattern generators (CPGs). A CPG produces specific activity pattern without any external stimulation, and if any of the neurons in the group is removed the pattern is lost. While identifying a CPG is not a trivial task, use of mathematical and computational techniques provide neuroscientists with additional tools to study the functions of CPGs.

In 1911, T. G. Brown suggested a specific network configuration, underlying behaviors that are composed of alternating rhythms such as locomotion. He coined the term half-center oscillator (HCO) to describe a CPG type network that have two components and inhibit each other while active. Since then many CPGs have been identified that contain HCOs as component subnetworks. HCO produces alternating activities as each half of the network ensures the other half is inactive. At the same time, both halves

can participate, but only by taking turns. With the advent of electrophysiological tools, such alternating activities can be seen in the simultaneous recordings made from multiple neurons. Furthermore, connections between neurons can be distinguished as inhibitory or not. As a result, reciprocal inhibition between two neurons, forming a half-center oscillator, has been under intense investigation.

Studies of model half-center oscillators are rich with mathematical analysis of the differential equations representing the network. Alternating rhythm is contrasted with synchronous rhythm, where activities of the neurons in the network perfectly coincide. Using low dimension ODEs, the classical theory proves that under the most general conditions, alternating rhythm is robust while synchronous rhythm is unstable in the HCO networks. The research presented in this discourse is an extension of the classical theory. When ODEs of higher dimension is used, it is found that synchronous rhythm is robust along with the alternating one. Furthermore, rhythms with intermediate delays or correlations have been observed and found to be stable. Since any behavior of an animal can be decomposed into a number of simpler activity patterns that may be sequentially active with various delays, the underlying mechanisms are important to understand.

In this study, stability of multiple coexisting rhythms in the HCO networks has been analyzed using mathematical and computational tools. These rhythms, in general, are referred as the phase-locked states of the network. ODEs that are complex enough to capture bursting behavior of neurons are used to study the stability properties of phase-locked bursting in the inhibitory neuron networks. Insights gained are used to analyze and predict plausible mechanisms of an experiment-based CPG from the invertebrate *Melibe leonina*. The broader implication of this study is that electronic circuits designed with the ODEs may be used to control useful machines similar to how CPGs control animal behaviors.

1.1 Background

Ordinary differential equations capture natural phenomena rather accurately in many cases. ODEs represent dynamical systems that have quantities evolving in time.

Electrical properties of neurons, for example, may oscillate frequently, in time, between two states separated by high amplitudes, producing patterns known as spikes. They can also spike intermittently, alternating with a third state, composing bursts [1, 2]. Bursts are characterized in experiments. These experiments are meant to reveal underlying mechanisms of various behaviors and nervous functions in animals. When neurons produce complex behaviors, their network interaction is often monitored by emergence of synchrony and other types of robust correlated activities known as phase-locking or phase-locked states[3–6]. To study the phase-locked bursting activities, the following mathematical tools are used: systems of ordinary differential equations, equilibriums or steady states, nullclines, bifurcations, variational equations, stability, Lyapunov exponents, phases and phase differences [7–11]. The discourse is organized as follows, introduction, models and methods, spike synchrony analysis, burst synchrony analysis, experimental network analysis, and finally, conclusions and future directions followed by references and appendices.

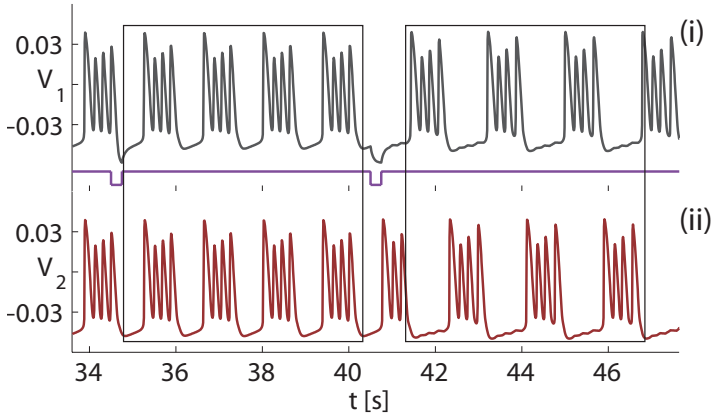

Figure 1.1. Voltage traces showing synchrony (left box) and anti-phase bursting (right box) rhythms.

Chapter 1 gives a broad view of the research embodied in this discourse, the main hypothesis and the significance of this work along with some background knowledge. This study starts with the spike synchrony of the electrical signals between neurons, which is achieved when the signals recorded from each neuron over-

lap completely. The traces (recorded signals) after being superimposed appears identical. The left box in figure 1.1 shows voltage traces for a pair of neurons producing synchronous rhythm. The traces are shifted vertically, as otherwise they would be indistinguishable. To demonstrate that they are identical, traces are often plotted with respect to each other without the explicit time coordinate. Visualized this way, spike synchrony appears as a diagonal line as depicted in 1.2.1. Burst synchrony, on the other hand, appears in 1.2.2. In this case, the lower values of the membrane potential, which is the main variable recorded from neurons, are identical. The higher values, which correspond to the spiking patterns within the bursts, are slightly deviated.

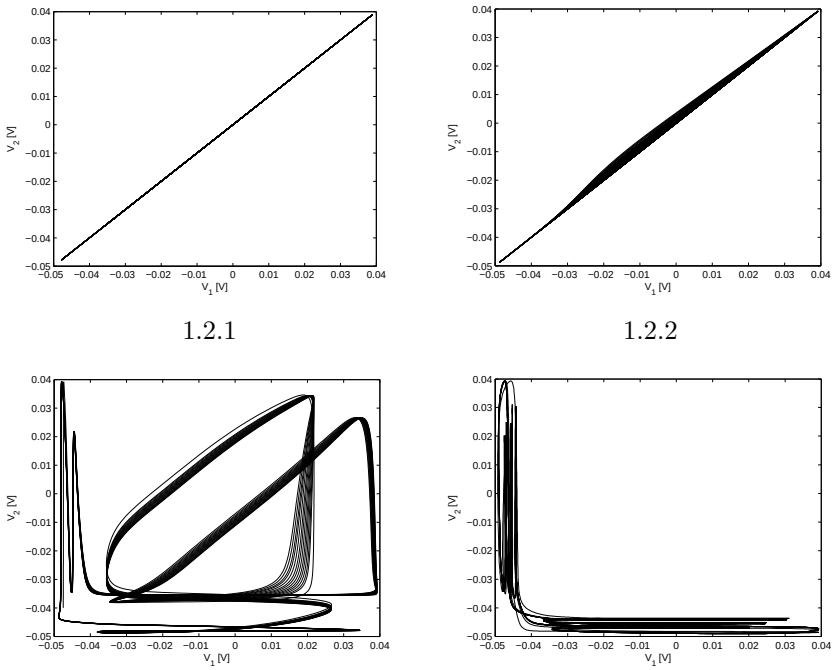

Figure 1.2. Visualization of in-phase ($\Delta\phi = 0$) spike (1.2.1) and burst (1.2.2), intermediate ($0 < \Delta\phi < 0.5$) phase-locked (1.2.3), and anti-phase ($\Delta\phi = 0.5$) synchrony (**??**) in the voltage plane for leech model HCOs. Phase-lag, $\Delta\phi$ is measured at the left bottom corner, when either V_1 or V_2 is -0.042 V. Spike synchrony is measured by maximum absolute difference of membrane potentials, $|V_1 - V_2|$, which is reflected by distance from the diagonal.

In chapter 2, details of the models, relevant concepts and descriptions of procedures are presented. The various phase locked rhythms are quantified and represented by constant differences between phases, ϕ. The definitions of phases, ϕ

and phase differences, $\Delta\phi$, can be found in chapter 2, and the pseudo code for the algorithm used to compute $\Delta\phi$ can be found in appendix B. The traces for rhythms that have intermediate delays between the active (spiking) states of the neurons are shown in figure 1.3. While synchronous and anti-phase rhythms have diagonal and L-shaped configurations in the $V_1 - V_2$ plane, other phase-locked rhythms are mixtures of both. Naturally, the later rhythms have zones where electrical activity is nearly identical or far from it. The two types of zones cause the mixture configuration; for example see figure 1.2.3.

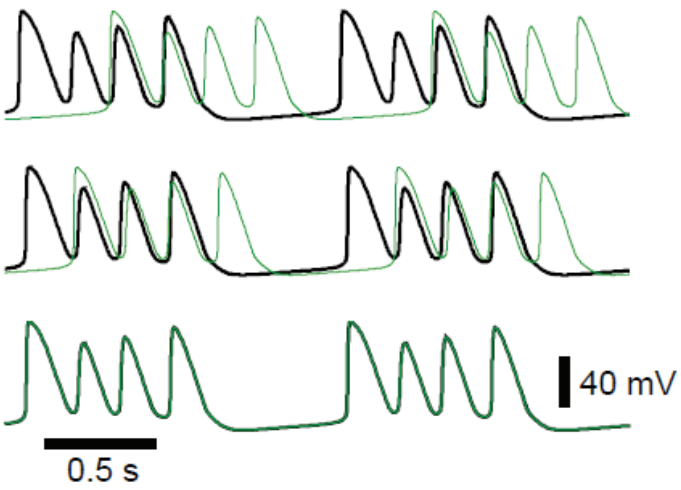

Figure 1.3. Voltage traces showing rhythms with intermediate delays between active states of neurons. Generally, these rhythms are known as phase-locked bursting patterns.

There are *mathematical abstractions that correlate with different types of neuron generated patterns.* Neurons are classified according to their electrical activities. Although spikes are present in bursting traces, some neurons are only capable of spiking or bursting, while others can generate both types of activities. In addition, neurons can be silent, meaning no oscillatory activity may be present in the traces. For a system of ODE represented by (1.1) a function $\mathbf{x}(t)$ is considered a solution if it satisfies the rates of change (indicated by $'$ or $\dot{}$) equations given by the system. A non-oscillatory pattern produced by the neuron is a constant function, and an oscillatory pattern such as spiking

or bursting is a periodic function; moreover, these patterns are solutions to the ODEs, constructed from the measurements of the neuron, given by the expression $\mathbf{f}(\mathbf{x})$.

$$\mathbf{x}' = \mathbf{f}(\mathbf{x}) \tag{1.1}$$

The boldfaced characters used in the equation (1.1) represent a number of variables and functions tabulated in the form of vectors. In other words, $\mathbf{f}$ is a vector of functions, while $\mathbf{x}$ is a vector of variables. Once the functions $\mathbf{f}(\mathbf{x})$ have been crafted, and the variables $\mathbf{x}$ have been selected based on the experiments, mathematical analysis of the ODEs and computational experiments have proven to be useful in providing insights into the underlying principles that govern neurons. Hence, there is a demand for further development of mathematical and computational tools for research in neuroscience.

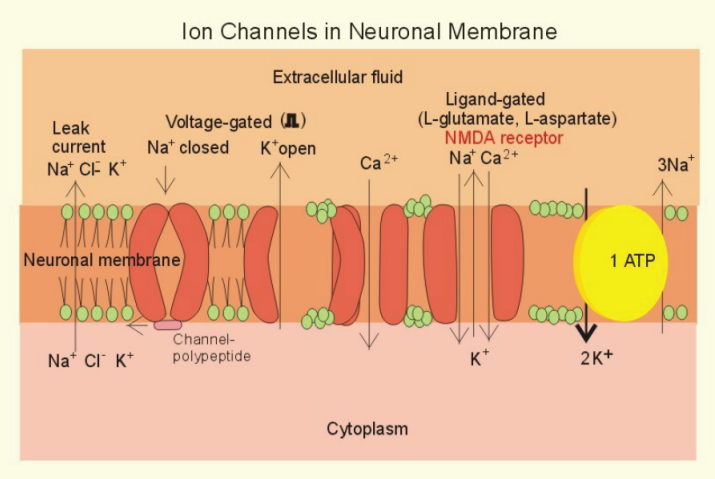

Figure 1.4. Schematic depiction of processes at the neuron membrane producing electrical activity, reproduced from [12]. Here, most common ions are shown: sodium (Na), chloride (Cl), potassium (K), calcium (Ca). Neuron's membrane is composed of special molecules depicted in green. Channels and receptors are made of proteins and sugars, shown here as orange cylindrical objects. Activities of these molecules may be dependent on membrane potential, or other molecules, known referred as their ligands. ATP stands for Adenosine Tri-Phosphate, which is the energy releasing molecule.

There has been much research exploring *the causes and the meaning of electrical signals in neurons.* Neurons or other cells capable of electrical activities have reservoirs of various ions, such as sodium, potassium, chloride, calcium and so on. The charges on

these ions retain the ability to cause electricity as they move between the interior and the exterior portions of the neurons. The amplitude of the electrical activity is dictated by the concentration of these ions. The specific distributions of various ions correspond to membrane potential that drives the electrical activities. In other words, neurons or cells control their electrical activity by controlling the distribution of ions [13]. Figure 1.4 shows schematic representation of some of the processes.

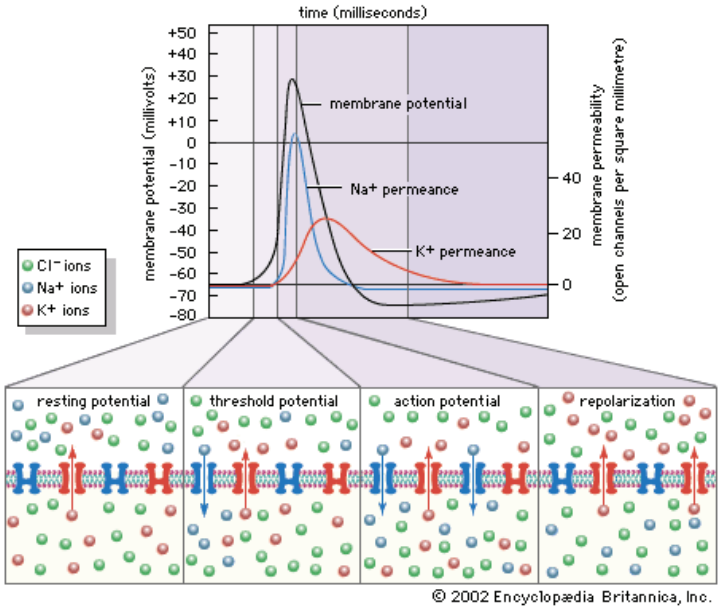

Figure 1.5. Action potential resulting from ion transport at specific time scales. Membrane potential depolarize (increase) following shortly after opening of channels that raises sodium permeability; on the other hand, it hyperpolarize (decrease) when permeability of potassium changes allowing the ion to leave the intracellular space. Figure reproduced from Encyclopedia Britannica.

The use of ordinary differential equations to model electrical activities of a neuron was first introduced by Nobel laureates Hodgkin and Huxley, in their seminal papers, studying the electrophysiology of the squid's giant axon [14, 15]. Neurons propagate electrical signals over long distances through their axons and dendrites. These projections of neurons contain large numbers of channels (pores) that are capable of transporting ions across the membrane, which separates the interior of the neurons from the exterior. Many channels require energy produced via dephosphorylation of Adenosine Tri-Phosphate

(ATP), or other conditions to transport ions. In general, channels activate (open) or inactivate (close) depending on the voltage potential across the membrane. Depending on the specific distribution of ions maintained by the neurons, certain ions typically flow either in or out when their corresponding channels activate, creating inward or outward flow of currents. By convention, flow of positive charge indicates the inward or the outward currents. In other words, inward current is the flow of positive charge into the cell, or equivalently, the flow of negative charge out of the cell; outward current is the reverse flow. Furthermore, by convention, inward currents result in depolarization (rise in the positive direction) and outward currents result in hyperpolarization (lower in the negative direction) of the membrane potential [16]. Hodgkin and Huxley proposed the

$$\frac{dV}{dt} = -\frac{1}{C_M}\{\bar{g}_K n^4 (V - V_K) + \bar{g}_{Na} m^3 h (V - V_{Na}) + \bar{g}_l (V - V_l)\}$$

Figure 1.6. The original Hodgkin-Huxley equation for the membrane potential, reproduced from [14].

ODE shown in figure 1.6 to model the membrane potential of a neuron. It has a number of expressions defining the ionic contributions. In this model, a number of variables and parameters are introduced along with V, the membrane potential. Conductances, $\bar{g}_x$, and reversal potentials, V_x, specific to two of the major ion species are included as the experimentally measured parameters. Probability variables m, n, h, which define the rates of transport of the ions across the membrane are introduced. Variables are functions of time whereas parameters are time independent constants. Further details for these type of models and their interpretations can be found in the chapter 2.

The types of *networks, considered in the study, are formed by neurons that can elicit electrical responses in each other.* This interaction can be caused directly by the flow of ions between neurons (gap juctions/electrical synapses) or indirectly by neurotransmitter signals (chemical synapses). The synapses are further classified into excitatory

(depolarize membrane potential) or inhibitory (hyperpolarize membrane potential). Figure 1.7.1 shows changes in the membrane potentials of the post-synaptic neurons for the two types of synapses. It is also possible for synapses to have the capacity to function as both excitatory and inhibitory connections. In this study, models that approximate chemical synapses are used. Among these models are Heaviside, fast threshold modulatory (FTM), alpha-, and leech dynamical synapses. First three are phenomenological, meaning they approximate signature electrical properties of the synapses, and the fourth includes mechanistic details of the synapses. Regardless of the paradigm, all of the model synapses are quite fast. This means that the post-synaptic potentials, elicited in response to pre-synaptic spikes, decay as fast as the spikes. In contrast, slow synapses have longer lasting post-synaptic potentials. The mathematical function used for a fast synaptic con-

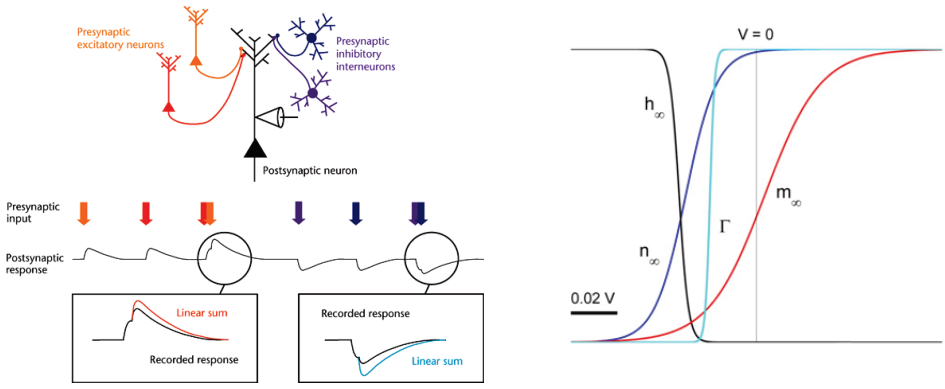

1.7.1 1.7.2

Figure 1.7. Figure (1.7.1), reproduced from [17], showing post-synaptic potentials may be hyperpolarizing (inhibitory) or depolarizing (excitatory). In (1.7.2), graphs of functions used to generate action potentials in the neuron models, and fast threshold modulatory function, Γ used for synaptic connections, are shown. The voltage depended probabilities, $n_\infty, h_\infty, m_\infty$, representing the channel gates are modeled by Boltzmann functions, which transition between closed (zero) to open (one) state smoothly. Here, n, m are activating, that is for high values of membrane potential, V, these channels open; whereas, h is inactivating because this channel closes for high values of V.

nection is depicted in figure 1.7.2 and denoted by Γ. Compared to the functions used for generating action potentials in the neuron, Γ has the fastest transition from minimum to maximum value.

Reciprocal inhibition is a common and critical feature in various neuronal networks that regulate biological functions [3, 18–20]. Such networks, known as central pattern gen-

erators (CPGs) are polymorphic, meaning different configurations may serve the same function, and multifunctional, meaning same network may serve different functions under different conditions. CPGs govern various rhythmic activities including cardiac beating and locomotive behaviors such as walking, chewing, swimming, and so on [21–24]. Switching between behaviors can be attributed to switching between various attractors of a CPG network, where attractors are the dominant and stable patterns in the system, with specific rhythms and time scales associated with them. A dedicated CPG has a single attractor as opposed to a multifunctional CPG which has more than one attractor. The smallest network capable of possessing reciprocal inhibition is a pair of neurons, the half-center oscillator (HCO) [18], which sometimes operates as a CPG by itself, or more often belong to larger CPGs. The figure 1.8.1 is a stained brain tissue that reveals the

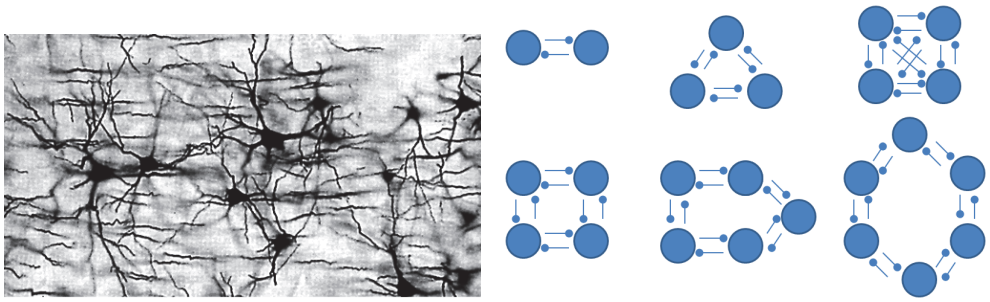

1.8.1 1.8.2

Figure 1.8. In (1.8.1), image of brain tissue stained with a dye show interconnectedness of the neurons, reproduced from [25]. In (1.8.2), schematic drawings of neuron networks show two levels of connectedness: global (top row) and local (bottom row). Large circles represent the neurons and round headed arrow indicated inhibitory synapses. Global networks have reciprocal inhibition between all pairs, local networks have reciprocal inhibition between only two neighbors. Local and global networks are the same for networks of two and three neurons.

projections of neurons that form connections with each other. A common strategy to study the brain mechanism or the functions of the nervous system is to study smaller networks such as those shown in 1.8.2. The idea is to understand the network behaviors theoretically, so that predictions can be made to verify the real mechanisms.

Many *behaviors are composite sequences of activities,* where one subset of activities completely suppresses another group of activities. For example, to move a leg during walking a group of muscles must be contracted to lift the leg, while the opposite group

must be inhibited or relaxed at the same time, allowing the lift. T. G. Brown originated the concept of the half-center oscillator in 1911 [18] while studying animal locomotives and their associated neuronal rhythms. Neurons in the half-center oscillators may not exhibit bursts of activity that alternate if dissociated from the network. This indicates the importance of formation of network and interaction between neurons in the network. In this discourse, the HCO is defined as a reciprocally inhibitory, two-neuron configuration that can produce anti-phase bursting. There are many studies that define mechanisms that generate bursting in individual and networked neurons [2, 26–29]. In particular, it has been shown that spiking and bursting behaviors may be regulated by slight perturbation of some critical parameter of the neuron.

In mathematical models, *time scales are essential for analyzing model behavior.* Multiple time scales are required to capture the stereotypical shape of action potentials in neurons (see figure 1.5). Existence and shapes of the spikes and bursts are closely tied to the number of time scales in the model. In addition, network interactions may be directed by the time scales. It has been shown that stable synchronous oscillations (traces boxed on the left, in figure 1.1) are not possible in reciprocally coupled networks of fast inhibitory *spiking* neurons [30, 31], unless each neuron has at least two slow intrinsic variables [32]. In other words, reciprocal inhibition is postulated to desynchronize neurons, if the inhibition is fast [33, 34]. Pre-synaptic neurons reliably take turn inhibiting the post-synaptic neurons because of reciprocal inhibition, leading to the phenomenon of anti-phase bursting (traces boxed on the right, in figure 1.1). The later pattern is strongly stable in the HCOs; hence the discovery that the former pattern can also be stable is of noteworthy.

In chapter 3, details of the spike synchrony analysis in bursting neuron networks is presented. Answer to the question, whether inhibition can synchronize fast non-delayed reciprocally connected bursting neurons, is amenable to mathematical analysis. Stability analysis of spike synchrony is possible by the use of variational equations because the system of ODEs in the neighborhood of synchronous manifold can be reduced [10]. This chapter demonstrates that numerical simulations of variational equations indicate spike synchrony in HCOs is stable, in a biologically relevant domain, in the

case of the fast non-delayed inhibition. A slowly decaying or a time-delayed inhibition, however, has been found previously to establish synchronization in the network by [35]. In addition, it was demonstrated that "inhibition not excitation" leads to synchronized firing, provided that reciprocal synapses are non-instantaneous and slow [33]. In these literatures, however, the time scales of the synapse required for synchronization excluded the fast and non-delayed condition.

For the purpose of studying HCOs with fast and non-delayed synapses, variational equations were used to analyze the stability of spike synchrony. In reality interactions between neurons in CPGs are highly nonlinear and nonhomogeneous as the neurons receive uncorrelated driving inputs from each other. As a result, novel patterns emerge due to network interactions [36]. When bursts are present, spike synchrony (figure 1.2.1) is a special case of in-phase burst synchrony (figure 1.2.2); the later form of synchrony is common in heterogeneous networks and cannot be detected by the variational equations. Larger networks that are homogeneous were investigated briefly using the variational equations. HCOs with slow synapses were also explored in this chapter, but without the use of variational equations.

In chapter 4, the concept of phases and phase differences are used to analyze the stability of burst synchrony in the HCO. Experiments show bursting patterns may be phase-locked during particular behaviors. For example, when swimming is initiated, recordings from swim interneurons show specific phase-lags, and it is distinct from the pattern seen for crawling [37]. In fact, constituent neurons from CPGs are distinguished by measuring phase relation between bursts generated by neurons in the network [3, 38]. Phases are defined by progression of the neuronal activity in terms of the percentage of one cycle of activity pattern. For a bursting neuron, one cycle is one complete burst and for spiking neuron, it is one complete spike. In other words, every time the activity pattern of a neuron repeats, it is a cycle. Period of a cycle is the time it takes for the pattern to recur (purple bars in figure 1.9). A convenient way to study multiple oscillatory units is to compare the phases by measuring phase differences (green bars in figure 1.9).

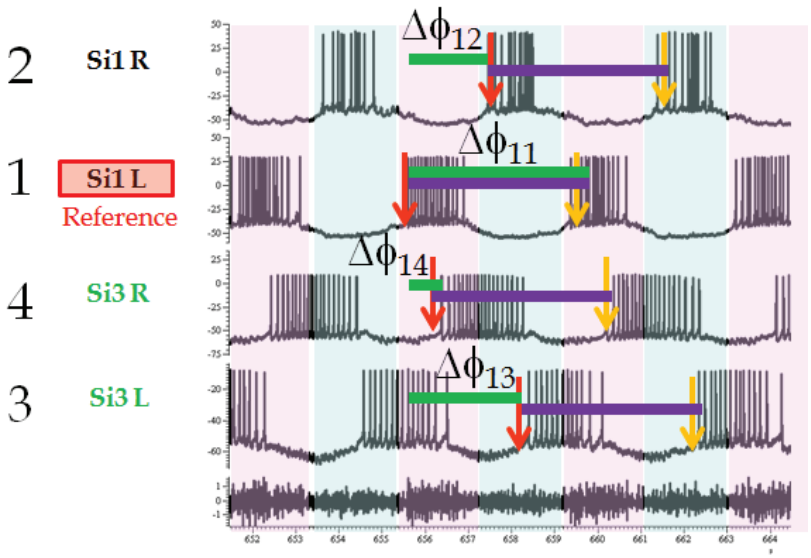

Figure 1.9. Phase differences compare the phases of activity pattern in CPG neurons. Traces are from [39]. Purple bars show periods, red and yellow arrows identifies beginning and ending of bursts, green bars show phase differences with respect to a reference neuron. Si stands for swim interneurons, L or R mean left or right side of the animal. $\Delta\phi$ denotes phase differences; subscripts identifies the neurons being compared.

A stunning feature of all CPGs is the burst synchrony: robust and stable timing of the constituent neurons' oscillatory rhythms [40, 41]. Figure 1.9 shows simultaneous recording from four neurons from the swim CPG of a marine invertebrate. The traces maintain specific timing among their bursts [39]. In an animal, a behavior often requires that groups of muscles act together and/or in specific sequences. For example, leech body wall muscles, grouped into twenty seven segments, engage in contraction in sequence to produced blood circulation. The bursting activities in the motor neurons in each segment show phase-lags, when compared to a reference neuron [3]. Large scale recordings show groups of neurons with bursting activities that are highly correlated within group and in specific phase relation among the groups [42]. There are several aspects to consider when seeking explanations for this generic and noticeable CPG phenomenon. These aspects include properties of individual neurons or neuronal models, types and time scales of synaptic coupling, as well as network architectures of CPGs. The stability analysis of burst synchrony is integral to the understanding of CPG functions [43–48]. A critical

question is whether there is one CPG dedicated for each activity or one multifunctional CPG capable of generating several behaviors. In this study, evidence for the multifunctional CPG is found.

In this chapter,weakly coupled HCOs are used to explain *how spike interactions due to reciprocal inhibition induce multiple stable phase-locked states.* Multiple stable phase-locked states imply multifunctional CPGs. The phenomenon of multistability has been reported in several cases of slow inhibitory [33, 34] and fast excitatory synapses [49, 50], and in this study, it is found in the case of fast, non-delayed inhibitory synapses. Diverse HCOs made of bursting neurons, such as leech heart interneurons [51], Sherman pancreatic β cells [52], Purkinje neurons [53], and the classical Fitzhugh-Rinzel phenomenological neurons are simulated. In addition, a number of different paradigms of fast, non-delayed synapses are employed. The results show that for a broad class of bursting neurons, burst synchrony and multistability are generic phenomena.

The effect of spike interactions are measured using phase differences. These phase differences, in turn, are measured using Poincaré sections mapping technique, which is a useful historic tool in the theory of dynamical systems. It measures how the phase changes after every cycle for a periodic solution of ODEs. In figure 1.10, the dashed horizontal lines represent location of the Poincaré sections. Instead of measuring phases of each neuron, the phase differences are measured directly from the time delay between the neurons at each Poincaré section. Stability diagrams for phase differences between bursts are constructed from the sequence $\Delta\phi^{(n)}$; an effective potential to quantify the stability of phase-locked states is introduced, such that its depths of wells correspond to robustness of stable states. The stability of in-phase bursting in strongly coupled HCOs, is also investigated for cases when variational equations are inapplicable.

In chapter 5, an experiment based CPG that includes two pairs of HCOs is examined. The CPG is for swimming behavior of the marine invertebrate *Melibe leonina*. Simultaneous recordings from four of the swim interneurons show phase-locked patterns (figure 1.9). While the biological preparation of the CPG includes excitatory and electrical coupling between some of the neurons, inhibitory coupling is more prevalent. In this study, starting with identical neuron models and coupling strengths, variation in

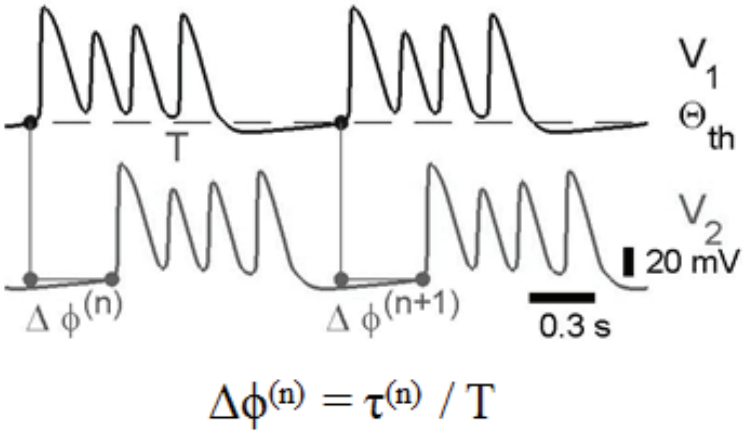

Figure 1.10. Phase differences measured with Poincaré sections.

parameters are introduced systematically; in the process, theoretical understanding of the system is validated or corrected as needed; only the inhibitory couplings are considered. The individual neuron used in the CPG was originally developed for leech heart interneuron, and the coupling paradigm used is FTM. The strategy is to use models that are well understood and introduce components that are grounded on a hypothesis about the mechanism of the CPG.

To reduce the number of distinct cases generated by combination of a plethora of parameters, coupling conductances are varied in groups, while maintaining small heterogeneity of random components up to 1% of mean strength. Figure 1.11 shows inhibitory connections grouped by colors and the parameter space organized by Cartesian product. Phase relation is captured by three unique phase differences ($\Delta\phi_{12}$, $\Delta\phi_{13}$, $\Delta\phi_{14}$), by choosing one of the neurons in the CPG as reference and other three as its partners (figure 1.9). For network period that admits single burst for each neuron, the reference neuron maintains phase difference of 1 , see $\Delta\phi_{11}$ in figure 1.9; and, the three phase differences may be used to obtain those between any pairs of neurons. For example, $\Delta\phi_{23} = \Delta\phi_{13} - \Delta\phi_{12}$. In addition, symmetry imposed by periodicity equates the value 0 and 1. In other words, $\Delta\phi = 1 - \Delta\phi$ imply the same phase difference between the neurons

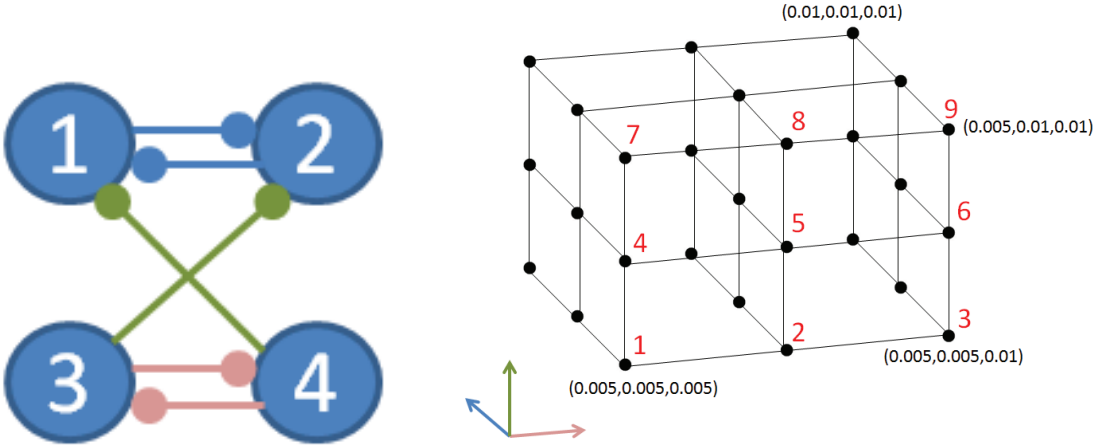

1.11.1 1.11.2

Figure 1.11. Schematic representation of coupling parameter groups and corresponding simulation grid. In 1.11.1 the color blue, green, pink corresponds to the pair of conductances $g_{12} \approx g_{21}$, $g_{32} \approx g_{41}$, and $g_{34} \approx g_{43}$ respectively. The 3D grid in 1.11.2 shows the parameter variation as the Cartesian product: $blue \times green \times pink$. The values in the vectors labeling the dots match the parameter sequence in the Cartesian product. The red numbers are inserted as shorthand for each of the gride nodes (dots), numbered sequentially from the front layer bottom left corner (1-9), middle layer bottom left corner starts with 10 and third layer bottom left corner starts with 19, following this numbering convention.

in the pair. This means the delay between the bursts in a pair is the same regardless of the chronological order of the bursts.

Discrete trajectories are constructed from a dense array of 3-tuple initial values, whose evaluation in the forward time represents the network phase state at every network period. Sequence of these phase differences resulting from the Poincaré mappings, when plotted in Cartesian coordinate, generate a 3D torus. Equivalently stated, the solutions stay within a unit cube whose opposite faces are identified; when a trajectory given by the mapping reaches either surface of the cube, it emerges from the side opposite to it. This toroidal resetting happens due to the equivalency between 0 and 1; a full description of the algorithm may be found in the appendix B. Finally, predictions are made based on parameter manipulations, and plausible sources of the experimentally observed pattern are suggested.

In chapter 6, conclusions and future directions are presented. The significance of the study and the results are briefly highlighted. In addition, relevance and importance of future investigations are discussed.

1.2 Hypothesis

The premise of this study is that the presence of spikes in bursts underlies the existence of multiple stable phase-locked states, including the synchrony. Multistability is hypothesized to be a common phenomenon for *square-wave* type bursting neurons, coupled reciprocally by fast, non-delayed inhibitory synapses. Further, the number of phase-locked states is suggested to be essentially determined by the number of spikes in the burst.

1.3 Significance

Many diseases and disorders result from the malfunctions of the nervous system. Starting from locomotion to cognition, all aspects of the animal behaviors are either generated or regulated by the nervous system. By understanding the functions, one can cure diseases, alleviate disorders, and may even build machines to serve greater purposes of the human society. To understand the functions of the nervous system, one needs to address numerous components and interactions. While high speed computers confer the ability to simulate very complex systems, underlying questions remains the same: what general laws govern the various functions of the nervous system? In this study, the role of bursts of activity in neurons and other electrically enabled cells is investigated. Processes resulting from spikes interact in a critical way during bursts of activities correlating to specific behaviors. In particular, spikes in bursting neurons are shown to play important roles in generating the robust correlates of a behavior.

In this study, it is found that the fast, non-delayed reciprocal inhibition can stably synchronize endogenously bursting neurons in the HCO through spike interactions. Fast, non-delayed inhibition is typical in many neuronal networks including the leech heartbeat CPG [23] or the *Melibe* swim CPG [54]. Since these systems are different from human

nervous systems in many ways, additional investigation is required to make direct connection. Nevertheless, the phenomenon is expected to persist with appropriate balance of parameters, and the basis for building machines controlled by artificial networks is an important implication of this study.

The bistability in HCO networks can make CPGs multistable with a bursting repertoire of two (anti-phase and in-phase) or more complex rhythms [55]. HCOs with bursting neurons contrast with the HCOs comprised of non-bursting neurons, which do not have spikes and are only capable of generating a single anti-phase rhythm. Compared to anti-phase bursting, less robust in-phase bursting can be effectively established in the HCO after both cells have received an external inhibition from another bursting neuron [56]. The computational approaches developed in the study enhances the perturbation technique of phase resetting curves (PRCs) [57]. The conventional PRCs are proven to be an effective tool for analyzing spiking neuronal models. However, the PRC technique, in application to bursting cells, produces rather complex outcomes (due to highly timing-sensitive changes in the number of spikes per burst that can sporadically cause large magnitude phase responses) even in the weak coupling case [58]. It is argued that the stability diagrams, along with Poincaré return mappings based on the variations of phase lags between the neurons, are more efficient tools for thorough studies of spike interactions in bursting neurons.

Finally, mathematical models and computational tools used to study the specific neurons and networks are generic to many classes of systems such as oscillations of proteins or genes. The abstraction of mathematics allows one to apply similar equations and analysis techniques for a multitude of real world phenomena. In addition to neuroscience, modeling studies can be easily maneuvered to include components of other critical and relevant modalities such as genetics or cardiac-vasculature systems. The ability to combine such seemingly disparate but interacting modalities through mathematical equations makes modeling studies a powerful tool for any scientist. Hence, tools and techniques developed in this study are very important for real world investigation and contribution to the society.

Chapter 2

MODELS AND METHODS

Mathematical models representing various biological processes have been developed and studied by many researchers over the decades [1, 16, 59]. In this chapter, the details of specific models and concepts used in the study are presented. While the applications in neuroscience is relatively new, some of the theories of dynamical systems revoked in this research have been known for centuries and are found in classic text books [60, 61]. Hence, general overview with fewer rigors are included for such concepts. First, mathematical equations and their electrophysiological interpretations are presented; second, overview of theories and concepts used for analysis are presented; finally, the computational implementation methods are presented.

2.1 Electrophysiological models

Electrical signals recorded from neurons represent the physiological entity (neuron) for the purpose of the model. While there are large amounts of details that may be included in a model, the most salient features included in these models are voltage-current relation governed by molecules or proteins that act as non-ohmic resistors. Below are detailed descriptions of the models used in the study.

2.1.1 Neuronal models

Following the Hodgkin-Huxley formalism, the models used for neurons represent sum of ionic currents that change with characteristic time dynamics. Ionic currents result from specific charges on types of ions, as they flow in and out of the neurons due to various influences, such as osmosis, active transport, or signal induced channel opening. Electrophysiologists have measured such currents, and ordinary differential equations (ODEs) are used to capture the conservation principle of the flow of currents. A set (system) of ODEs is used as the model of a neuron. Specific details of the models

are presented later; in the following, the general form of the ODE corresponding to most observable variable, membrane potential, is shown:

$$C\,V' = \sum_{i=1}^{n} I_i(V), \tag{2.1}$$

Here, V', C and I_i, respectively, represent the rate of change in the membrane potential measured in voltage, the capacitance of the membrane, and a number of ionic currents, referenced by the subscript i, that pass through the membrane. The flow of currents depend on the membrane potential, V, which in turn is determined by the level of these currents. Each current is characterized by reversal potential, meaning the direction of current is switched (inward/outward to outward/inward) when the membrane potential is above or below the corresponding reversal potential. Mathematically, this phenomenon is implemented by sign change, so that $I_i(V) = I_i(V - E_i)$, where E_i is the reversal potential for a particular ion. In addition, amount of current flowing is not necessarily constant; hence the use of appropriate function for approximation is imperative.

The functions used for ionic currents are experimentally established by approximating electrophysiological data. Amplitude of current is related to the ion specific channels, which have multiple subunits that have the ability to open or close. The effect of the activity of these subunits is captured by probability variables representing the degree to which channels are opened or closed. So, current I_i is the function of three quantities $((V - E_i), x_i(V), \bar{g}_{x_i})$, namely deviation of the membrane potential from the reversal potential, the voltage dependent probability variable(s), and the maximal conductance respectively. Product of voltage and conductance, multiplied by dimensionless probability variables approximates the amount of current flowing through the channels. The probability variables are also commonly referred to as gating variables that may activate or inactivate. In other words, activation level may saturate in the direction of depolarization or hyperpolarization (see figure 1.7.2). It is noteworthy that there is also evidence for unspecific ion channels and channels that have constant probabilities. For example, a class of current often referred as the ohmic leak current is modeled with these assumptions. Mathematically, ionic currents are expressed by the function, $I_i = \bar{g}_{x_i} x_i^k(V)(V - E_i)$,

where k is the number of gating subunits present in the channels, and x may be either activating, inactivating or product of both types of gating variables.

The flow of current is governed by processes that involve physical movement and conformational changes, both of which requires time. Specifically, the gating variables represent allosteric proteins that change shapes leading to opening or closing of channels through which ions pass. ODEs are used to capture the time dynamics of these processes. Time scales for different types of gates vary considerably. Some gate activities may be so fast that they are assumed to be at their full capacity, restricted only by membrane voltage but fully saturated regardless of time. These gates are represented by $x^{\infty}(V)$, which are typically Boltzmann functions, which have sigmoid shaped graphs as shown in 1.7.2, indicating 100% and 0% channel opening at the opposite ends of the voltage axis. Time scales are constants that define the multiple scales in the multiple-scale oscillators, and also the rate of dynamics for each dynamic variable (variable with non-zero time derivative). It is possible that time scales depend on voltage in such a way that assumption of constancy is invalid, and a function is used for better approximation of the time scales of the system, see tables in Appendix A. The model 2.4 retains voltage dependent time scales, while others maintain multiple but constant time scales.

The three distinct model neurons used in the study are listed and described in the rest of this section.

1. Leech heart interneuron model

   This model includes the fast sodium current, I_{Na}, the slow potassium current, I_{K2}, and an ohmic leak current, I_{L}, and is taken from [28]:

$$
\begin{aligned}
&C\,\frac{dV}{dt} = -I_{\mathrm{Na}}(V) - I_{\mathrm{K2}}(V) - I_{\mathrm{L}}(V) - I_{\mathrm{app}},\\
&I_{\mathrm{Na}} = \bar{g}_{\mathrm{Na}}\, n^3\, h\,(V - E_{\mathrm{Na}}), \quad n = n^{\infty}(V),\\
&I_{\mathrm{K2}} = \bar{g}_{\mathrm{K2}}\, m^2 (V - E_{\mathrm{K}}), \quad I_L = \bar{g}_{\mathrm{L}}\,(V - E_{\mathrm{L}}),\\
&\tau_{\mathrm{Na}}\,\frac{dh}{dt} = h^{\infty}(V) - h, \quad \tau_{\mathrm{K2}}\frac{dm}{dt} = m^{\infty}(V) - m.
\end{aligned}
\tag{2.2}
$$

   Here, V is the membrane potential, n and h are the gating variables for sodium channels, which activate and inactivate respectively as the membrane potential de-

polarizes. m is the gating variable for potassium channels that activate slowly as the membrane potential hyperpolarizes. The sodium current activates instantaneously. The time constants for the gating variables, maximum conductances and reversal potentials for all the channels and leak current, and the membrane capacitance are shown in table A.1. The steady state values of the gating variables are given by the Boltzmann functions in table A.2. An applied current $I_{\text{app}} = 0$ is used unless indicated otherwise. In this study, $\text{V}_{\text{K2}}^{\text{shift}}$ is a primary bifurcation parameter that controls the number of spikes per burst.

2. Sherman model of pancreatic beta cells

   This model [52] is based on two fast currents: calcium I_{Ca}, and persistent potassium I_K, and a slow potassium current I_s. V is the membrane potential and m, n, and s are the voltage dependent gating variables for these currents. The model is given by the ODEs:

$$\begin{aligned} &\tau \frac{dV}{dt} = -I_{\text{Ca}}(V) - I_{\text{K}}(V) - I_{\text{s}}(V), \\ &I_{Ca} = \bar{g}_{\text{Ca}}\, m^{\infty}(V)\,(V - E_{\text{Ca}}), \\ &I_{\text{K}} = \bar{g}_{\text{K}}\, n\,(V - E_{\text{K}}), \quad I_{\text{s}} = \bar{g}_{\text{s}}\, s\,(V - E_{\text{K}}), \\ &\tau \frac{dn}{dt} = \lambda[n^{\infty}(V) - n], \quad \tau_{\text{s}} \frac{ds}{dt} = s^{\infty}(V) - s. \end{aligned} \tag{2.3}$$

   The governing equations for the gating variables n and s are similar to those in (2.2), where the time constants, maximum conductances, and values of reversal potentials are shown in table A.3. In the model, an additional scaling factor, λ, controls the time scale of the persistent potassium channels. The steady state values of the gating variables are given by the Boltzmann functions in table A.4.

3. Purkinje neuron model

   This model [53] includes five currents: the sodium current, I_{Na}, with slow inactivation, h, and fast instantaneous activation, m^{∞}; the delayed rectifier potassium current, I_{K}, with activation, n; the non-inactivating calcium current, I_{Ca}, with activation c; the muscarinic receptor suppressed potassium current, I_{M}, with activation M; the leak current, I_{L}, and an applied current, I_{app}. The individual cell model is

given by:

$$\begin{aligned}
&\frac{dV}{dt} = -I_{\mathrm{Na}}(V) - I_{\mathrm{K}}(V) - I_{\mathrm{Ca}}(V) - I_{\mathrm{M}}(V) - I_{\mathrm{L}}(V) - I_{\mathrm{app}},\\
&I_{\mathrm{Na}} = \bar{g}_{\mathrm{Na}}\, m^3\, h\, (V - E_{\mathrm{Na}}), \quad m = m^{\infty}(V),\\
&I_{\mathrm{K}} = \bar{g}_{\mathrm{K}}\, n^4 (V - E_{\mathrm{K}}), \quad I_{\mathrm{Ca}} = \bar{g}_{\mathrm{Ca}}\, c^2 (V - E_{\mathrm{Ca}}),\\
&I_{\mathrm{M}} = \bar{g}_{\mathrm{M}}\, M\, (V - E_{\mathrm{M}}), \quad I_L = \bar{g}_{\mathrm{L}}\, (V - E_{\mathrm{L}}).
\end{aligned} \tag{2.4}$$

The governing equations for the gating variables h, n, c, and M are similar to those in 2.2, where the values for maximum conductances and reversal potentials are set according to table A.5. Voltage dependent time scales for the gating variables, measured in msec, are governed by the following functions shown in the tables A.6 and A.7. The steady state values of the gating variables are given by the Boltzmann functions in table A.8. Here the applied current is a bifurcation parameter, set for the cell to be a long burster, as $I_{\mathrm{app}} = -27$ nA.

4. Fitzhugh-Rinzel model

   This is a phenomenological model and thus lacks specifically defined ionic currents. However, it does produce regular bursts with two spikes for the parameter values given in A.9. This is a classical model of excitable system, a system that is capable of producing large amplitude oscillation centered around a small amplitude (nearly quiescent) branch, a characteristic feature of elliptic bursters [1].

$$\begin{aligned}
\frac{dx}{dt} &= x - \frac{x^3}{3} - y + z + I,\\
\frac{dy}{dt} &= \delta(a + x - by),\\
\frac{dz}{dt} &= \mu(c - x - z).
\end{aligned} \tag{2.5}$$

   Here, the parameters δ and μ are the timescales, similar to τ's in the other models. In the first equation, the value of timescale is 1, set as two orders larger than δ and three order larger than μ, which makes z the slowest variable of the system.

The first three cases of neuron models generate bursting patterns of square-wave type, which is characterized by depolarized spikes and hyperpolarized silent state. The fourth

produces bursts of elliptic type, which is characterized by silent state at a depolarized level between the minimum and maximum level of spikes. Elliptic bursters, such as Fitzhugh-Rinzel model, involve delayed loss of stability and canard solutions [62], which make the system very sensitive and inherently unstable. As a result, only the first three models show multiple phase relations that are stable. Equivalently stated, multiple phase-locked states coexist in the first three cases. This coexistence implies multiple behaviors, corresponding to multiple possible fixed time delays between the spiking activities in the voltage traces, may be controlled by same network.

2.1.2 Network models

The network that is the primary focus of this study is a pair of neurons in the half center oscillator (HCO) configuration. Other networks that have been explored are all-to-all (global) and local reciprocally inhibited networks. Schematic diagrams of these networks are shown in the figure 1.8.2. In terms of the equations, negative synaptic currents, $-K_i \cdot I_{\text{syn}}^{(i)}$, are now added to the individual neuron model.

$$C\,V_i' = F(V_i, \mathbf{h}_i) - K_i \cdot I_{\text{syn}}^{(i)}, \quad \tau(V_i)\mathbf{h}_i' = G(V_i, \mathbf{h}_i), \quad i = 1..n. \tag{2.6}$$

where V_i stands for the i-th neuron membrane potential, and $\mathbf{h}_i$ stands for the gating (in)activation variable(s) describing kinetics of specific ion current(s) with a characteristic time scale(s) $\tau(V_i)$. The scalar notation for the characteristic time should be interpreted as distinct for individual gating variables in the vector $\mathbf{h}$. K_i is n-dimensional connectivity vector whose jth entry is either 1 or 0, indicating whether synaptic input can be received from the jth neuron or not. For example, all entries are 1 except when $i = j$ in global networks, as every neuron receives input from every neuron except from itself. For local networks, only $(i-1)$th and $(i+1)$th entries have value 1, assuming $K_{i,1-1} = K_{i,n}$ and $K_{i,n+1} = K_{i,1}$. The $I_{\text{syn}}^{(i)}$ is a vector of all possible synaptic inputs, $I_{\text{syn}}^{(ij)}\ j = 1..n$. Neurons composing all networks and connections among them are assumed to be identical, hence,

$$I_{\text{syn}}^{(ij)} = g_{\text{s}}(V_i - E_{\text{syn}})S(V_j), \quad j = 1..n. \tag{2.7}$$

Here $S(V_j)$ is the synaptic gating variable, which may or may not be dynamical. The details of the synaptic models are presented in the next section.

In addition to the above networks, an experimental CPG for swimming behavior of marine invertebrate *Melibe leonina* has also been studied. This network has four model neurons that are grouped into two pairs of HCOs and unidirectional inhibitions from one pair to the other. The connectivity vectors are stacked row wise to form a matrix and shown below:

$$\left(K_{ij} \right) = \begin{bmatrix} 0 & 1 & 0 & 1 \\ 1 & 0 & 1 & 0 \\ 0 & 0 & 0 & 1 \\ 0 & 0 & 1 & 0 \end{bmatrix} \tag{2.8}$$

Here the i-th neuron inhibits j-th neuron if there is a non-zero number at the ij-th entry. The schematic diagram for the network is shown in figure 5.1.1. In future, signs and ϵ may be added in the matrix to indicate inhibitory, excitatory, and electric coupling.

2.1.3 Synaptic models

Models used for synapses have several levels of details. On one extreme, Heaviside and fast threshold modulatory (FTM) synapses with no time dynamics are used; on the other extreme, dynamic synapses with up to three time dependent variables are used. In total, four types of models are used to approximate fast non-delayed synapses.

1. "Heaviside" synapse

   This is the simplest representation of the synapses [32, 49]: $S(V_j) = H(V_j - \Theta_{\text{syn}})$ with $H = \{0, 1\}$. The synapse activates instantaneously, $S(V_j) = 1$, as soon as the membrane potential V_j of the presynaptic neuron exceeds the synaptic threshold Θ_{syn}, and deactivates instantaneously, $S(V_j) = 0$, after V_j drops below Θ_{syn}. The synaptic threshold Θ_{syn} is chosen to ensure that every spike of the bursting cell crosses the threshold 2.1. The actual value for Θ_{syn} is determined for each model individually. Unless specified otherwise, we fixed $\Theta_{\text{syn}} = -0.0225$ V for the leech

interneuron model, $\Theta_{\rm syn} = -0.03$ V for the Sherman model, and $\Theta_{syn} = -0.036$ V for the Purkinje cell model. For Fitzhugh-Rinzel model the number 1000 below is replaced by 50 and the value corresponding to Θ_{syn} is -0.8

2. Fast threshold modulatory (FTM) synapse

   The coupling function is modeled by the sigmoidal

$$S(V_j) = 1/[1 + \exp\{-1000(V_j - \Theta_{\rm syn})\}]. \tag{2.9}$$

   This coupling form was introduced and called the fast threshold modulation by Somers and Kopell [49]. It is a smooth version of the Heaviside coupling function with the same rise and decay times (compare panels A and B in Fig. 1). The FTM is a remarkable model of a realistic fast synapse [32, 49], such as that in the leech heart CPG [23], as it yields a nearly instantaneous response from the synapse on the post-synaptic neuron.

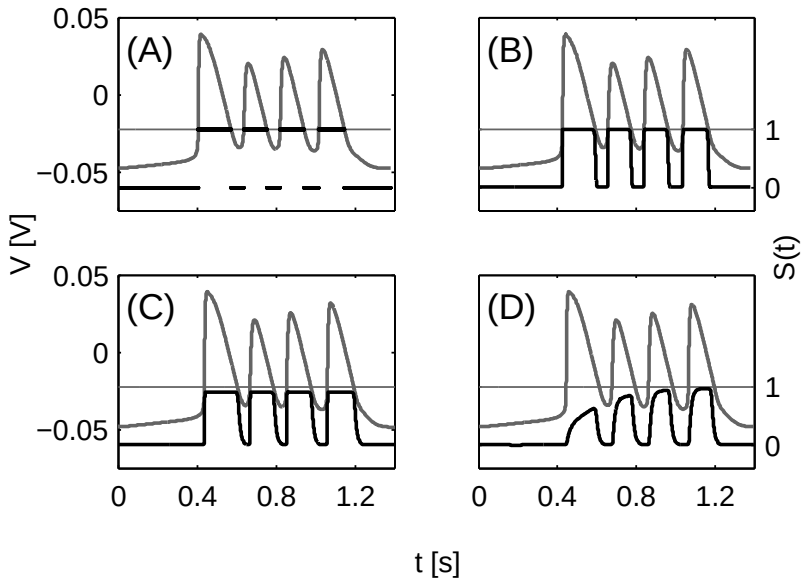

Figure 2.1. Four-spikes bursting in the leech interneuron HCO (2.13). Overlaid is the normalized synaptic function $S(t)$ for the synapse modeled by the (A) Heaviside function; (B) FTM coupling; (C) α-synapse and (D) leech heart dynamical synapse. Here $\Theta_{syn} = -0.0225$ (horizontal line across the panels aligned to Θ_{syn} on the left and $S(t) = 1$ on the right) and $g_{\rm syn} = 0.005$.

3. α-dynamical synapse

   In this frequently used model of the synapse [33, 34] the coupling function $S(V_j)$ is described by the following ODE:

$$S'(V_j) = \alpha(1 - S)[1 + \exp(-1000(V_j - \Theta_{\text{syn}}))]^{-1} - \beta S. \tag{2.10}$$

   Here, $\alpha = 1000$ and $\beta = 100$ are set to match the rate of the synaptic onset, decay, and maximum efficacy ($S \approx 1$) similar to the FTM synapse (see Fig. 1C). Decreasing β makes the synaptic current last longer.

4. Leech heart dynamical synapse

   The last model for fast synapses is from leech heart CPG, introduced in [23], where $S(V_j) = Y\,M(V_j)$ is such that the fitted dynamics of the variables Y and M are governed by the auxiliary ODE system:

$$\begin{aligned} \dot{X} &= [[1 + \exp(-1000(V_j - \Theta_{syn}))]^{-1} - X]/0.002, \\ \dot{Y} &= (X - Y)/0.011, \\ \dot{M} &= [0.1 + 0.9[1 + \exp(-1000(V_j + 0.04))]^{-1} - M]/0.2. \end{aligned} \tag{2.11}$$

2.2 Mathematical concepts

Systems of ordinary differential equations are commonly analyzed for long term behaviors. Analytically, these approaches work well for characterizing the local behaviors of the system such as steady states or equilibriums. In recent years, the uses of numerical integration methods and high speed computers have allowed one to screen global behaviors as well. Global behaviors can be as simple as plain periodic orbit or as complex as bursting periodic orbits or chaotic and aperiodic orbits [8, 9, 63]. In this study both analytical and numerical approaches have been used in conjunction. Some of the relevant concepts and definitions are presented next.

2.2.1 Steady states

Steady states are attained when transient changes disappear from the system. The figure 2.2 shows solution trajectories that approach steady states over time. There are two steady states achieved in forward time, which corresponds to following the traces to the right of the figure. In the figure, all of the traces either move to the top or the bottom. The persistent horizontal slopes of the trajectories indicate that the rates of change of the variable being plotted have vanished. Loss of change over time is precisely how the steady states are defined. So, there are steady states located at the top and the bottom of this figure. In addition, there is a invisible steady state that separates the two visible steady states.

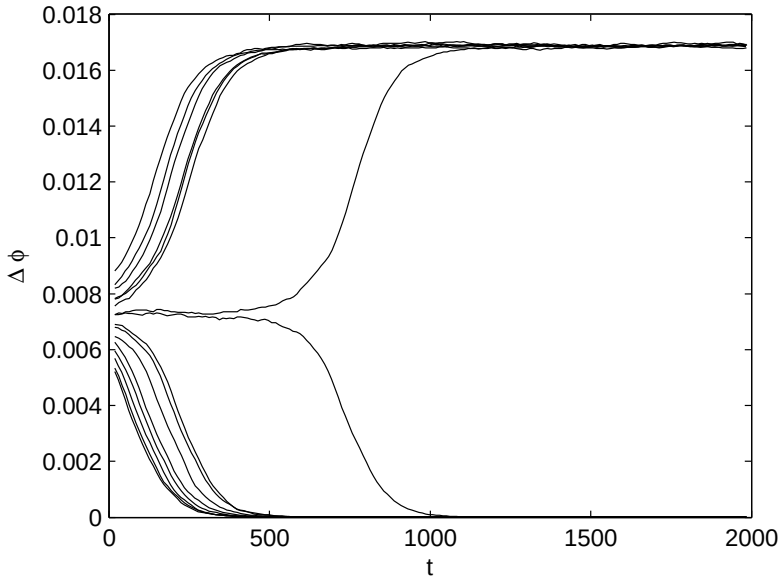

Figure 2.2. Phase-lag traces showing unstable and two stable states in close proximity for parametric regime (1) in 2.7. A phase-locked state other than anti-phase, which has phase-lag $\Delta\phi = 0.5$, is observed. The phase-locked states, $\Delta\phi = 0, 0.017$, attract nearby trajectories as time progresses, whereas the state $\Delta\phi \approx 0.007$ repels (separates).

When trajectories are near the invisible steady state, they move away from it in forward time. As a result, one sees traces emanating from it as the traces move to the right of the figure. On the other hand, if the time is reversed and one follows the traces from right to left, then the middle steady state now attracts all trajectories. In the backward time, it appears that the trajectories are emanating from the top and

the bottom steady states. The two types of behaviors of steady states, attracting or emanating are rigorously defined by the concept of stability, which is presented in the section 2.2.2.

The time derivatives, which are the rates of change of dynamic (time dependent) variables become zero. For the first order ODE systems with linear or weakly non-linear terms, the steady states can be found analytically by setting the derivatives to zero and solving the resulting system. Shown below are calculations for the leech model:

$$\begin{aligned} 0 &= -I_{\mathrm{Na}}(V) - I_{\mathrm{K2}}(V) - I_{\mathrm{L}}(V) - I_{\mathrm{app}}, \\ 0 &= h^{\infty}(V) - h, \quad 0 = m^{\infty}(V) - m. \end{aligned} \tag{2.12}$$

As a result following function is gotten that describes the steady states of the system.

$$I_{\mathrm{app}} = -\bar{g}_{\mathrm{Na}}\, n^{\infty}(V)^3\, h^{\infty}(V)\,(V - E_{\mathrm{Na}}) - \bar{g}_{\mathrm{K2}}\, m^{\infty}(V)^2 (V - E_{\mathrm{K}}) - \bar{g}_{\mathrm{L}}\,(V - E_{\mathrm{L}}). \tag{2.13}$$

Here the applied current, I_{app}, is often treated as the independent variable since it can be controlled by the experimenter. For this reason, it is also the parameter of choice for analyzing individual neuron models. In this study, value of this parameter is fixed at a level that generates bursting behavior. For example, figure 2.3 shows steady states M_{eq} in blue S-shaped curve, but the trajectories, shown in black and grey, do not settles at the steady states; they form a closed loop with multiple oscillations corresponding to bursts. Figure 2.5, on the other hand, shows the graph of steady states from an analogous equation as 2.13. This figure plots steady states of a HCO as the function of the coupling parameter g_s of the network, instead of the parameter I_{app}. Further details and use of steady states are provided in the next few sections.

2.2.2 Stability

The concept of stability classifies the behaviors of solutions surrounding a steady state. As mentioned earlier, a steady state may attract or emanate other solutions (see figure 2.2). A steady state is asymptotically stable, when other solutions approach it as time progresses. On the other hand, it is unstable, if other solutions emanate or

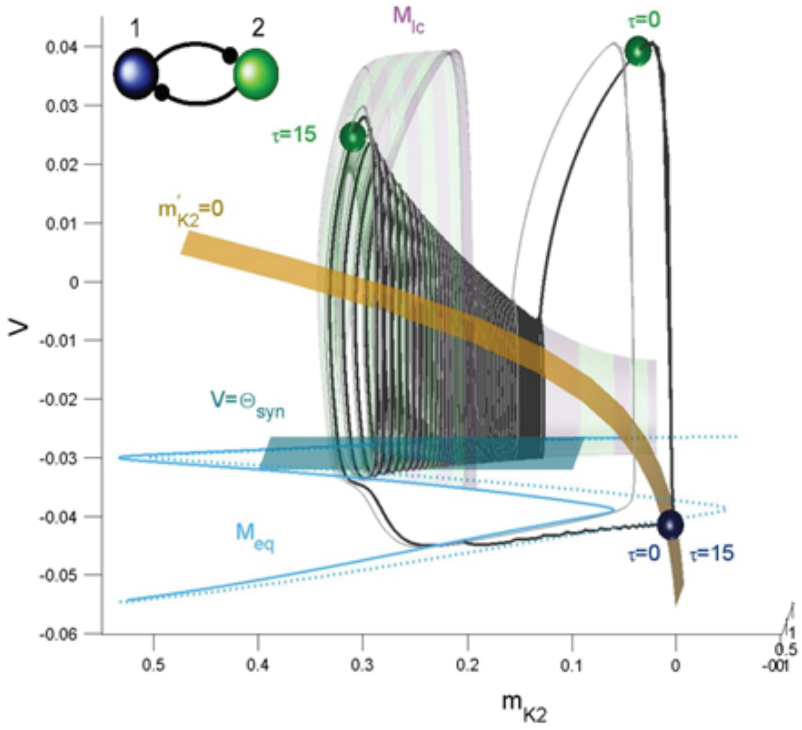

Figure 2.3. Depiction of steady states, nullclines and bifurcations in a single neuron model. This figure is reproduced from [64].

diverge from it as time progresses. In addition, it is possible to have solutions that do not approach or diverge from a steady state, but maintains limited distance from the nearby steady states. A periodic orbit is an example of such a solution. Figure 2.3 shows that a bursting periodic orbit (black/grey curves) maintains limited or bounded distance from the steady state solutions (blue curve).

The classical method for analyzing stability of steady states of ODEs is through locally linearizing the system in a small neighborhood of the steady state under investigation. Lyapunov stability of a solution of interest, $\mathbf{V}^*$, is defined by growth or decay of small perturbation, $\delta\mathbf{V}$, so that over time $\mathbf{V}^* + \delta\mathbf{V}$ approaches one of three outcomes: $|\mathbf{V}^* + \delta\mathbf{V}| \to \infty$, $|\mathbf{V}^*| < |\mathbf{V}^* + \delta\mathbf{V}| < \infty$, or $|\mathbf{V}^* + \delta\mathbf{V}| \to |\mathbf{V}^*|$. In the first case, solution is unstable; in the second case, it is stable, and in the last case, it is asymptotically stable.

Locally, stability of steady states are detected by characteristic exponents, that is the rate of convergence or divergence of solutions near the steady state up to linear rate, which turn out to be the eigenvalues of the Jacobian, the first derivative of the system

of ODE. In this study, the primary focus is the stability of periodic bursting orbits, the stability of which is studied by Poincaré return maps, described in the section 2.2.4.

2.2.3 Nullclines

The nullclines are found by setting the derivative of one dynamic variable to zero, as opposed to those of all the variables as in the case of steady states. As a result, each variable has a corresponding nullcline. Analytical expression of the nullclines may be complex, but geometrically they provide much useful insight into the global behaviors of the system. The figure 2.3 shows the nullcline (gold color) of the slowest variable m in 2.2, where $\dot{m} = 0$. The steady states coincide with the intersections of all the nullclines, as all the derivatives vanish at these points. Figure 2.3 depicts this process, except due to high dimension two of the nullclines are not plotted, only their intersection (dashed, blue curve) is plotted, the third nullcline is shown in gold.

In studying the systems that have multiple (time) scales, it is classical to consider the nullcline of the slowest variable in particular. The slow variable, m, grows ($\dot{m} > 0$) above the slow nullcline and decays ($\dot{m} < 0$) below it. The spikes in the bursting patterns are generated by the fast periodic orbits (loops foliating M_{lc}), and the slow silent phase is generated by hyperpolarized steady states in M_{eq}. The location of nullcline dictates the existence of bursting pattern. A low level causes asymptotically stable steady state, leading to persistent silent phase of the neuron; a high level causes stable fast periodic orbit, leading to persistent spiking behavior of the neuron. For the bursting behavior to exist, the nullcline must be located at an intermediate level such that neither the steady state nor the fast periodic orbit is stable, such that a complex periodic orbit may exist in combination of the two.

2.2.4 Poincaré return maps

Periodic orbit, by definition, returns periodically to every point that belongs to it. Poincaré section, named after Henri Poincaré, is a set that is transversal to the periodic orbit and small enough such that the periodic orbit intersects it only once. The mapping constructed from the points after every periodic return to the section is the Poincaré

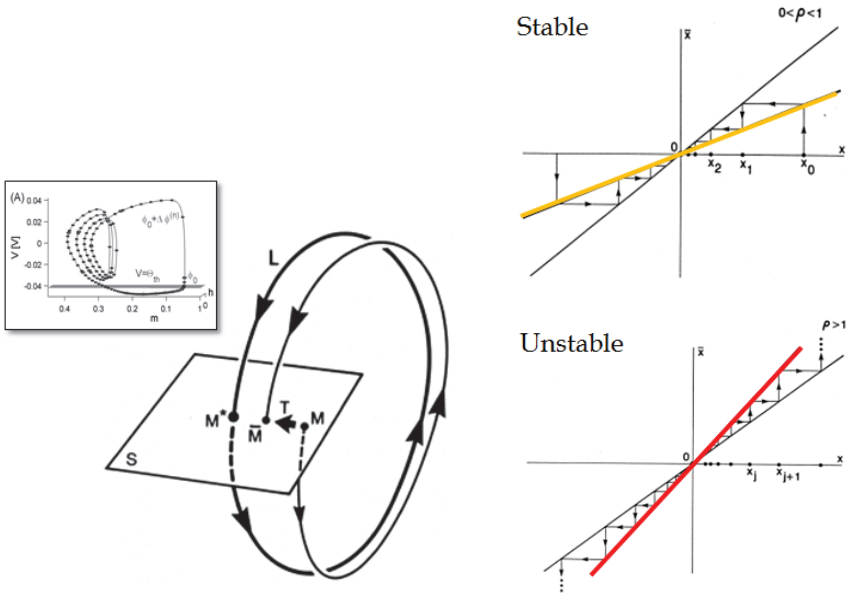

2.4.1 2.4.2

Figure 2.4. Schematic portrayal of Poincaré return maps and the stabilities of their fix points. Figure reproduced and modified from [8, 65].

return map, and the periodic orbit is its fixed point (M^* in figure 2.4.1 and the bursting orbit from leech HCO in the study, shown in inset). If the mapping is of contraction type, then the periodic orbit is asymptotically stable. Then the slope of the mapping, its derivative, has magnitude less than one (top panel in 2.4.2). If a trajectory is not the periodic orbit itself but approaches one, then the mapping is useful in finding the destination of the trajectory by applying it iteratively a number of times, or cycles. If the mapping has slope of magnitude bigger than one at the fixed point, then the corresponding periodic orbit is unstable (bottom panel in 2.4.2).

2.2.5 Bifurcations

In the theory of qualitative analysis of dynamical systems, two systems are considered to have the same behavior if changing a parameter does not cause emergence or disappearance of qualitatively distinct solutions such as steady states, periodic orbits or other complex structures. Change in stability is also considered qualitatively distinct; however, change in numerical values of these solutions is not considered to be so. Bifur-

cation diagrams capture the number of distinct behaviors in a system and how they are organized and transition in some critical parameter space.

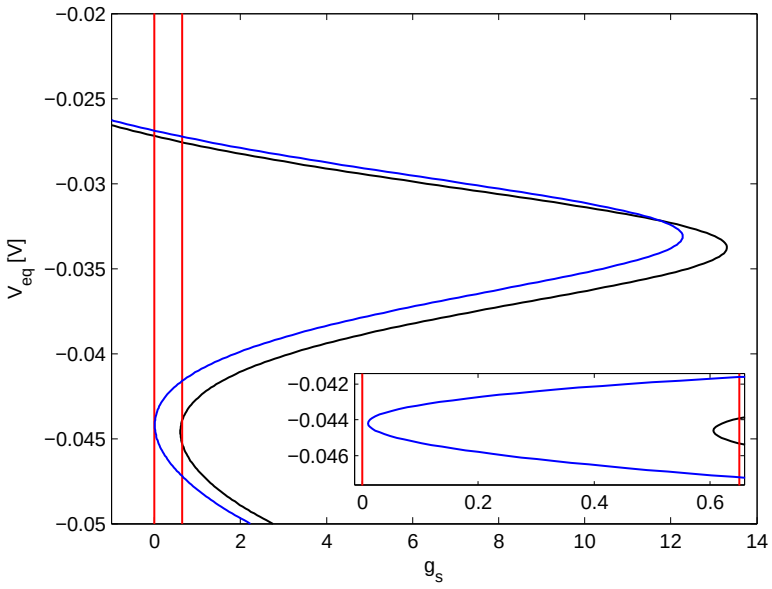

Figure 2.5. Bifurcations of steady states in HCOs as function of coupling parameter g_s. Two different set of parameters are used in the individual neuron models in the HCO: (1) near blue sky catastrophe (blue) [51], or (2) period doubling cascade (black) [28]. Vertical lines cross the curves at equilibrium points for the corresponding values of the parameter, $g_s = 0, 0.65$. Inset shows magnification of the knee region where two new equilibriums emerge through saddle node bifurcation.

The variable m_{K2} in the model 2.2 and depicted in the figure 2.3 is considered the bifurcation parameter in the analysis of dynamical systems via the slow-fast decomposition of the time scales. Because m_{K2} is the slowest variable in the system, it is treated as a parameter and the qualitatively different behaviors as a function of this variable is identified. For example, in the aforementioned figure high values of m_{K2} have a single steady state in the fast subsystem (lower blue curve, extending to the left in the picture), for slightly lower value there are three steady states (middle portion of S-shaped blue-curve, but to the left of M_{lc}), for even lower values there is a periodic orbit in addition to the steady states (middle portion of S-shaped blue-curve, but including only M_{lc}). Insight gained from bifurcation analysis helps one to identify zones of qualitatively significant dynamics in a system.

In contrast to the bifurcation analysis of individual neuron model, figure 2.5 shows a bifurcation diagram of two coupled neurons in HCOs. The black and blue folded curves indicate that for some critical coupling strengths, g_s, the number of steady states transition from 1 to 3 steady states as g_s increases from zero, or 3 to 1 steady state as g_s increases further past the value of 10. Lowest (hyperpolarized) branch fall below the graphed window in the figure. Known as hysteresis, this curve is a classical bifurcation structure in many systems. In this study, the diagram enables one to precisely define the value of g_s for which transition from 1 to 3 steady states happens. Figure shows the set of steady states for two distinct set of parameters defining the individual neurons. The existence of hyperpolarized branch following the transition coincides with the network interaction known as the hold-then-release mechanism for anti-phase bursting [56, 64]. When hold-and-release mechanism is established in the HCO, spikes of one neuron com-

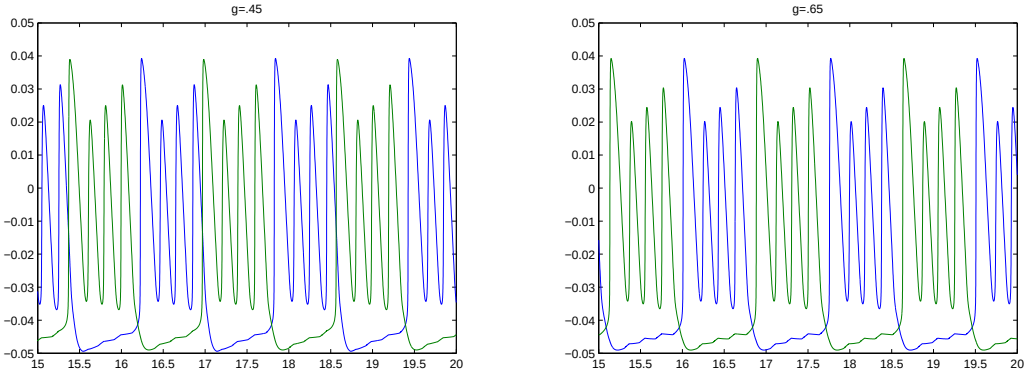

2.6.1 2.6.2

Figure 2.6. Traces showing anti-phase bursts with or without hold-then-release mechanism.

pletely block spike initiation in the other neuron. Each neuron takes turn to be active; such anti-phase bursts are qualitatively distinct from the case when some spikes may overlap in the anti-phase bursts (traces shown in figure 2.6). Thus, bifurcation diagrams help one to distinguish processes in the dynamical systems.

Weak to strong: bifurcation of coupling strength. In this study, HCOs are investigated in two distinct regimes or bifurcation zones given by the coupling strength of the network. The two regimes are distinguished qualitatively by the smoothness of the phase

difference trajectories. Figure 2.7 demonstrates the difference between the two regimes.

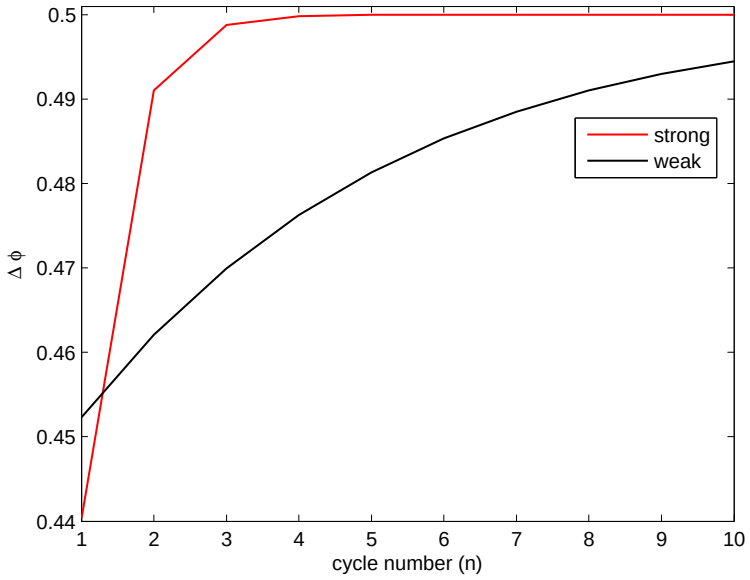

Figure 2.7. Strong versus weak coupling definition. Graphs of smooth (black curve) and non-smooth (red curve) convergence of phase differences $\Delta\phi$.

Sudden large changes are indicative of highly non-linear interactions among the variables. Hence, the results of weakly coupled networks are not valid for strongly coupled ones.

2.2.6 Mean Value Theorem

Suppose the function $F(x)$ is C^1 that is it is continuous and has continuous derivative on $[a, b]$, $a < b$. Then there exist a number c such that $a < c < b$ and $F'(c) = (F(b) - F(a))/(b - a)$ [60]. This can be applied for a small deviation ξ such that $\xi F'(x) = F(x + \xi) - F(x)$. In the derivation of variational equations $V_1 = x + \xi$ and $V_2 = x$ is set. On the synchronous manifold where $\{V : V_1 = V_2\}$ the following derivative $\{F'(V) : F'(v_1) = F'(V_2)\}$ is used to approximate $F(V_1) - F(V_2)$ by $F'(V)\xi$. This approximation is justified as long as ξ is small.

2.2.7 Variational equations

Individual models of neurons in networks confer symmetry that may be used to study convergence or divergence properties of small variations of special solutions. In-

phase synchronization, where all variables in each model neurons are identical, is one such solution. Shown below are the variational equations for transverse perturbations to the synchronous solution for the leech HCO connected by FTM synapses. These equations are obtained by following the method in [10].

$$\begin{aligned} C\,\xi' &= F_V(V,h,m)\xi + F_h(V,h,m)\eta + F_m(V,h,m)\zeta + \\ &\quad +(S_1+S_2)\xi \\ \tau_{\rm h}\eta' &= G_V(V,h)\xi - \eta,\ \tau_{\rm m}\zeta' = R_V(V,m)\xi - \zeta, \end{aligned} \tag{2.14}$$

where $\xi = V_1 - V_2$, $\eta = h_1 - h_2$, $\zeta = m_1 - m_2$ are infinitesimal perturbations of the zero equilibrium state of (2.14), which represents in-phase synchronization. In (2.14), $\{V(t),\ h(t),\ m(t)\}$ corresponds to the synchronous bursting rhythm. The terms $S_1 = -g_s\Gamma(V-\Theta_{\rm syn})$ and $S_2 = g_s(V-E_{\rm s})\Gamma_V(V-\Theta_{\rm syn})$ are due to the synaptic coupling. The derivation of the variational equations is presented next.

Suppose, $\dot{V}_i = F(V_i,h_i,m_i) - g_s(V_i - E_{syn})\Gamma(V_j - \Theta_{syn})$ where $i,j = 1,2$, then the rate of change of the infinitesimal perturbation $\dot{\xi}$ is obtained as the following:

$$\begin{aligned} C\,(\dot{V}_1 - \dot{V}_2) &= F(V_1,h_1,m_1) - g_s(V_1-E_{syn})\Gamma(V_2-\Theta_{syn}) \\ &\quad -F(V_2,h_2,m_2) + g_s(V_2-E_{syn})\Gamma(V_1-\Theta_{syn}) \\ C\,\dot{\xi} &= F(V_1,h_1,m_1) - F(V_2,h_2,m_2) \\ &\quad +g_s(V_2-E_{syn})\Gamma(V_1-\Theta_{syn}) - g_s(V_1-E_{syn})\Gamma(V_2-\Theta_{syn}) \\ C\,\dot{\xi} &= F(V_1,h_1,m_1) - F(V_2,h_2,m_2) \\ &\quad +g_s(V_2-E_{syn})\Gamma(V_1-\Theta_{syn}) - g_s(V_1-E_{syn})\Gamma(V_2-\Theta_{syn}) \\ &\quad +g_s(V_1-E_{syn})\Gamma(V_1-\Theta_{syn}) - g_s(V_1-E_{syn})\Gamma(V_1-\Theta_{syn}) \\ &\quad +g_s(V_2-E_{syn})\Gamma(V_2-\Theta_{syn}) - g_s(V_2-E_{syn})\Gamma(V_2-\Theta_{syn}) \end{aligned} \tag{2.15}$$

In order to approximate the deviation in F with the mean value theorem, it is assumed that $F(V_1,h_1,m_1) - F(V_2,h_2,m_2) \approx F(V_1,h,m) - F(V_2,h,m) + F(V,h_1,m) - F(V,h_2,m) + F(V,h,m_1) - F(V,h,m_2)$ so that $F(V_1,h,m) - F(V_2,h,m) \approx F_V(V_1 - V_2) = F_V\xi$, $F(V,h_1,m) - F(V,h_2,m) \approx F_h(h_1-h_2) = F_h\eta$ and $F(V,h,m_1) - F(V,h,m_2) \approx$

$F_m(m_1 - m_2) = F_m\zeta$. These steps explain the first three terms in the ODE $C\xi'$ in the equation 2.14. By rearranging the synaptic components the fourth term is derived as follows:

$$\begin{aligned}
C\,\dot{\xi} &= ... \\
&\quad +g_s(V_1 - E_{syn})\Gamma(V_1 - \Theta_{syn}) - g_s(V_2 - E_{syn})\Gamma(V_2 - \Theta_{syn}) \\
&\quad +g_s(V_2 - E_{syn})\Gamma(V_1 - \Theta_{syn}) - g_s(V_1 - E_{syn})\Gamma(V_1 - \Theta_{syn}) \\
&\quad +g_s(V_2 - E_{syn})\Gamma(V_2 - \Theta_{syn}) - g_s(V_1 - E_{syn})\Gamma(V_2 - \Theta_{syn}) \\
C\,\dot{\xi} &= ... \\
&\quad +g_s\{\Gamma(V - \Theta_{syn})(V - E_{syn})\}'(V_1 - V_2) \\
&\quad +g_s(V_2 - E_{syn} - V_1 + E_{syn})\Gamma(V_1 - \Theta_{syn}) \\
&\quad +g_s(V_2 - E_{syn} - V_1 + E_{syn})\Gamma(V_2 - \Theta_{syn}) \\
C\,\dot{\xi} &= ... \\
&\quad +g_s\{\Gamma(V - \Theta_{syn}) + (V - E_{syn})\Gamma_V(V - \Theta_{syn})\}\xi \\
&\quad -g_s\Gamma(V - \Theta_{syn})(V_1 - V_2) - g_s\Gamma(V - \Theta_{syn})(V_1 - V_2) \\
C\,\dot{\xi} &= ... \\
&\quad +g_s\Gamma(V - \Theta_{syn})\xi + g_s\Gamma_V(V - \Theta_{syn})(V - E_{syn})\xi - 2g_s\Gamma(V - \Theta_{syn})\xi
\end{aligned} \tag{2.16}$$

Thus the second term in the ODE $C\xi'$ in the equation 2.14 is obtained. The derivations of $\tau_h\eta'$ and $\tau_m\zeta'$ is similar but simpler since there are no synaptic terms in the corresponding ODEs. One only needs to replicate the procedure 2.15 for $\tau_h\dot{h_i} = G(V_i, h_i, m_i)$ and $\tau_m\dot{m_i} = R(V_i, h_i, m_i)$ with $i = 1, 2$.

For larger networks with equal number of inputs, only the terms due to synaptic coupling needs to be modified as following: $S_1 = -kg_s\Gamma(V - \Theta_{\text{syn}})$ and $S_2 = (k + \gamma_2)g_s(V - E_{\text{s}})\Gamma_V(V - \Theta_{\text{syn}})$, where k is the number of synaptic inputs each neuron receives and γ_2 is the second largest eigenvalue of a matrix $\mathbf{G}$. The connectivity of the network is represented by the matrix $\mathbf{G}$ which is gotten from the connection matrix $\mathbf{K}$ such as 2.8. When all neurons have equal inputs, the matrix $\mathbf{G} = \mathbf{K} - \mathbf{kI}$ such that it has zero row sum. A classical result for such matrix is the existence of zero eigenvalue while all other

eigenvalues are of the same sign [66]. For the networks considered in this study all other eigenvalues except the zero eigenvalue are negative.

2.2.8 Lyapunov Exponents

Named after Aleksandre Lyapunov, Lyapunov exponents are measures of exponential rate of separation between trajectories as time progresses. The trajectories are initially separated by infinitesimal perturbation. Suppose, $\mathbf{\Psi} = (\xi, \eta, \zeta)$ is defined as the vector defining the small perturbation. The entries ξ, η, ζ are similarly defined as in the section 2.2.7. Then the Lyapunov exponent is defined as the following:

$$\lim_{t\to\infty} \frac{1}{t} \ln \frac{|\mathbf{\Psi(t)}|}{|\mathbf{\Psi(t_0)}|} \tag{2.17}$$

where $\mathbf{\Psi(t)}$ is time evolution of the initial infinitesimal perturbation $\mathbf{\Psi(t_0)}$. Such small variations may grow or decay as the time evolves. An average measure of this growth and decay is indicated by a spectrum of Lyapunov exponents. The number of exponents in the spectrum corresponds to the dimension of the system of interest.

For the synchronous trajectory, Q_s in figure 3.1, $\{V_1 = V_2, h_1 = h_2, m_1 = m_2 : \forall\ t\}$, three of the six Lyapunov exponents are zero, other three corresponds to transverse perturbation and are measured with 2.14. The signs of these Lyapunov exponents indicate the overall convergence or divergence of the nearby trajectories. For the networks considered in this study, two of the non-zero Lyapunov exponents are always negative, hence the stability is indicated by the sign of the third non-zero Lyapunov exponent. In other words, the largest Lyapunov exponent may be positive or negative, which corresponds to unstable or stable zero steady state of the variational equations respectively. Although there are methods to compute Lyapunov exponents without the use of variational equations, it has been found to be more accurate to use the variational equations [67].

2.3 Computational methods

ODE integrator routines from Matlab software were used to simulate the solutions of all the networks presented in this discourse except those of experiment-based *Melibe* CPG.

2.3.1 Lyapunov Exponents

The algorithm used for Lyapunov exponents is adapted from the Matlab code written by V. N. Govorukhin, who wrote the code based on the method suggested by [68]. The method evaluates the variational equations on an orthonormal matrix (unit cube) and renormalizes the transformed matrix at specified time intervals to produce $\Psi(t)$ in the equation 2.17. Govorukhin's code is freely available through his website and the Matlab central website [69, 70]. Figures 2.8 and 2.9 show the number of step sizes, and durations of the settle time are used to gauge the appropriate discretization.

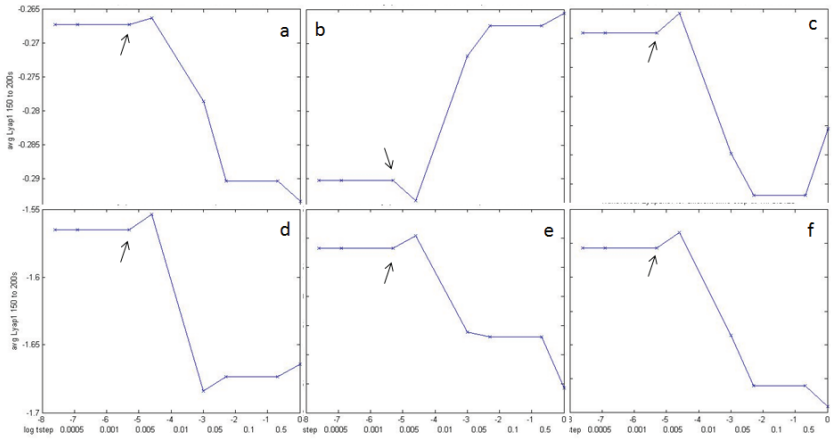

Figure 2.8. Comparison of step size for largest Lyapunov exponent calculation using long time average. Lyapunov exponents were calculated at regular time intervals for 200 seconds, and the average of last 50 seconds are plotted. The step sizes used for time intervals, plotted right to left in each panel on logarithmic scales, are $1, 0.5, 0.1, 0.05, 0.01, 0.005, 0.001, 0.0005$. Variation in amplitude plateaus at 0.005, which was chosen for all simulations of Lyapunov exponents, except in the cases of larger networks where an alternate algorithm was used. Synaptic threshold varies in each panel, $\Theta_{syn} = -0.0375$ (a),-0.031 (b),-0.0285 (c),-0.021 (d),-0.0085 (e),0.0125 (f).

Randomly selected stability outputs by the above algorithm are verified by Matlab toolkit for Lyapunov exponent, LET, and by directly measuring maximum difference

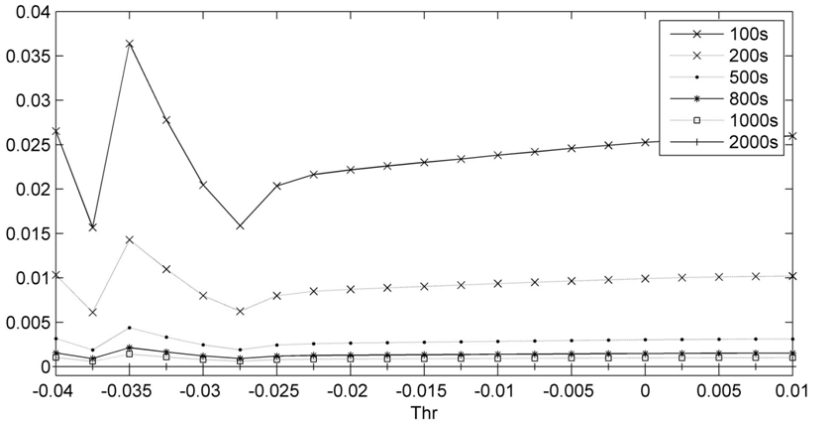

Figure 2.9. Synaptic threshold dependence of error in Lyapunov exponent compared to last 50 seconds average of 2000 seconds long simulation. Compared maximum largest Lyapunov exponent, see 3.5, the error is less than 5%; vertical axis represent difference of Lyapunov exponent shown by the legend with that computed for 2000 seconds.

between the trajectories after removing the transients. Two methods are used to evaluate Lyapunov exponents: (1) the aforementioned algorithm is simulated for 200 seconds and averaged over last 50 seconds, and (2) linear coefficients of the variational equations are multiplied to an unit matrix precisely for one period, T. Then the Floquet multipliers, eigenvalues of the transformed matrix, are used as $\Psi(t)$ in the equation 2.17 for $t = T$ instead of the limiting variable t which approaches infinity. The pseudo codes for Govorukhin's code and the alternate code using Floquet multipliers are presented in the appendix B.

The above algorithm outputs cumulative average of the variation as the Lyapunov exponents as the time progresses (see appendix B). To investigate the role of synaptic terms of the variational equations in defining the largest Lyapunov exponent, the sum $S = S_1 + S_2$ in 2.14 is cumulatively averaged as well. In other words, at every time step along with the Lyapunov exponents an output for the sum S is produced, which is denoted by $\bar{S}(t)$. Similar to the computation of Lyapunov exponents at every time step the value of S is added to the sum of the previous ones and divided by the time elapsed since the beginning. Stated mathematically, $\bar{S}(t) = 1/t \int_0^t S(r)dr$. As the Lyapunov exponents and the $\bar{S}(t)$ continue to oscillate with slowly decaying amplitudes, they are further averaged to obtain estimates of the settled values for each parameter combination (for examples

see 3.5 and 3.6). The duration of the time steps, total time and non-transient averaging time chosen for optimum settled values are based on the comparisons shown in the figures 2.8 and 2.9.

2.3.2 Phases and Phase Differences

The algorithm for identifying phase differences between the bursting neurons of the HCO is based on the observation that solutions of the two neurons belong to the same orbit. The neurons in the weakly coupled HCOs are identical and the weak reciprocal inhibitions perturb their trajectories small enough that they remain nearly identical in the phase space. In addition, because of the strong convergence to stable periodic orbit from neighboring points in the phase space, small perturbations diverge along the periodic orbit the most. Therefore, the trajectory of each neuron passes through a reference point contained in the periodic orbit but with some delay.

The reference point is set to be on the auxiliary threshold $\Theta_{\text{th}} = -0.0425$ V (see figure 2.10A), halfway between the spiking and quiescent voltage values. The phase of the bursting neuron is initiated/reset every cycle after the voltage, $V(t)$, increases above Θ_{th}. The phase lag, $\Delta\phi^{(n)}$, on the n-th bursting cycle is defined through the delay, τ_n, between the burst initiations $V_1(t_n) = \Theta_{\text{th}}$ and $V_2(t_n+\tau_n) = \Theta_{\text{th}}$ (see figure 2.10B), which is further normalized over the recurrence period, $T^{(n)} = t^{(n)} - t^{(n-1)}$, of the HCO. The pseudo code for the algorithm is presented in the appendix B. A detailed account of the routine for the computations of the sequence $\{\Delta\phi^{(n)} = \tau^{(n)}/T^{(n)}\}$ is given in [55].

Due to symmetry imposed by the identical neurons and synaptic connections, the same phase difference may occur in two distinct configurations, either neuron 1 or neuron 2 is delayed. Phase-advance with respect to neuron 1 correlates to phase-lag with respect to neuron 2. Hence, results of phase-advances and phase-lags are symmetric. So, it is sufficient to measure only the phase-lags with respect to the reference neuron.

2.3.3 Phase Differences on 3D Torus

The system of ODEs representing the CPG in chapter 5 is numerically integrated and processed by PyDSTool and python packages [71]. Phase-lags are computed as described

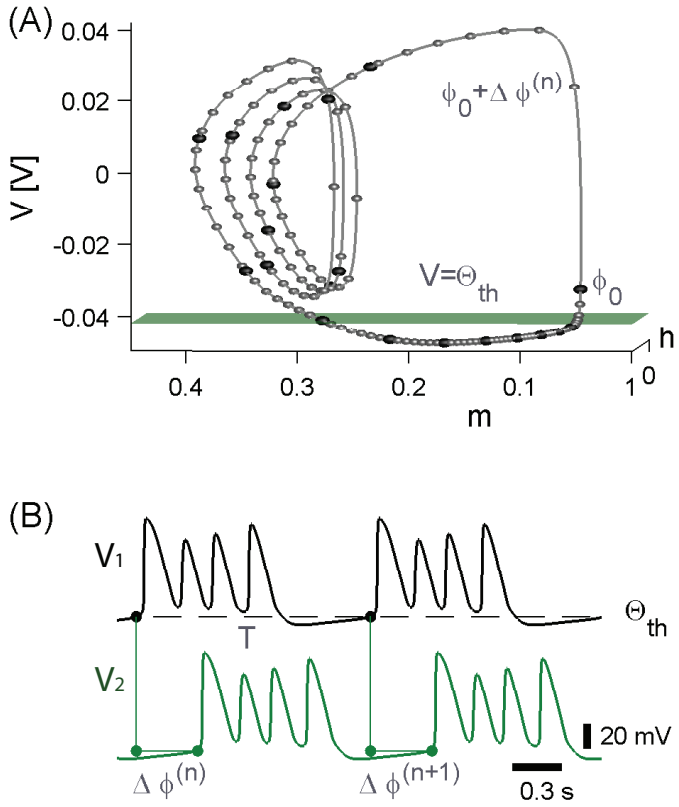

Figure 2.10. (A) Periodic bursting orbit in a 3D projection of the phase space of the leech model HCO. Dark and lighter spheres represent, schematically, the densely distributed initial phases, ϕ_0, for neuron 1 (reference) and, $\phi_0+\Delta\phi^{(0)}$, for neuron 2 across the bursting orbit of a normalized 1-period. (B) The sequence, $\{\Delta\phi^{(n)}\}$, for every initial phase lag, $\Delta\phi^{(0)}$, (out of 7,200) is identified from the traces at the instances when the ascending voltage $V_{1,2}$ passes through an auxiliary threshold $\Theta_{\rm th}$ shown in (A).

in the section 2.3.2 by pairing three of the neurons with the fourth in the network. In this process 3-tuple phase-lags $(\Delta\phi_{12}, \Delta\phi_{13}, \Delta\phi_{14})$ resulting from the Poincaré return mappings are obtained. As the time progress, sequences of phase-lags are obtained, which form trajectories indicating the progression of initial phase-lags when connected by lines, shown in figure 2.11. Here, neuron 1 is the reference neuron and maintains the phase-lag $\Delta\phi_{11} = 1$ (see figure 1.9 for illustration). When graphically visualized in Cartesian coordinate, the three phase-lags $(\Delta\phi_{12}, \Delta\phi_{13}, \Delta\phi_{14})$ from the four-neuron network generates a 3D torus (for example, see figure 2.12).

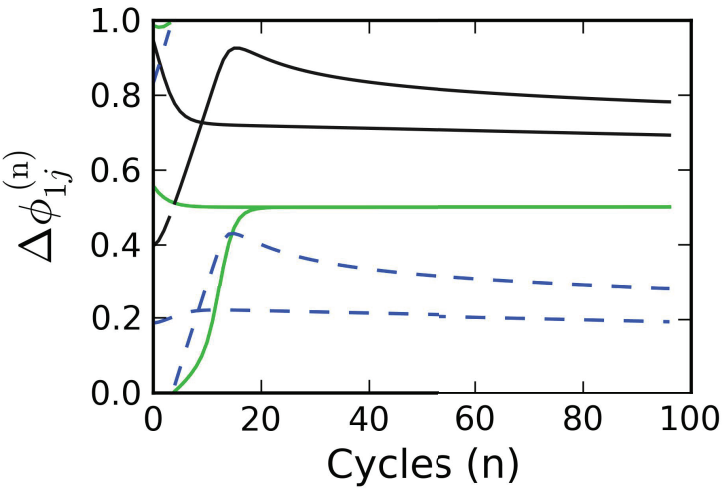

Figure 2.11. Traces of phase-lags with respect to burst cycles. The subscript $j = 2, 3, 4$ corresponding to the colors green, black and blue.

The 3D torus is a unit cube whose opposite faces are identified, so that when a trajectory of the mapping reaches either surface of the cube it emerges from the side opposite to it. Figure 2.11 shows some traces being reset near the beginning of the graphs. The resetting procedure is given in the appendix B. In order to capture all possible network behaviors a dense array of initial phase-lags, green points in figure 2.12, are simulated whose evaluation in the forward time represents the network phase state at every network period. Traces in the figure 2.11 correspond to two initial 3-tuple phase lags (two green dots) in the figure 2.12 at the beginning of the simulation, and to two final ones (two red dots) in the figure 2.12 at the end of the simulation. Thus the Cartesian plot of 3-tuple phase-lags allows one to visualize the network behavior simultaneously

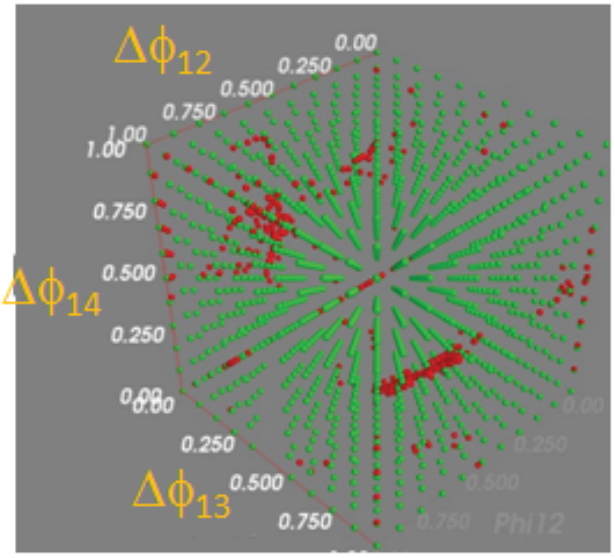

Figure 2.12. Initial (green dots) and final (red dots) distributions of 3-tuple phase-lags in *Melibe* CPG for a 60 cycles long simulation. Author acknowledges undergraduate mentee Dane Allen for this figure.

from a large set of initial conditions. The figure 2.12 only shows initial and final phase-lags after a number of cycles, however plots of these points at intermediate cycles would reveal the transience, hence the convergence and the divergence properties of the network steady states.

Chapter 3

SPIKE SYNCHRONY ANALYSIS:

The stability analysis of spike synchrony of bursting neurons, forming various networks, is presented in this chapter. The terms 'spike synchrony' and 'in-phase synchrony' are used interchangeably in this chapter. Through the examination of the variational equation, properties of the network models, with fast, non-delayed synapses, that make spike synchrony stable are distinguished. It is found that *reciprocal inhibition can cause both in-phase and anti-phase bursting to exist for the same parametric regime*; an example is shown in figure 3.1. This result extends the classical results of spiking neurons which show that mutual inhibitory connections cause activity of one neuron to block the activity of the other, leading to the anti-phase network activity, where each neuron must take turn to be active. This sequential activity is referred to as the anti-phase bursting.

The coexistence of the two attractors mean that there are two separate attraction basins, which are identified and shown to have non-smooth boundary between them; some examples are shown in figure 3.2. The findings indicate initial preparations, under which experiments are conducted, are critical for defining the outcome. By the same token, the circumstance under which CPG receives input should then dictate the behavioral output.

Another critical feature that is elucidated through the analysis presented in this chapter is that the spikes in the endogenously bursting neurons contribute to stabilize the in-phase synchrony. This contrasts the solely desynchronizing property of relaxation oscillators, which are often used to model bursting cells where the spikes are omitted [19, 31]. Relaxation oscillators have monotonic depolarized state as opposed to square wave bursters, which have depolarized oscillatory (non-monotonic) state in addition to monotonic hyperpolarized state. The depolarized state of the neuron is generally referred interchangeably as the active phase, the spiking phase. The ratio of the duration of the active phase and the period is termed the duty cycle. During the active phase of a

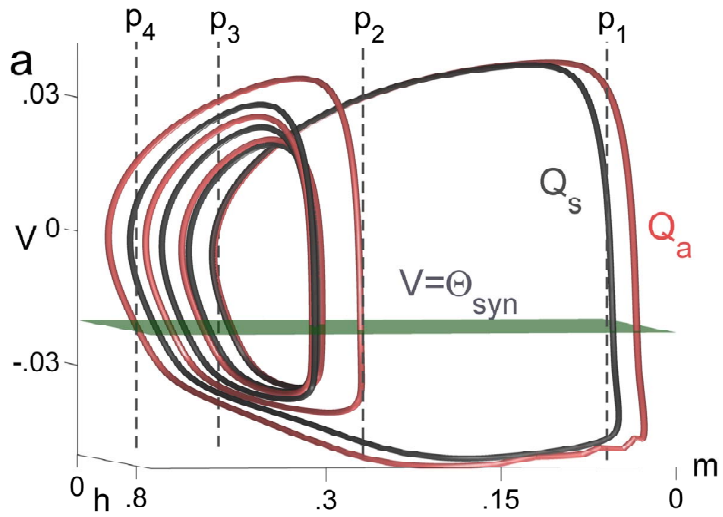

3.1.1

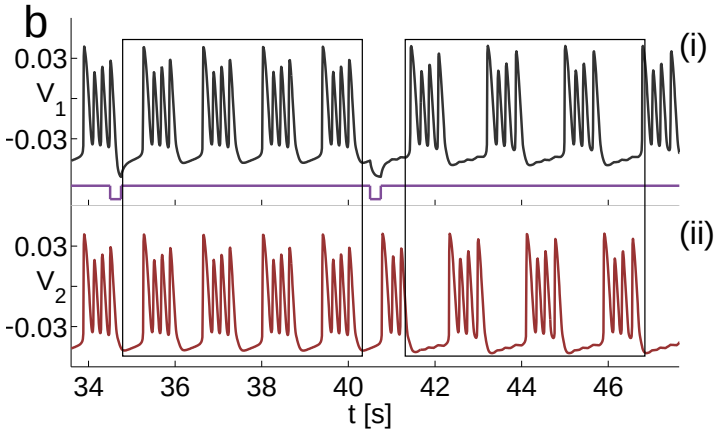

3.1.2

Figure 3.1. Co-existing stable in-phase (Q_s) and anti-phase (Q_a) bursting orbits in the phase space of (2.2) at $g_s = 0.7$, $\Theta_{syn} = -0.02$ and $V_{\text{K2shift}} = -0.0215$. Voltage cuts p_i, $i = 1..4$ reveal the V-range of attraction basins (shown in 3.2) of in-phase bursting at the periodic orbit's various phases (3.1.1). Voltage traces showing the robustness of in-phase bursting against an external pulse perturbation during the spiking period, and its vulnerability, leading to anti-phase bursting, during the quiescent period of bursting (3.1.2).

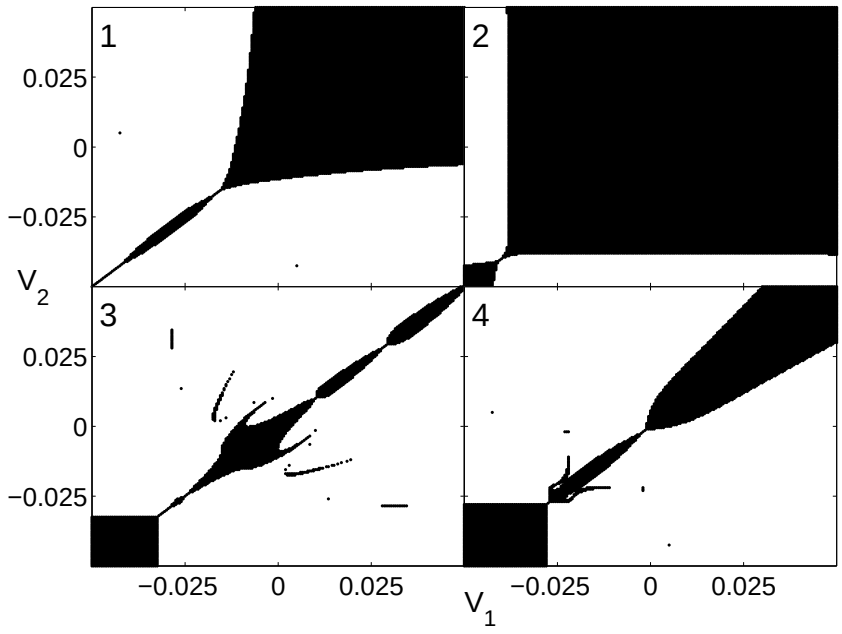

Figure 3.2. Basins of attraction corresponding to the stable synchronous trajectory in the leech HCO. The four basins of attraction (synchronization zones) in the (V_1, V_2) plane are calculated by choosing different V_1 and V_2 along the four vertical lines p_1, p_2, p_3, p_4, depicted in (3.1), that correspond to four fixed values of the gating variables $m_1 = m_2$ and $h_1 = h_2$. Here, $g_s = 0.4$, $\Theta_{syn} = -0.0225$, and $V_{\text{K2shift}} = -0.022$. Black points indicate the initial values that converge to the synchronous trajectory (the diagonal $V_1 = V_2$), whereas the white regions indicate the attraction basins of anti-phase bursting. Panels 1-2 show that during the spiking phase, in-phase synchronization occurs despite a large dispersion in initial conditions in V and dominates entirely (cf. line p_2) over anti-phase bursting. Panels 3-4: during the quiescence, the basins shrink strongly and become fractal.

pre-synaptic neuron, chemicals (neurotransmitters) are released by the neuron that elicit response in the form of an inward (excitatory) or an outward (inhibitory) current in the post-synaptic neuron. Due to reciprocal synaptic connections, spike interaction takes place when both pre- and post-synaptic neurons are in the active phase.

The suggested mechanism of in-phase synchronization is based on the observation that the neurons in the networks interact through their spikes during their active phases. It is shown that spikes influence the synaptic components of variational matrix in such a way that correlations with stable spike synchrony occurs. This is demonstrated with networks connected by fast, non-delayed synapses. Various cross sections of attraction basins of the leech HCO network show the phenomenon is ubiquitous. Lyapunov exponents are calculated using the variational equations for leech HCO and large networks; the largest Lyapunov exponents are plotted in the (Θ_{syn}, g_s)-biparametric plane, which show broad regions of spike synchrony in these systems. For comparison leech HCOs connected by slow synapses were investigated. In this case, spike synchrony is calculated using voltage variation averaged over long-term and is plotted in the (β, g_s)-biparametric plane, where the parameter β controls synaptic decay - the speed at which synapses inactivate. In what follows, results and analyses for HCOs are presented first, which are sectioned based on two types of connections: fast and slow synaptic connections. Finally, results for large (up to hundred neurons) networks with fast, non-delayed synapses are presented.

3.1 Half Center Oscillators

The common network motif, HCO, is studied for three distinct neuronal and two categories of synaptic models. Unless stated otherwise, the connections are assumed to be symmetric such that $g_{\text{syn}}^{(ij)} = g_{\text{syn}}^{(ji)} = g_{\text{syn}}$ are modeled by the FTM paradigm. The reversal potential is set so that $E_{\text{syn}} < V_i(t)$ at all times t to ensure the inhibitory nature of the current. Specifically, $E_{\text{syn}} = -0.0625$ V is fixed for the leech heart interneuron model, and $E_{\text{syn}} = -0.08$ V is set for the Sherman β-cell and Purkinje cell models, and corresponding value of E_{syn} is -3 in Fitzhugh-Rinzel model. The HCO with individual

neuron model (2.2) was shown to generate robust anti-phase bursting via the hold-and-release mechanism [56], similar to synaptic release [34] in spiking cells.

Any network of identical neurons always possesses a symmetric solution $\{V:\ V_i(t) = V_j(t), h:\ h_i(t) = h_j(t), m:\ m_i(t) = m_j(t),\ i, j = 1..n\}$, corresponding to spike synchrony and governed by the self-connected system known as autapse. This synchronous solution is unstable in the absence of appropriate form and strength of coupling. Computer-assisted verifications aimed to examine the robustness of in-phase synchronization are of four categories: (1) application of small amounts of current to one of the neurons in the HCO at different times in the numerical simulations; (2) introduction of variation in membrane potential, while other variables are fixed at that of the synchronous solution; (3) introduction of variation in the phases along the bursting orbit, and (4) numerical evaluation of Lyapunov exponents using variational equations for the transversal perturbations to the synchronous solution [10]. All of the approaches have been used for leech HCOs with fast, non-delayed synapses and selected few have been applied to other networks to test the generality hypothesis for the in-phase synchronization of the bursting networks.

3.1.1 Fast, Non-delayed Synapse Coupled HCOs

In leech HCOs, approach (1) demonstrates coexistence of in-phase and anti-phase synchrony, shown in figure 3.1(b). The pulse of current applied is shown in the middle of the two voltage traces. At different times within a cycle, perturbation caused by the applied current leads to either persistence or loss of the in-phase synchrony. Samples resulting from approach (2) are shown in figure 3.2, which depicts in-phase synchrony with black dots, meaning the voltage variation corresponding to the black area results in spike synchrony. Figure 3.3 shows the variations of the synchronization zone (shaded) as the neurons transition from the silent phase to spiking, uncovered by approach (3). The synchronization zone, identified with the third alternate approach, is consistent with the results of figure 3.2 and confirms that in-phase synchronization is quite robust and achievable during the spiking phase of bursting. However, small variation introduced during the silent period will likely lead to anti-phase bursting. The third approach has

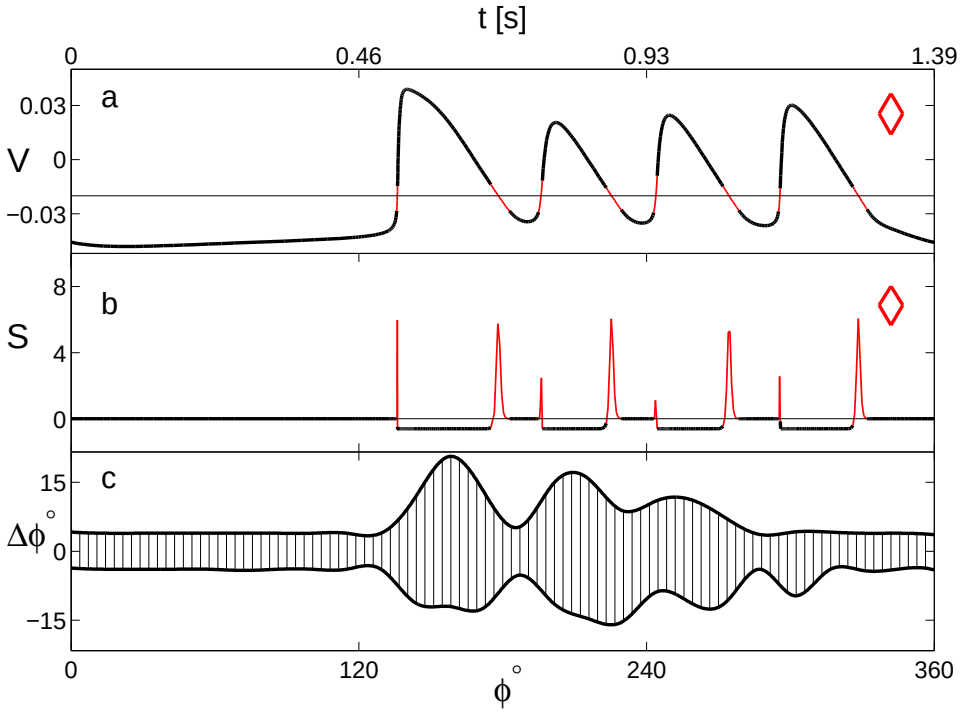

Figure 3.3. Analysis of synaptic terms in variational matrix for the leech HCO. (a) Voltage trace of four-spike synchronous bursting. Its red (thin) and black (thick) segments indicate positive and negative instantaneous values of the largest transversal Lyapunov exponent $L_{\max}^{\text{inst}}$. (b). Synaptic term $S = S_1 + S_2$. Note sharp positive peaks in S, corresponding to the appearance of the desynchronizing term S_2, when the bursting orbit crosses the synaptic threshold Θ_{syn}. The wide negative plateaus in S are caused by the stabilizing term S_1 and coincide with the upper part of the bursting trajectory. For the given threshold $\Theta_{syn} = -0.02$, S_1 wins over S_2 and defines the overall synchronizing effect of coupling. The corresponding averaged value of S is depicted by $\diamond$ in 3.4b. (c) Shape of the synchronization basin (dashed) along bursting, parameterized from 0° through 360°; 0° corresponds to the beginning of its quiescent period. Its boundaries correspond to evolutions of unstable fixed points on the orbit which separate the basin from anti-phase bursting. Tonic spiking period of bursting corresponds to the widest synchronization zone (cf. 3.2), while it becomes more fragile during the quiescent period: exceed of 5°, or advance of either cell's state, leads to anti-phase bursting.

been applied to HCOs coupled by four paradigms of fast, non-delayed synaptic models. The results, shown in figure 4.13, indicate that regardless of the paradigm, synchronization zones are preserved. In-phase synchrony is measured two ways, deviations of either voltage or phase values, which are delineated by the two color bars in the figure. In addition, this approach is applied to HCOs, composed of Sherman pancreatic $\beta-$cells, Purkinje neurons, and Fitzhugh-Rinzel models connected by FTM synapses. The results of the first two cases are presented in the figure 3.9, which shows more irregularities but significant sizes of the synchronization zones. For Fizhugh-Rinzel HCO, very little synchronization zones are observed for the parametric regime considered (figure 3.7). However, (Θ_{syn}, g_s)-biparametric diagram indicates non-trivial synchronization zone is possible (figure 3.8).

Finally, the approach (4) is considered, which uses variational equations 2.14 presented in chapter 2 for the HCO configuration. Spike synchrony is a steady state, located at the origin, of the ODEs defined by the variational equations. As a result, when $S_1 \leq 0$ it *stabilizes* the steady state of 2.14. More precisely, $S_1 < 0$ after the membrane potential $V(t)$ goes over the synaptic threshold Θ_{syn}, as in the case of excitatory coupling in [10]. On the other hand, $S_2 \geq 0$ due to $(V - E_{\text{s}}) > 0$. The partial $\Gamma_V(V - \Theta_{\text{syn}})$ reaches a positive and high amplitude peak at $V = \Theta_{\text{syn}}$ and then rapidly decays away from the threshold. Consequently, $S_2\xi$ tends to destabilize steady state at the origin every time the membrane potential $V(t)$ gets close to Θ_{syn}. In simple terms, the inhibition has a *dual* role in stabilizing and breaking in-phase synchronization as the terms S_1 and S_2 compete with each other to make the synchronous solution stable versus unstable. The overall outcome depends on various quantitative factors including the coupling strength and the level of the synaptic threshold.

Whenever the phase point (depicted by spheres in figure 2.10), corresponding to the instantaneous state of one cell, gets close to the threshold Θ_{syn}, the other cell receives a strong, short-term desynchronizing kick due to S_2 that causes the divergence between the phase points (see figure 4.6 as well). Once both rise above the threshold, the inhibition switches into a synchronizing role. Then the phase points receive a weaker though longer lasting synchronizing effect due to S_1. As a result, the phase points converge leading

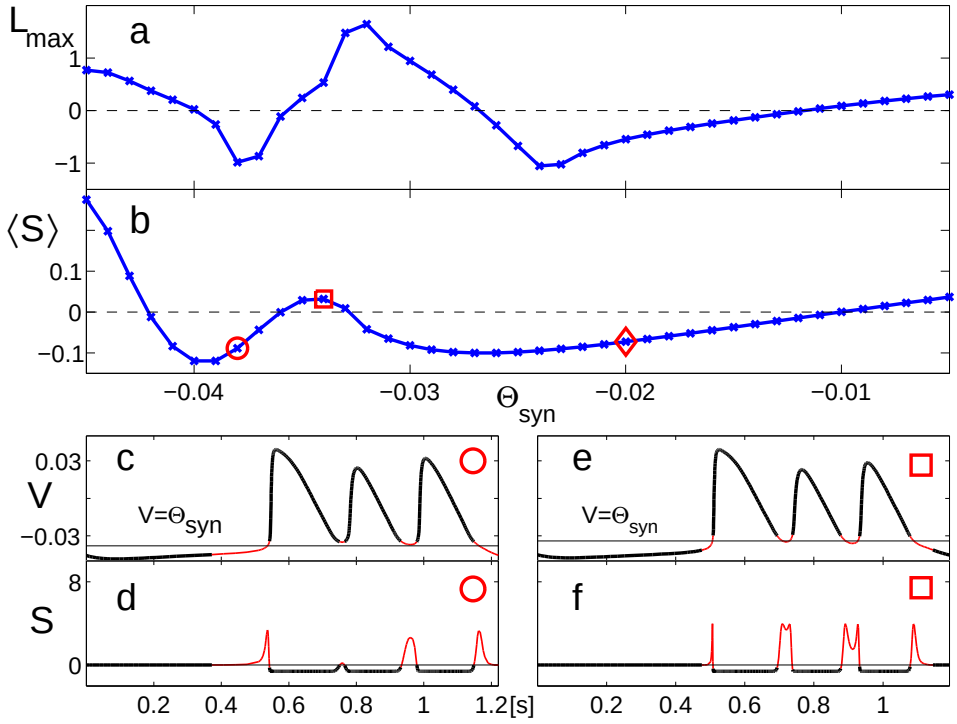

Figure 3.4. (a) Largest transversal Lyapunov exponent, $L_{\max}$, of synchronous bursting plotted against the synaptic threshold Θ_{syn} at $g_s = 0.3$. Note two stability intervals where $L_{\max} < 0$. (b) Dependence of averaged $\langle S \rangle = \langle S_1 + S_2 \rangle$ on Θ_{syn}. Observe the graph of $\langle S \rangle$ closely following that of L_{max} within the physiologically relevant interval $[-0.025\,;0.015]$ for Θ_{syn}. It accurately predicts the critical threshold $\Theta_{syn} = -0.009$ beyond which in-phase synchronization breaks down. Insets (c,d) and (e,f) are similar to Figs. 3a-b and relate to the thresholds Θ_{syn} marked by the circle and the square in (b), corresponding to stable and unstable in-phase synchronization, respectively. When the spikes hit Θ_{syn} transversally [(c-d) and Figs. 3a-b], the impact of S_2 is weaker, so that $\langle S \rangle$ remains negative long enough to ensure stable in-phase synchronization. When Θ_{syn} touches spikes from below (e-f), the desynchronizing term $\langle S_2 \rangle$ lasts longer, thus making $\langle S \rangle$ positive and breaking in-phase synchronization down.

to synchrony (illustrated in figures 3.3a-b). The threshold value Θ_{syn} and the synaptic strength g_{s} are two crucial factors determining the stability of the zero equilibrium state in the variational equations (2.14), and hence the stability of spike synchrony. It is noted that the choice of Θ_{syn} affects the balance between the competing terms S_1 and S_2 and may reverse the overall contribution of the coupling from negative to positive and vice versa. That is raising the threshold closer to the upper part of the spikes lowers the contribution of the stabilizing term S_1 and leads to anti-phase bursting in the network (see figures 3.4-3.6).

It is worth noticing that the values of Θ_{syn} from the left interval of stability (see figure 3.4a) range from about -0.038 to -0.036 in the leech HCO. For these values, the threshold Θ_{syn} is placed below the minimum value of spikes and cannot intersect the bursting part of the trajectory and hence cannot account for the presence of spikes in the presynaptic cell. As far as the synaptic coupling between the cells is concerned, this location of the synaptic threshold Θ_{syn} implies an interaction that is similar to that between spiking (non-bursting) cells [19]. For such a low threshold, the synaptic

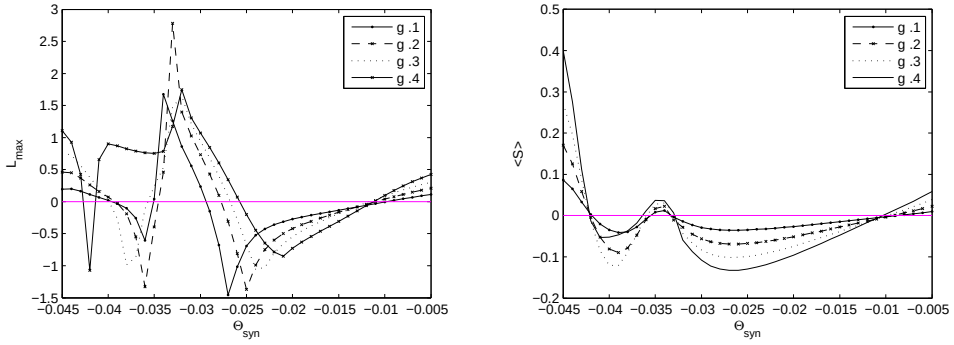

3.5.1 3.5.2

Figure 3.5. Cross sections of (Θ_{syn}, g_s)-parametric contour plot of largest Lyapunov exponent, shown in figure 3.6, and corresponding traces for average synaptic terms, $\langle S \rangle$, in the variational matrix, reveals two correlated intervals of negative values that corresponds stable spike synchrony.

coupling is always switched on when the system is on the bursting manifold and switched off when the system is on the silent branch of the solution. Stable synchronization observed in this interval is fragile. Lowering the threshold closer to the silent part switches

on the destabilizing term S_2 in such a way that the effect of S_2 becomes significant. Therefore, the synchronous solution receives a long lasting desynchronizing impact during the quiescent part and destabilizes. At the same time, the right, physiologically relevant interval of Θ_{syn} corresponds to the spike interactions during the active phase of bursting, and therefore to more robust synchronization.

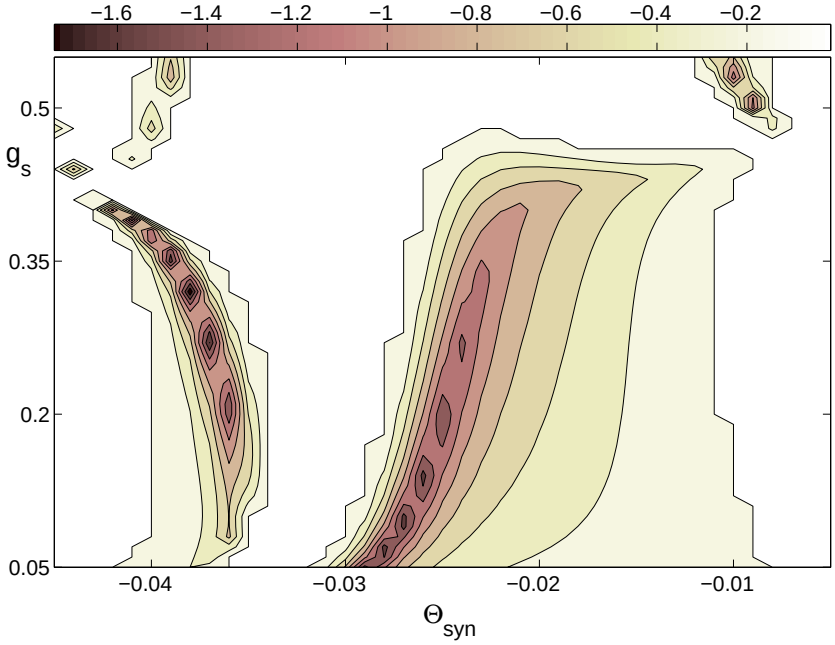

Figure 3.6. Stability islands for in-phase synchronization in the (Θ_{syn}, g_s)-parameter diagram. Level curves of the Lyapunov exponent $L_{\max}$ show two large islands of stable synchrony, where $L_{\max} < 0$. Darker shading (top color bar) corresponds to smaller values of $L_{\max}$. Note that the vertical axis scale does not extend down to $g_s = 0$. The Lyapunov exponent $L_{\max}$ can still be negative below the level $g_s = 0.05$, however its values are close to 0 and sensitive to the choice of the integration method.

Figure 3.6 shows a two-parameter diagram of the stability of synchronization as a function of parameters Θ_{syn} and g_s in the leech HCO. Given a fixed threshold Θ_{syn}, providing stable synchronization for certain values of the synaptic coupling g_s, increasing the synaptic strength at first has a general tendency to make synchronization more stable. However, once a certain strength of inhibition is reached, the inhibition starts desynchronizing the neurons. Indeed, an increase in g_s makes the individual self-connected system more unstable, therefore the dominance of the stabilizing term S_1 over S_2 is no longer sufficient to synchronize the neurons.

It is important to stress that the *evaluation of the averaged synaptic term from the variational equations 2.14 predicts the synchronization threshold rather precisely* and serves as the necessary quantitative condition for stable in-phase synchronization. This calculation is particularly important for the bistable network where co-existing anti-phase bursting typically dominates over in-phase synchronization such that it is easy to come to the wrong conclusion that in-phase synchronization is always unstable, relying only on numerical calculations from random initial conditions. Indeed, if one cell is initially in the spiking phase, whereas the other is silent fast, non-delayed reciprocal inhibition between the cells leads only to anti-phase bursting. However, if the cells start firing in the spiking phase, then the inhibition, instead of diverging them, will force the cells' states to come together, resulting in stable synchronized bursting. Note that once anti-phase bursting is achieved, it remains highly resistant to external voltage perturbations of either cell. On the contrary, a weak common inhibition applied to both cells can break the anti-phase regime and make the cells burst together [56] so that the reciprocal inhibition between the cells could synchronize them.

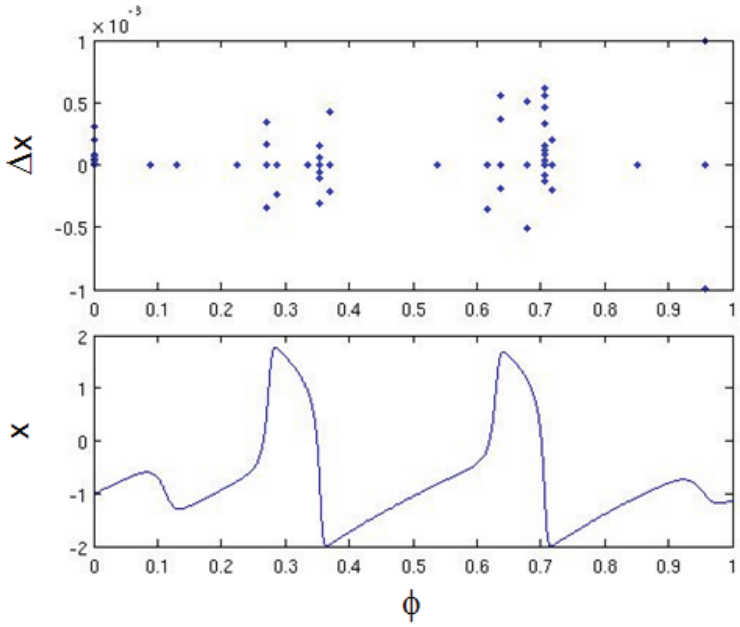

Figure 3.7. Synchronization zone along periodic orbit in the phase space for Fitzhugh-Rinzel HCO, with $g_s = 0.0001$. Only complete (spike) synchrony is measured. Algorithm for burst synchrony is not applicable.

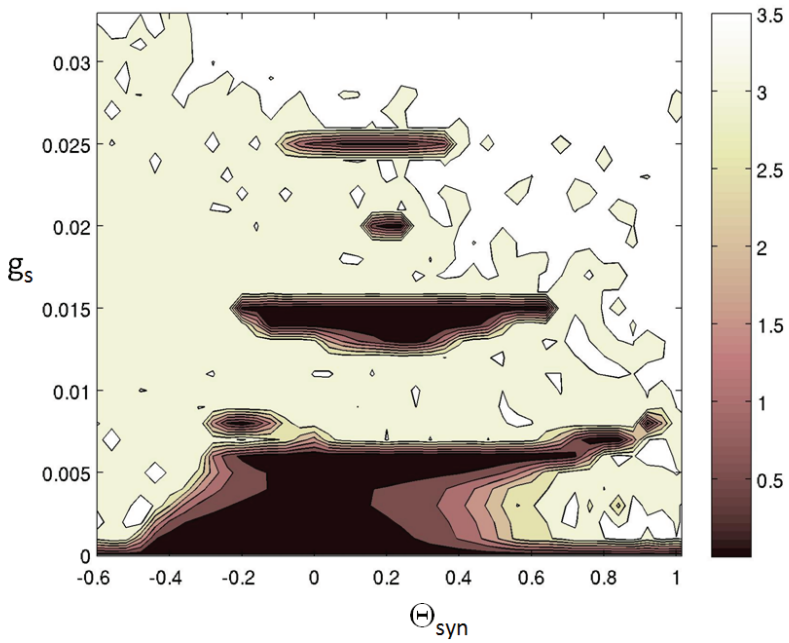

Figure 3.8. Biparametric (Θ_{syn}, g_{syn})-diagrams depicting stability zones (dark) of in-phase bursting in the Fitzhugh-Rinzel HCO. Color bar measures maximum absolute deviation in the values of x variable, after transients have been removed.

The synchronizing effect of fast non-delayed reciprocal inhibition is defined by the intrinsic property of the fast synaptic coupling to act differently on the synchronization trajectory, depending on whether the trajectory crosses or is above the synaptic threshold. This property is linked to the presence of the two competing terms S_1 and S_2 in the variational equations. In this context, it is generic and applicable to other Hodgkin-Huxley-type neurons, exhibiting different types of bursting. In support of this claim, we have examined the synchronization properties of the network (2.6), composed of two coupled (i) Sherman pancreatic β-cell models [52], displaying square-wave bursting; (ii) Purkinje bursting cell models [53]; and (iii) FitzHugh-Rinzel elliptic bursters [62]. In the first two networks, it is observed that stable and robust in-phase synchronization co-exists with anti-phase bursting (figure 3.9). The elliptic bursters tend to synchronize poorly due to the delayed loss of stability property. Small variations may cause difference in the numbers of spikes causing spike synchrony less achievable (figure 3.7). Nevertheless, this class of bursters are very important to study as many biological neurons produce bursts

that have close resemblance to that of the elliptic bursters and their HCOs may conform to less stringent but more experimentally relevant condition for synchrony.

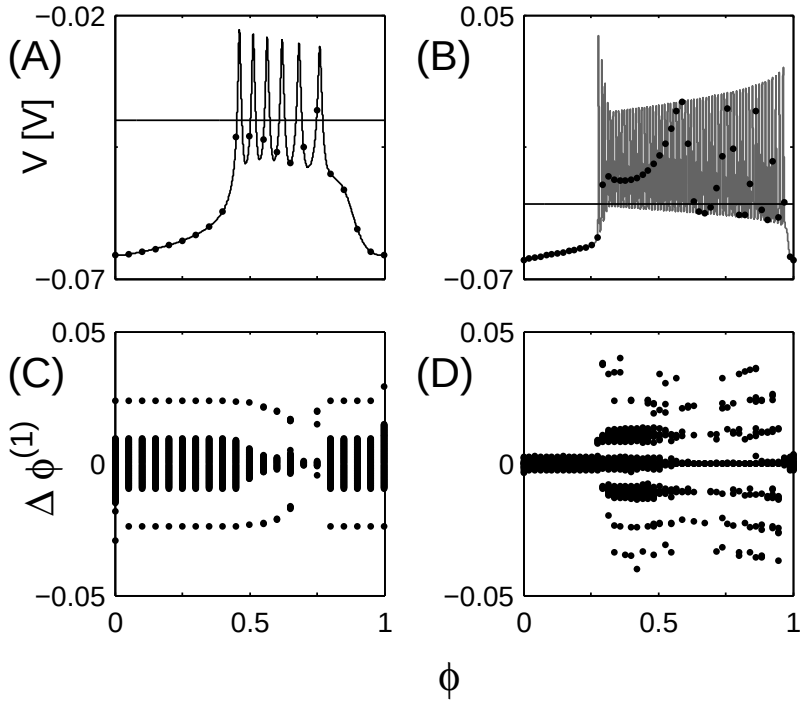

Figure 3.9. Synchronization zones for pancreatic-β and purkinje HCOs, where complete in-phase synchrony is achieved. (A-B) Voltage traces of single complete bursts for HCOs composed of pancreatic-β and purkinje neuron models, respectively. The dots indicate reference phases for estimating synchronization zone. Horizontal lines represent synaptic thresholds. (C-D) Initial phase differences, $\Delta\phi^{(1)}$, that lead to complete in-phase synchrony are shaded dark, corresponding to the traces above. Reference phases correspond to each vertical bars, which may be discontinuous.

The persistence of robust in-phase synchronization in the leech HCO is also verified, after the synaptic FTM function was replaced by the Heaviside function [31] and more common alpha-dynamical function; and by a precise dynamical model of fast synapses, wiring the heart beat central patter generator of the leech [23](figure 3.10). In the latter case, the synapses are non-instantaneous, yet fast so that the impact of inhibition on synchronization is identical to those of the instantaneous FTM coupling. Synaptic current traces generated by the various paradigms are shown in 2.1 for comparison. The robustness of in-phase synchronization with respect to mismatches in the synaptic strengths and the intrinsic parameters of the cells is also tested. Perfect synchronization

is no longer possible in these cases due to symmetry-breaking, which leads to the fact that the spikes within the synchronized burst do not coincide anymore. In all simulated cases this burst synchronization has been verified to be robust for $5 - 10\%$ mismatch in the synaptic strengths, presented in chapter 4. The main results and analysis presented

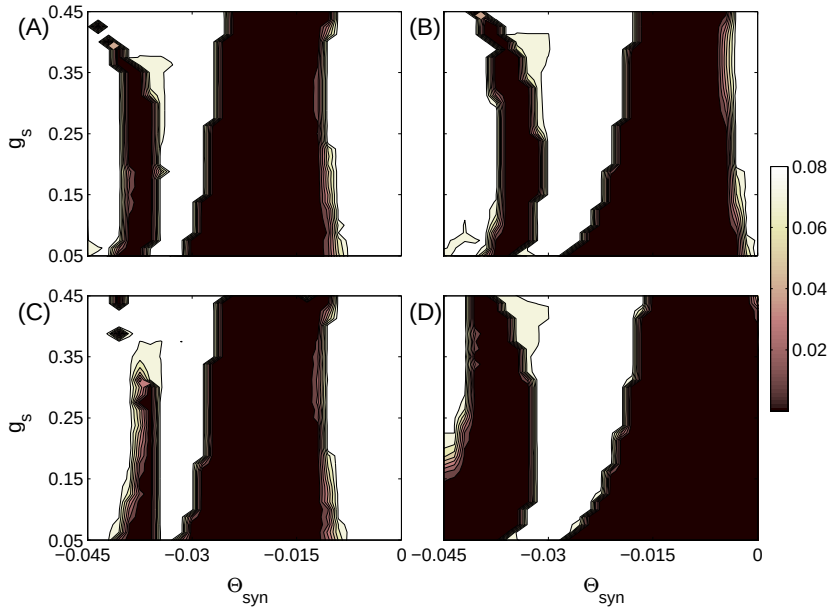

Figure 3.10. Biparametric (Θ_{syn}, g_{syn})-diagrams depicting stability zones (dark) of in-phase bursting in the leech HCOs connected by various paradigms of fast non-delayed synapses. Here, leech models have parameters regime of (2) in fig. 2.7. (A) Heaviside, (B) FTM, (C) alpha and (D) leech dynamical synapses.

in this chapter have been published in [72].

3.1.2 Slow Synapse Coupled HCOs

In-phase synchrony has been shown to exist for HCOs connected by slow or delayed synapses in the mathematical and computational neuroscience literature. In this doctoral research, α-dynamical synapse is calibrated to match transition from slow, non-delayed to fast, non-delayed synapse (see figure 3.11). Thus far, the choice of parameters α and β that produce qualitative results matching those of FTM synapse connected leech HCO are shown. The use of variational equations is dependent on the type of synaptic terms, which allows for approximation of small variation. Networks with slow synaptic connections are checked for both spike synchrony and burst synchrony by the methods described in the

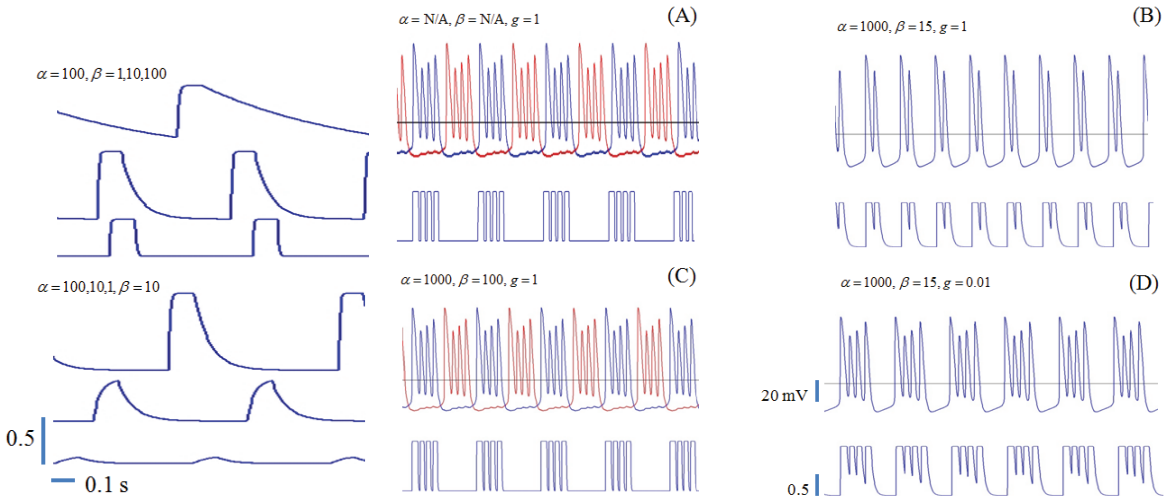

3.11.1 3.11.2

Figure 3.11. Determination of single parameter control, from slow to fast decay, of synaptic current, matching FTM and alpha synapse models in leech HCOs. The traces in 3.11.1, top to bottom, are the results of variation of control parameters α and β, in alpha-synapse with vertical axis being dimensionless synaptic gating variable, $S(t)$. In 3.11.2, voltage and synaptic gating variable traces are shown for specific parameter combinations: (A) FTM synapse, (B-D) alpha-synapse. (C) was chosen as a match for fast non-delayed FTM synapse.

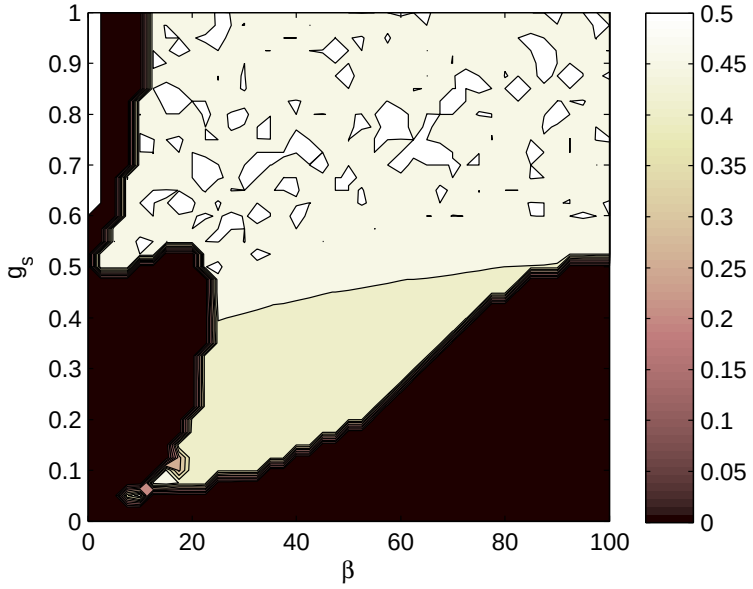

Figure 3.12. Biparametric (β, g_{syn})-diagrams depicting stability zones (dark) of in-phase bursting in the leech HCO connected by alpha-synapses. Right and left edges of the plane correspond to fast and slow synapses, respectively. Color bar indicates phase-lags. Darkest shade closely relate to complete in-phase synchrony.

chapter 2. The (β, g_s)-parameter diagram shows evolution of synchronization zone as the speed of synaptic decay, measured by β, is lowered. Figure 3.12, which is not unique and is dependent on the choice of initial conditions show non-linear transition in such a way that the in-phase synchrony disappears for intermediate rate of synaptic decay for certain coupling strengths. Further investigation is needed to shine light on the cause of this phenomenon.

3.2 Large Networks

The same variational equations 2.14, with small changes, may be used for larger networks as long as individual neuron models remain the same. Each network corresponds to a connectivity matrix that defines coupling configurations among neurons in the network. The variational equations for larger network differ from that of the HCO only by two constants, number of connections per neuron and second largest eigenvalue of the connectivity matrix [10]. In particular, ten local and two global networks have been explored using this approach (see figure 3.13). A general trend of increased synchronization islands is seen with respect to increasing size of the local networks, and the opposite trend is seen for global networks. The magnitude of the largest Lyapunov exponent however decreases as the size of the local network is increased, indicating weaker convergence with respect to the size. The reason for this behavior needs further investigation as well.

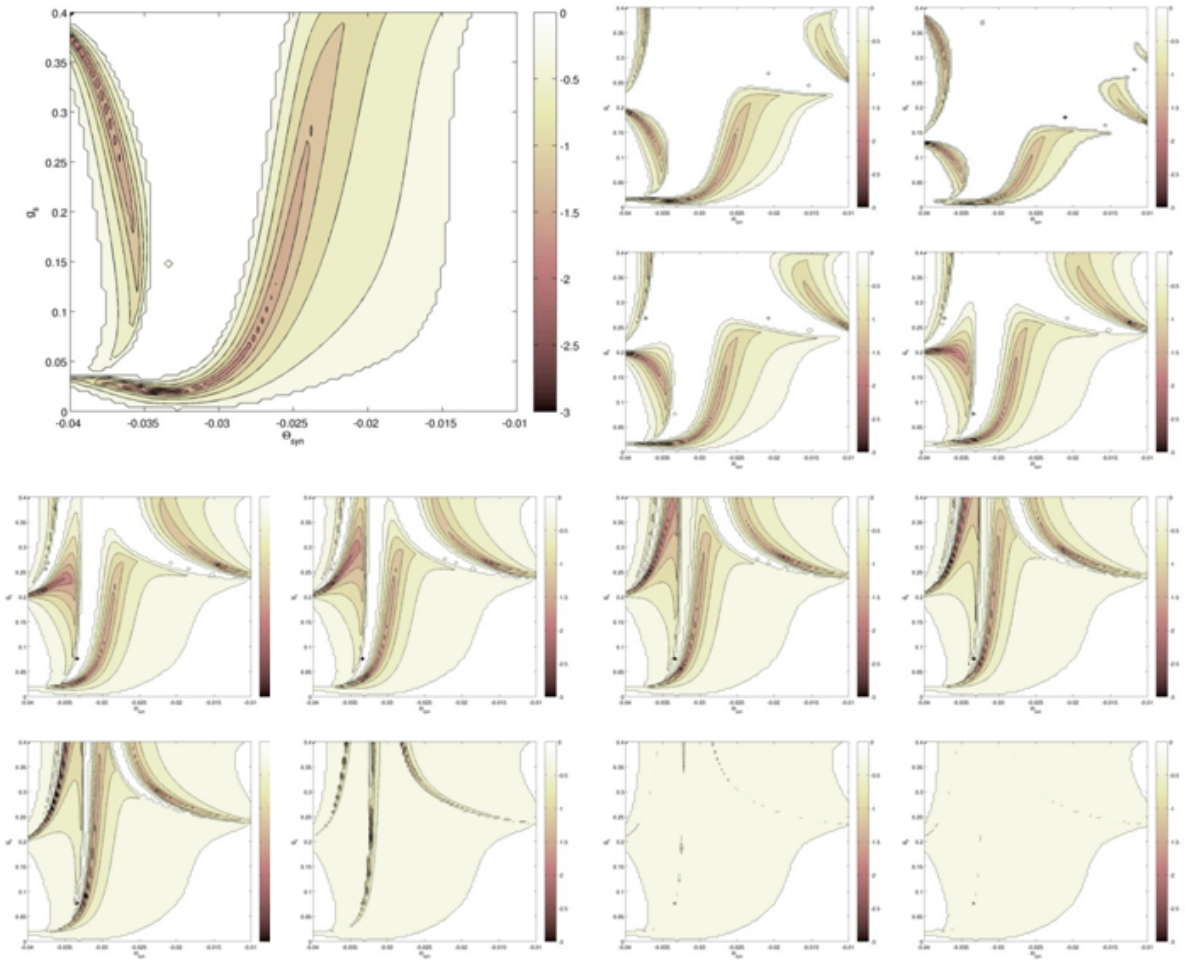

Figure 3.13. Maximum Lyapunov exponent, in $(\Theta_{syn},\ g_s)$-parameter plane, for networks larger than HCOs. Two cell network (largest inset) is reproduced to match the grid sizes and color schemes of reference scales of the larger networks. Remaining insets, row-wise from left to right (from the top), belong to all-to-all connected networks with three and four neurons. Continuing the sequence, remaining insets belong to locally connected networks with $4..10, 20, 50, 100$ neurons.

Chapter 4

BURST SYNCHRONY ANALYSIS

Bursting patterns of neurons have persistent and correlated activities. Phase difference allows one to describe phase-locked states that are neither spike synchrony nor anti-phase synchrony. In addition, in-phase synchrony without spike synchrony is possible. For neurons with approximately equal duty cycles and period, the burst envelopes may align without the spikes in the burst, giving the appearance of correlated burst initiation and termination. For mismatch in duty cycle or period, bursts may still robustly and persistently initiate together, that is with zero phase-lag. From henceforth the term 'in-phase synchrony' is used to mean zero phase-lag between bursts generated by each neuron in the network. Spike synchrony is a subset of the in-phase synchrony defined in this way.

In this chapter, weak and strong coupling is considered, as opposed to slow and fast coupling, considered in the previous chapter. The burst synchrony algorithm, based on the phase-lag, reveals a number of coexisting stable behaviors (multiple phase-locked states) as opposed to just two robust patterns, in-phase and anti-phase synchrony, for weakly coupled networks. Stability is determined qualitatively using convergence or divergence of phase-lag sequences. The algorithm is described in chapters 2 and B, and the results and analysis are presented in this chapter. In addition, a mechanism for multiple phase-locked states is suggested. Other tools such as phase return maps and reversal of stability through inhibition to excitation coupling are employed to analyze the data as well.

4.1 Weakly coupled HCO: Multiple phase-locked states

This section is begun with the HCO (2.6 with $n = 2$) composed of the leech heart interneurons (model 2.2) coupled by weak FTM inhibitory connections (model 2.9). In chapter 3, it has been shown that this HCO bursts, not only in anti-phase as predicted,

but also in in-phase [72]. The weakly coupled HCO possesses multiple, co-existent phase-locked states, in addition to in-phase and anti-phase bursting. In what follows, it is demonstrated that the co-existence of several phase-locked states is due to spike interactions in overlapping bursts.

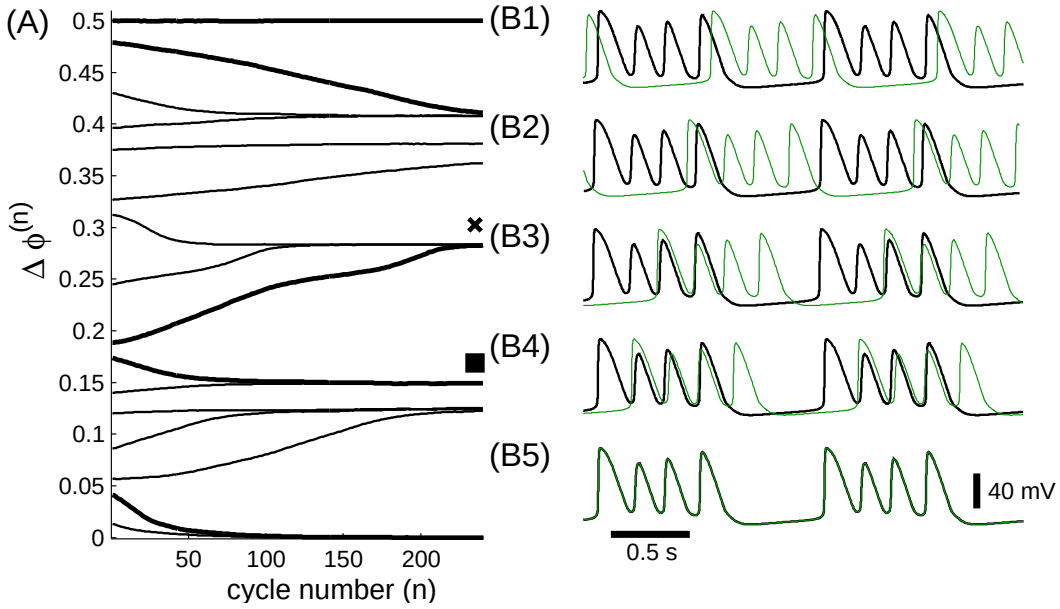

Figure 4.1. (A) Exponential convergence of initial phase-lags to four co-existent phase-locked states over 200 burst cycles of the leech HCO. Parameters are $\Theta_{syn} = -0.0225, V_{\mathrm{K2}}^{\mathrm{shift}} = -0.022$, and $g_{syn} = 0.005$. $\Delta\phi^{(n)} = 0$ and 0.5 correspond to stable in-phase and unstable anti-phase bursting, respectively. The right panel shows the established bursting cycles (dark and light/green colors for neurons 1 and 2, respectively) corresponding to the selected phase-locked states (thick lines in Panel A). Symbols $\times$ and ■ are the same in 4.6.

The case of the weak inhibitory coupling $g_{syn} = 0.005$ between the neurons in the leech HCO is considered. Such weak coupling does not drastically change the phase lags $\Delta\phi^{(n)}$, between the neurons over a bursting cycle thereby allowing one to follow "continuous" evolution of the phase lags, $\Delta\phi^{(n)}$, as the number n, of bursting cycle progresses. One must keep in mind though that such continuous evolution may be hard to achieve when the individual neuron is defined by parameters close to a bifurcation such as the one underlying slow transition from bursting to tonic spiking or silence. Slow evolution of the phase lags however lets one systematically single out all co-existing stable phase-locked states. In addition, the separating thresholds (unstable states) are identified by evaluating the convergence rates given by $\Delta\phi^{(n+1)} - \Delta\phi^{(n)}$.

Figure 4.1A represents the evolution of the phase lags, $\Delta\phi^{(n)}$, plotted against the number of burst cycles, n, for the leech heart HCO generating four-spikes per burst. By assessing convergent tendencies of $\Delta\phi^{(n)}$, as n increases, in the figure one can clearly identify four stable phase locked states (non-linear thick curves), which include the synchronous state, $\Delta\phi^{(n)} = 0$. Unstable states are invisible, but they exist between every pair of stable states. Four unstable states, which include the anti-phase state $\Delta\phi^{(n)} = 0.5$ (top thick curve) are seen. Panel B of figure 4.1 depicts the voltage traces for bursting patterns corresponding to the states, anti-phase (B1) through in-phase (B5).

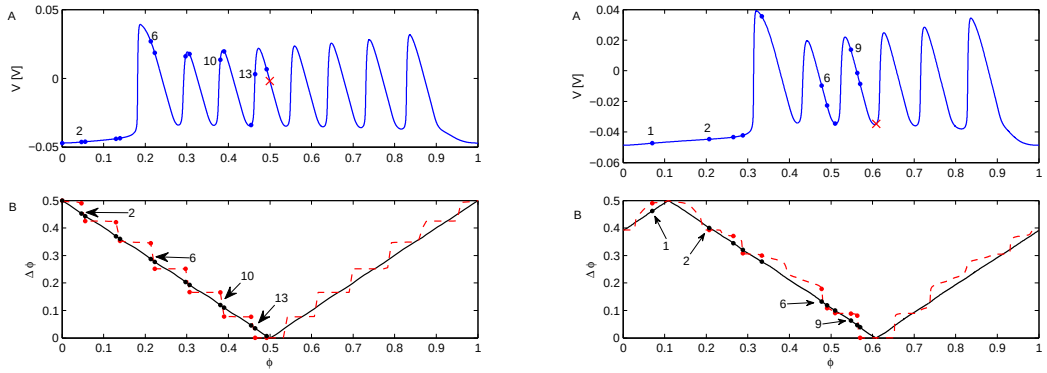

4.2.1 4.2.2

Figure 4.2. Graphs of phase-lags with respect to phases for two different parametric regimes of leech model HCOs. All parameters are same as (2) in 2.7, except $V_{\text{K2shift}} = -0.024$ in both; $I_{app} = 0$ in 4.2.1 and $I_{app} = 0.005$ in 4.2.2. Panel (A) in each show reference burst with dots representing varied (numbered sequentially from the left) and cross representing fixed initial conditions. In panels (B) black lines represent initial phase-lags, red dashed line represent final phase-lags after 40 bursts have elapsed, while numbers correspond to those in panels (A).

A number of examples and methods of quantifications are investigated before a comprehensive explanation for the causes of the multistable states are given in section 4.1.1. Figures 4.2 and 4.3 show phase-lags produce results symmetric to that of phase-advances (see more detailed discussion in the chapter 5). The symmetry is graphically portrayed by the two diagonals with slopes of opposite signs. In figure 4.4.1, the net synaptic currents are averaged for a number of phase-lag trajectories for a leech HCO. All of these traces approach equilibriums or level off over time. Net synaptic currents are also plotted with respect to phase-lags in 4.4.2 to investigate correlations of minima

with stable phase-locked states (red circles). However, net inhibition is not minimized at the phase-locked states.

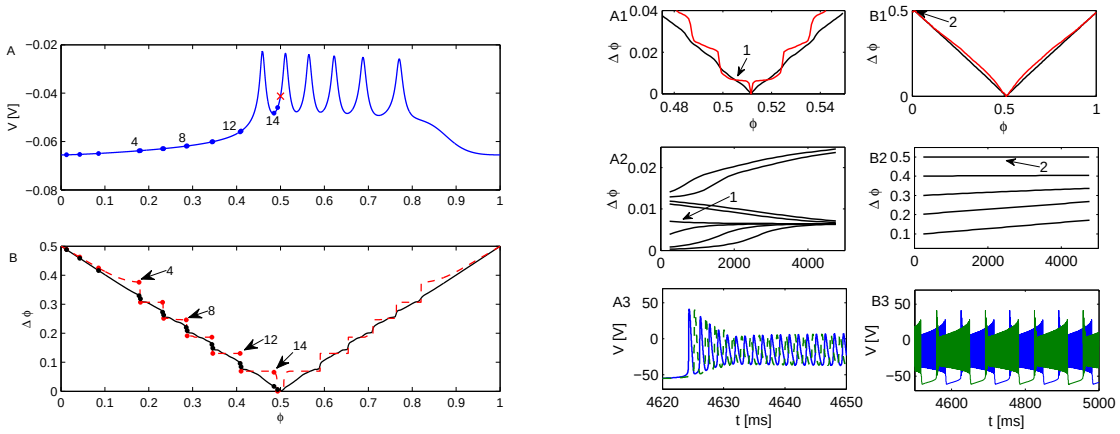

4.3.1 4.3.2

Figure 4.3. Graphs of phase-lags with respect to phases for pancreatic-β and purkinje HCOs. Markers in 4.3.1 (pancreatic-β HCO) has same meaning as those in 4.2. In 4.3.2, the panels (A1-A3, B1-B3) show phase-lag versus phase plot, phase-lag time series, and voltage traces for in-phase and anti-phase synchronous state respectively, for the purkinje HCO.

In figure 4.4.3, $\dot{V}$ from individual neurons is used to compare the rate of change in the coupled versus uncoupled neurons. As expected from the ODEs, coupled neurons (black traces) have smaller rates of change when $\dot{V} > 0$ and larger for $\dot{V} < 0$ compared with the uncoupled neurons (red traces). In an effort to quantify the speed of the phase points L_2 norm is used to cumulatively measure the distance travelled over the elapsed number of burst cycles in the figure 4.4.4. A number of phase-lag trajectories show growing separation between the coupled (blue) versus the uncoupled (green) HCOs. In figure 4.5.1, instantaneous phase of each neuron in the coupled HCOs are graphed. The algorithm which used L_2 norm probably failed to detect distance along the trajectory at times, indicated by the large jumps. Nevertheless, initial phase difference clearly causes differential impact on the motion of the phase points over a burst cycle, indicated by separation between the black and green curves. Duration of common activity, when both neurons spike above the synaptic threshold, is investigated for correlations with phase-

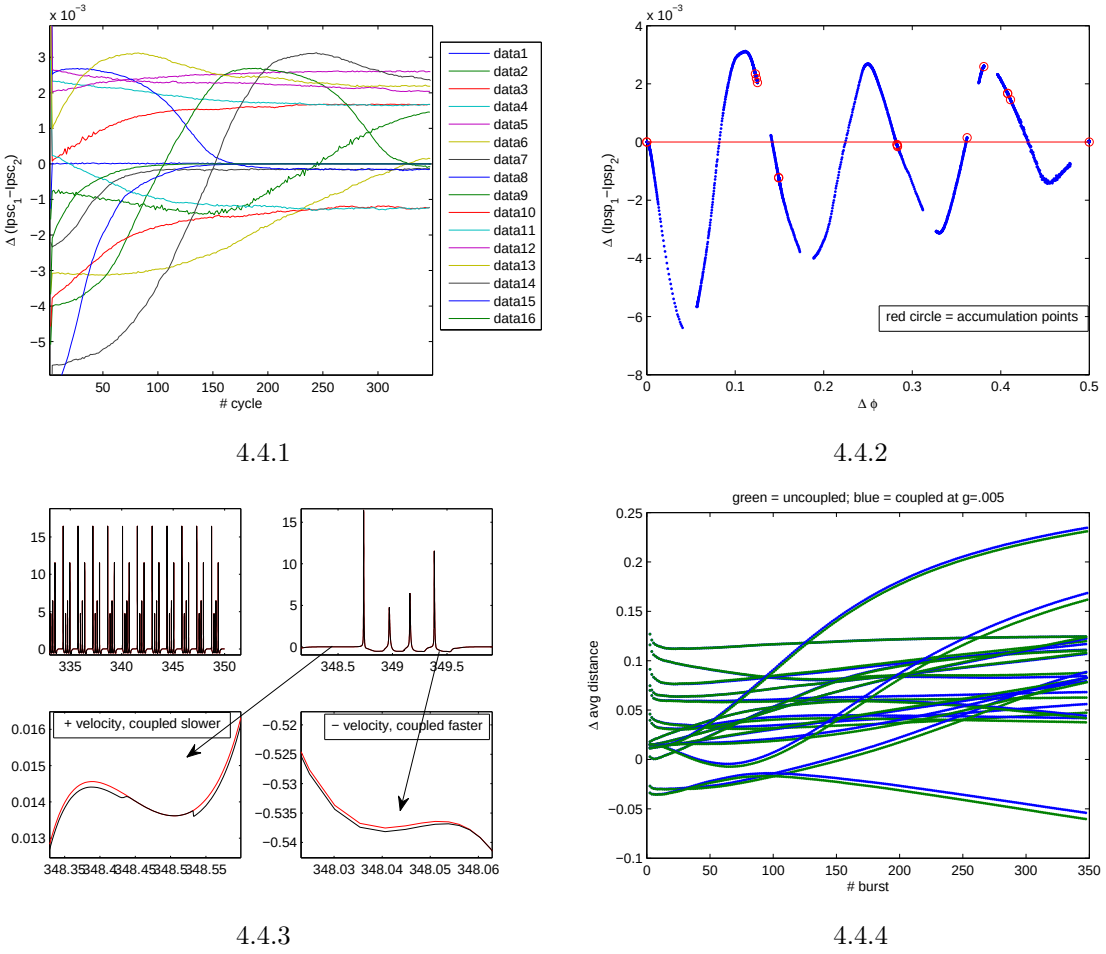

Figure 4.4. Investigation of underlying mechanism of phase-locking using the leech HCO. A number of $< IPSC >$ traces are plotted with respect to time in 4.4.1, and with respect to phase-lags in 4.4.2. The derivative of membrane potential (velocity) is plotted and magnified for weakly coupled (black) and uncoupled (red) HCOs in 4.4.3, and the difference between L_2 norm of the dynamic variables of the two neurons in the HCOs, per burst cycle, is plotted in 4.4.4, where green is uncoupled and blue is coupled case.

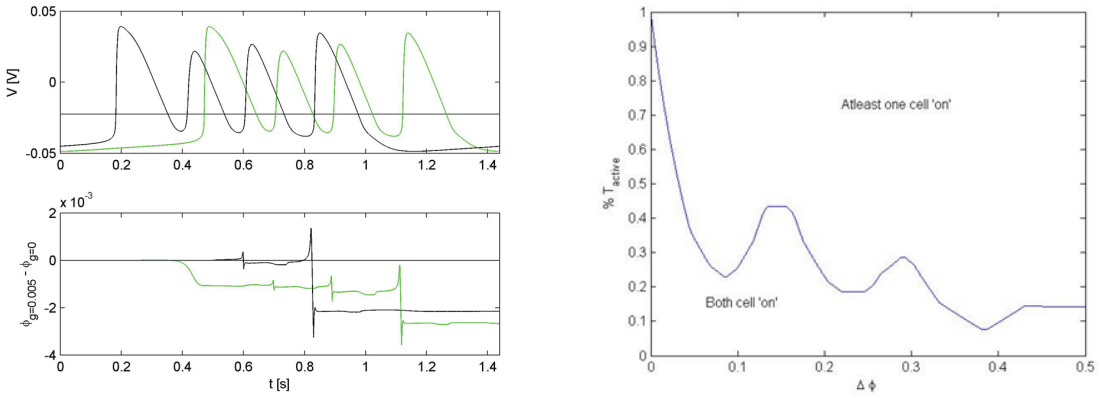

4.5.1 4.5.2

Figure 4.5. Instantaneous phase-lag resulting from spike interaction and duration of active phase per network period. In 4.5.1, voltage traces of individual neurons in the leech HCO is shown, horizontal line indicates level of Θ_{syn}; the panel below corresponds to self-referenced phase-lags with respect to individual uncoupled phases. Green and black traces show spike interaction affects each neuron differently, the underlying reason of resetting the phase-lags between the neurons. In 4.5.2, duration of active phase, time spent by the spikes above Θ_{syn}, is plotted as function of initial phase-lag.

locked states. However, due to non-linear effect of duration of the spike interaction is not a sufficient correlate of the phase-locking phenomena.

4.1.1 The mechanism of multistability: two opposite roles of inhibition

In this section, it is argued that the cause of multistability is a dual role of inhibition. Since the periodic orbit does not significantly deform the shape in the limiting case of the uncoupled network, motion of a phase point along the orbit is tracked. Due to the oscillatory nature of spiking, the inhibition from a pre-synaptic neuron can either speed up the post-synaptic neuron on the downstroke (decreasing further $V' < 0$) or slow it down on the upstroke (decreasing $V' > 0$) as one can see from the modeling equations equations(2.6). Because the inhibition is reciprocal in the HCO, this argument also applies to the other neuron. As a result, depending on timing, the phase lag between the neurons can shrink or widen during the spiking period of bursting, thereby giving rise to multiple phase locked states.

The mechanism is illustrated in figure 4.6A, depicting the momentary phases of the reference neuron 1 on the upstroke (above the synaptic threshold) and the two relative

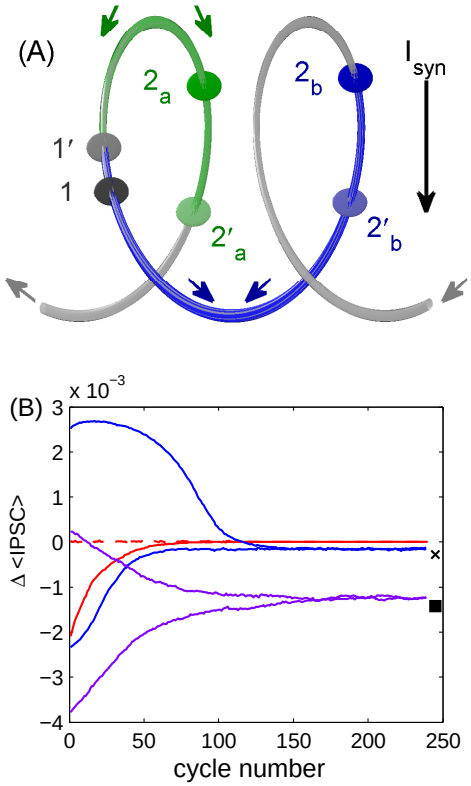

Figure 4.6. (A) Illustration of the dual, slowing and speeding, roles of reciprocal inhibition on evolution of the phase lags during the spiking phase on the bursting orbit, sketched as a helix segment in $\mathbf{R}^3$ with the voltage on the vertical axes. Black (dark) sphere denotes the reference neuron 1 on the upstroke, while lighter (green and blue) spheres denote the instant phases of the neuron 2 on downstrokes. Arrows indicate the direction of inhibition at the current phases of the neurons that make the phase lags widen (upper arch between 1 and 2_a) or narrow (low arch between 1 and 2_b) along the bursting orbit. (B) Transients of the averaged net synaptic current $\Delta\langle \mathrm{IPSC} \rangle$ converging to two non-zero equilibrium levels representing the (B3) and (B4) phase-locked states. Transients (red) converging to the zero level for the stable in-phase (solid) phase locked state, as well as unstable anti-phase state (dashed).

positions of neuron 2 both on the downstroke along the bursting orbit in the active, spiking phase. In the first case, the initial distance (upper arch of the spiking helix) or the phase lag between neurons 1 and 2_a widens because the phase $1'$ is slowed on the upstroke by inhibition from the neuron 2_a while the phase $2'_a$ is accelerated on the downstroke due to the reciprocation from the neuron 1. In the second case, the reciprocal inhibition makes the distance (low arch) between the neuron 1 and 2_b shrink instead, thus narrowing the phase lag (arch between $1'$ and $2'_b$) with each cycle. It is noteworthy to mention that during simultaneous upstrokes and downstrokes, discrepancies in inhibition are less significant. The overall cells' convergence to or divergence from the given phase-locked state depends on the initial conditions that in turn define a fragile balance between the two competing, slowing and speeding, forces over the bursting period.

An average effect of instantaneous spike interactions on phase lags per burst cycle can be assessed from figure 4.6B, showing the dynamics of the net synaptic current, $\Delta IPSC(t) = I_{\rm syn}^{(12)}(t) - I_{\rm syn}^{(21)}(t)$ for several initial phase lags. The vertical axis represents the difference between the average synaptic currents generated by both neurons, $\Delta < IPSC > (n) = \int_{(n-1)T}^{nT} \Delta IPSC(r)dr$, where n and T are cycle number and period respectively. The figure shows that $\Delta < IPSC >$ settles down to a constant value after a number of bursting cycles when a phase-locked state is achieved. The rate of change of $\Delta < IPSC >$ approaches zero when all spikes with a burst are aligned. The attracting phase locked states are represented by the horizonal lines indicating the levels of $\Delta < IPSC >$ on established HCO configurations. While the zero level corresponds to two opposite states: unstable anti-phase and stable in-phase bursting with four spikes, nonzero states correspond to other configurations such as (B3) and (B4) spike offsets marked by $\times$ and $\blacksquare$ in figure 4.1. This presents a very peculiar observation that overlapping bursts can generate non-zero amounts of average net inhibition. In other words, force is required to maintain some of the stable states of the multistability.

In short, *the ability of inhibition to speed up or slow down*, depending on whether the driven postsynaptic neuron is on the down- or upstroke, respectively, is emphasized. Note that the neurons become decoupled during the spiking phase as soon as the voltage drops below the synaptic threshold. When the spikes are aligned, the relative phases

speed up and slow down simultaneously thus causing small variations in the phase lag. As a result, a weak coupling and a high synaptic threshold combined can give rise to the occurrence of multiple phase-locked states. This property is uniquely attributed to bursting cells with spikes as opposed to relaxation oscillator-type neurons without fast spikes that are capable of producing only anti-phase bursting.

4.1.2 Stability diagrams

To analyze and quantify the stability of the phase-locked states (figure 4.1), 1D stability diagrams (shown in figure 4.7) is employed. It represents snapshots of the n-th iterate of the difference between the current and preceding phase lags, i.e., $\left[\Delta\phi^{(n+1)} - \Delta\phi^{(n)}\right]$, plotted against the initial distribution $0 \leq \Delta\phi \leq 0.5$. For dense enough initial distribution, n can be taken as small as 2, which would give a scalar number corresponding to every initial phase lag. Observe that $\left[\Delta\phi^{(n+1)} - \Delta\phi^{(n)}\right]$ can also be viewed as the change rate over a single burst cycle on the n-th step. If the change rate does not vary for some initial phase lag $\Delta\phi^*$, then the latter corresponds to a fixed point of the iterative process. A zero of the graph $\left[\Delta\phi^{(n+1)} - \Delta\phi^{(n)}\right]$ vs. $\Delta\phi$ is a fixed point. The stability of the point is determined by the derivative $d[\Delta\phi^{(n+1)} - \Delta\phi^{(n)}]/d\Delta\phi$ at $\Delta\phi^*$. The fixed point is stable if the derivative is negative, or unstable if the derivative is positive. The basins of the stable states (four total as in figure 4.1) of the HCO network are separated by the unstable ones in this 1D phase portrait. Panel A of figure 4.7 shows the two 1D phase portraits of the leech heart HCO with a weak $g_{\text{syn}} = 0.005$ (black graph), and a stronger $g_{\text{syn}} = 0.01$ (blue/grey graph) coupling. In both cases, the fixed points are located at the same zeros of the graph of $\left[\Delta\phi^{(n+1)} - \Delta\phi^{(n)}\right]$. However, local (in)stability of the fixed point becomes quantitatively stronger with an increased coupling strength.

In addition to local stability, the robustness of the stable phase-locked states can be characterized in terms of the wells of an effective potential. The normalized potential function is computed from the stability diagram in panel A, and is given by the formula: $\Phi^{effective}_{potential}(p) = \sum_{\Delta\phi=0}^{\Delta\phi=p}(\Delta\phi^{(n+1)} - \Delta\phi^{(n)}) / \sum_{\Delta\phi=0}^{\Delta\phi=0.5}(\Delta\phi^{(n+1)} - \Delta\phi^{(n)})$. In panel B, the normalized effective potential plotted against the phase lag distribution $\Delta\phi$, reveals the profile of the potential wells corresponding to the attraction basins of stable states,

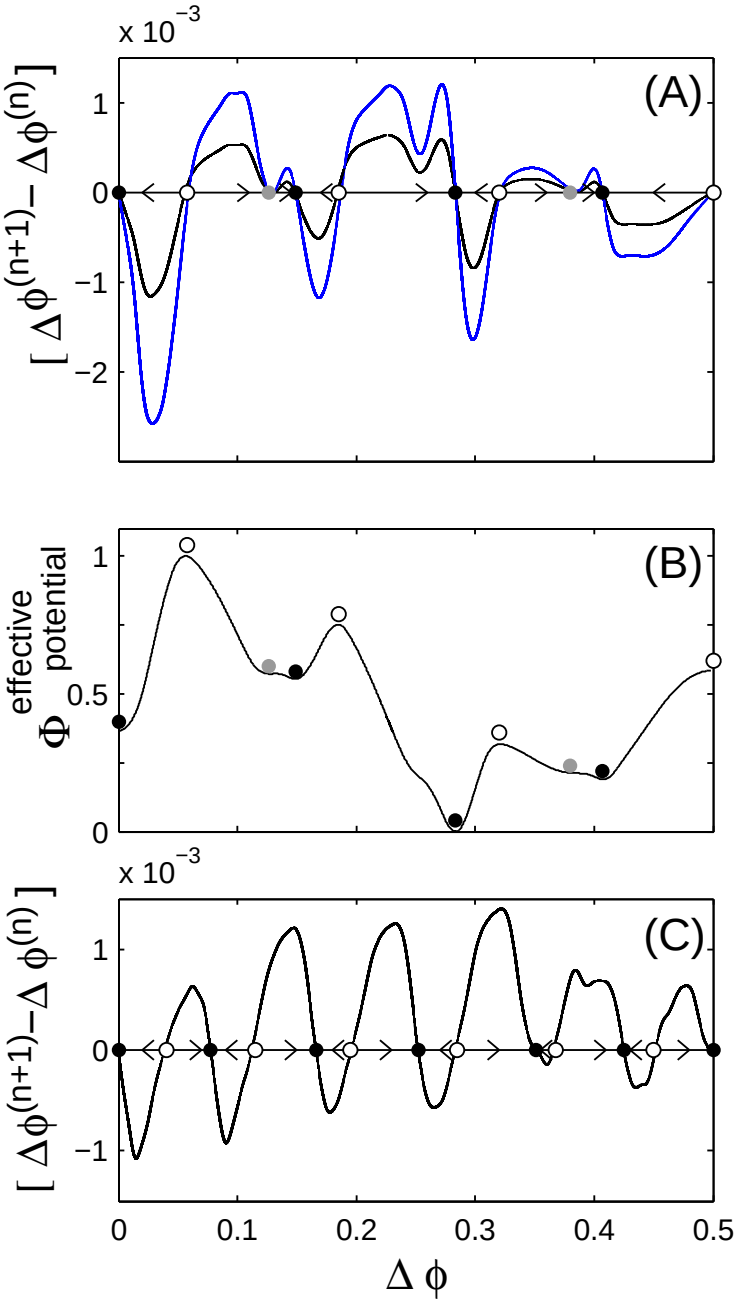

Figure 4.7. (A) Two graphs (black and blue/grey) of the 1D stability diagram: zeros of the stationary distribution of the phase lag difference $\left[\Delta\phi^{(n+1)} - \Delta\phi^{(n)}\right]$ over the range $\Delta\phi = [0, 0.5]$ are phase-locked states: four stable (solid dark circles) separated by repellers in the four spikes bursting HCO at $V_{\mathrm{K2}}^{\mathrm{shift}} = -0.022$ at $g_{\mathrm{syn}} = 0.005$ and $g_{\mathrm{syn}} = 0.01$, respectively. (B) Normalized effective potential (integral) for $g_{\mathrm{syn}} = 0.005$: different wells implying uneven robustness of the stable phase-locked states whose basins are separated by the thresholds. Solid grey circles indicate intermediate (saddle-node) states. (C) Zeros indicated by solid circles corresponding to seven stable phase-locked states, in the eight spikes bursting HCO at $V_{\mathrm{K2}}^{\mathrm{shift}} = -0.024$, in the 1D stability diagram.

and the barriers corresponding to the unstable states in the leech HCO network. This diagram allows one to identify the most robust phase-locked state by the depth and width of the wells. The steepness of a potential well yields the rate of convergence to the corresponding phase-locked state. This figure also shows that fast convergence to the in-phase ($\Delta\phi^* = 0$) state does not make it the most robust, as its basin is not as deep as those of other stable phase-locked states.

The comparison of figures 4.7A and 4.7B with the corresponding four spikes bursting trace (figure 4.9A), suggests that there is a *(direct) correlation between the number of spikes per burst and the number of stable phase-locked states.* To support the hypothesis we present figure 4.7C showing a similar 1D stability diagram for the eight spikes bursting trace (figure 4.9C): now the leech HCO possesses seven attractors corresponding to the stable phase-locked states. The relation between number of spikes and that of phase locking is still consistent because there are only six spikes that fall in the range $0 \leq \Delta\phi \leq 0.5$ and the anti-phase state is located at $\Delta\phi = 0.5$, which has switched stability.

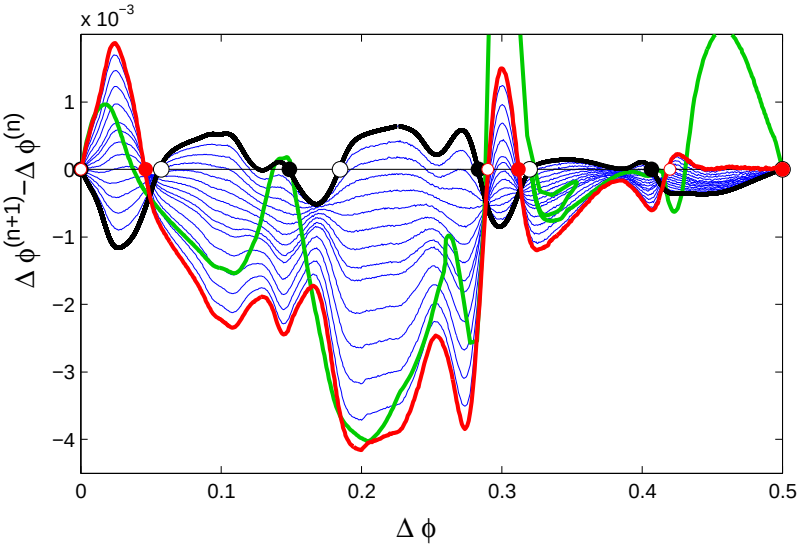

Figure 4.8. Average phase-lag change per burst cycle for various levels of excitation in the synapses. Synaptic reversal potential, E_{syn}, is varied from -0.0625 (black, inhibitory case) to 0.0625 (red, excitatory case) at increments of approximately 0.009. For the green curve $E_{syn} = 0.5$. Open and closed circles represent unstable and stable states.

Based on the qualitative examination of the stability of the fixed points for the phase lags, together with the quantitative observation, it is hypothesized that *spikes do matter*

for the emergence of multiple phase-locked states. The number of spikes per burst does yield an estimate for the number of phase locked states. However, complexity of the spike interactions due to timing and irregularities of the spike characteristics, slow convergence due to weak coupling and the sensitivity of the two-time scales bursting solutions may cause inaccuracy in some models. Moreover, multistability of weakly coupled HCO becomes harder to describe properly as the duty cycle becomes greater, resulting in a long burst train with a larger number of spikes (figure 4.9G-H). Meanwhile, the attraction basins of the phase locked states become narrower and less clearly identifiable, which means that accurate numerical simulations would require unrealistically high resolution.

Excitations instead of inhibitions in the same network configurations often reverses the stability of steady states [33]. So, multistability is expected to exist for excitatory coupling as well but with different phase-locked state being stable. This hypothesis is investigated by gradually raising the synaptic reversal potential, the result of which is shown in 4.8. Stability does switch however non-linear effects shift the locations for some. Thus far, the most tractable cases are presented, and next, an alternate way of thoroughly examining multistability is presented. This method reduces the problem of finding and characterizing stability of phase-locked states to studies of 1D Poincaré return mappings.

4.1.3 Phase return maps

Identifying multiple phase-locked states of the bursting HCO can effectively be reduced to that of finding stable fixed points in 1D Poincaré return mappings defined as: $\Delta\phi^{(n)} \to \Delta\phi^{(n+k)}$, where k is the degree of the mapping. For a non-stationary phase lag, either $\Delta\phi^{(n+k)} > \Delta\phi^{(n)}$ or $\Delta\phi^{(n+k)} < \Delta\phi^{(n)}$ for $k = 1$, but the change is small because of the "continuity" condition mentioned earlier: the case of the weak coupling, which results in slow and smooth dependence of $\Delta\phi^{(n)}$ on the burst cycle number n (figure 4.1A). As a result, the slope of the mapping at a stable fixed point is $1-\epsilon$ (for k-degree mapping the slope $(1-\epsilon)^k \to 0$) and at an unstable fixed point it is $1+\epsilon$ (k-degree slope $(1+\epsilon)^k \to \infty$). Hence, the integer k may be chosen relatively large for the basins of attractions to be well identified. Specific values of k depend on the individual cell model in question as they have distinct rates of the convergence to the phase-locked states. So, $(k-1)$ is

the number of successive burst cycles skipped in the traces to generate the mappings. By choosing the degree to be k, the mapping reveals robust phase-locked states that are represented by stable fixed points, located at intersection points of the flat sections (slope 0) of the mapping graph with a 45-degree line. Due to the large values of k, the unstable fixed points corresponding to the threshold separating the attraction basins reside at the discontinuity points (slope ∞) of the mapping graph.

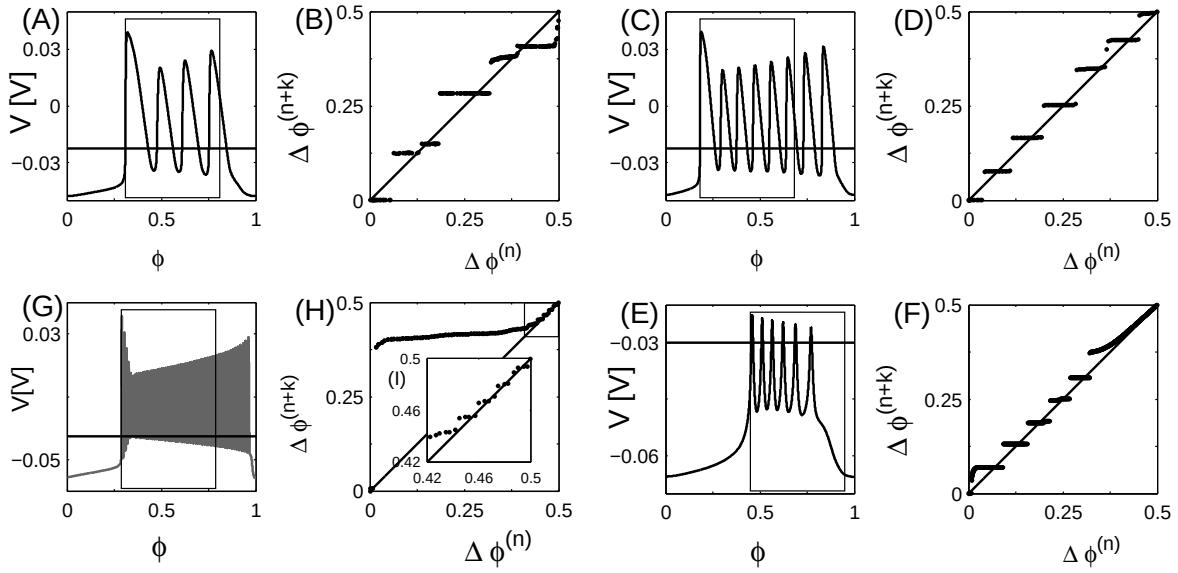

Figure 4.9. Mappings and reference bursts for leech, β-cells, and purkinje HCOs. Bursting cycles generated by the HCO composed of the leech heart interneuron models (panels A and C), and the Sherman models (E) and the Purkinje cell models (G). Overlaid boxes indicate the reference half-period frames defining the spikes that effectively determine the number of phase-locked states in the networks; the horizonal lines set the synaptic thresholds in the HCOs. Panels B, D, F, and H show the corresponding 1D return mappings: $\Delta\phi^{(n)} \to \Delta\phi^{(n+k)}$ of degree k (k = 345, 40, 80 and 35, reps.). (B) and (D): Four and seven stable fixed points in the mapping imply the coexistence of the same number of phase locked states in the bursting leech heart HCOs ($g_s = 0.005$). (E-F): The Sherman model HCO ($g_s = 0.001$) generating six-spike bursting possess the same number of stable fixed point in the mapping. (E) Zoom of the mapping (H) for the the Purkinje cell HCO ($g_s = 0.001$) generating 62-spikes burst trains reveals multiple phase locked states within [0.4, 0.5] range accumulating to anti-phase bursting.

Figure 4.9 presents four pairs of panels each representing bursting rhythms and the corresponding return mappings for the four HCOs under consideration: two with leech heart interneurons with varying duty cycles and one each with Sherman pancreatic β-cells and Purkinje neurons. Panels A-B and C-D depict, respectively, the voltage traces and

the mappings $\Delta\phi^{(n)} \to \Delta\phi^{(n+k)}$ of degrees $k = 345$ and $k = 40$ for the weakly coupled leech HCOs, which robustly produce four and eight spikes per bursting cycle. Panels E-F and G-H are for the HCOs made of the Sherman pancreatic β-cell models, and the Purkinje neuron models, respectively. The frames overlaid on top of the bursting traces denote half-period windows, $0 \leq \phi \leq 0.5$, with the spikes determining the number of phase-locked states. By construction, the phase lag, $\Delta\phi$ is symmetric about the half-period point such that the phase lags outside and inside of the half-period frame are equivalent. This implies that only the spikes within the frames are critical for spike interactions leading to phase-locked states.

Figure 4.9 suggests that the *HCO models under consideration possess the same universal properties, which are due to spike interactions contributing to the emergence of multiple phase-locked states.* There are some distinctions as well, for example, wide asymmetric spikes produced non-homogeneously by the leech heart interneuron model can result in more subtle attraction basins and less robust phase-locked states, including meta-stable states near saddle-node equilibria (figure 4.9) or tangent fixed points (figure 4.9). Those meta-states have vanished and phase-locked states gain robustness, as the number of spikes per burst becomes larger. Furthermore, narrow symmetric spikes produced evenly by the bursting Sherman model HCO contribute to the occurrence of robust phase-locked states with well defined (separated) basins of attraction (see figure 4.9E-F). Remarkably, the number of the spikes occurring within the half-period windows in the leech heart and Sherman β-cell HCOs accurately determines the number of coexisting stable phase-locked states.

The Purkinje model generates long bursts with multiple, nearly instantaneous spikes at the chosen parameter values. Because of that, it is hard to identify a large number of all phase-locked states with rather narrow attraction basins in the weakly coupled ($g_{\text{syn}} = 0.001$) HCO case due to slow convergence. To take fewer spikes into consideration, the synaptic threshold Θ_{syn} is lowered so that spikes occurring closer to the end of the burst cycle can actually cross it (figure 4.9G). As a result, the corresponding Poincaré mapping $\Delta\phi^{(n)} \to \Delta\phi^{(n+k)}$ (here $k = 80$) has an array of fixed points within the range, [0.4, 0.5], near the phase-locked state corresponding to anti-phase bursting produced by

the HCO. Additionally, this demonstrates the significance of the choice for the synaptic threshold in modeling studies of larger network models, such as specific central pattern generators that are often comprised of several HCOs.

In this section *it is demonstrated how various intrinsic properties of the HCOs may determine the number of co-existing phase-locked states.* These properties include correlations between the number of spikes and the temporal characteristics of bursting, such as the spike frequency, duration and duty cycles, as well as the level of the synaptic threshold. While the strength of the synaptic coupling modulates the amplitude of the synaptic current, and hence influences the spike interaction, the simulations suggest that variations of the coupling strength do not essentially influence the number of stable phase-locked states as long as the coupling remains weak, which in turn guarantees the relatively slow convergence to a phase locked state. A significant increase in the coupling strength makes most phase-locked states disappear so that anti-phase bursting will solely persist in the HCO, which is the general convention.

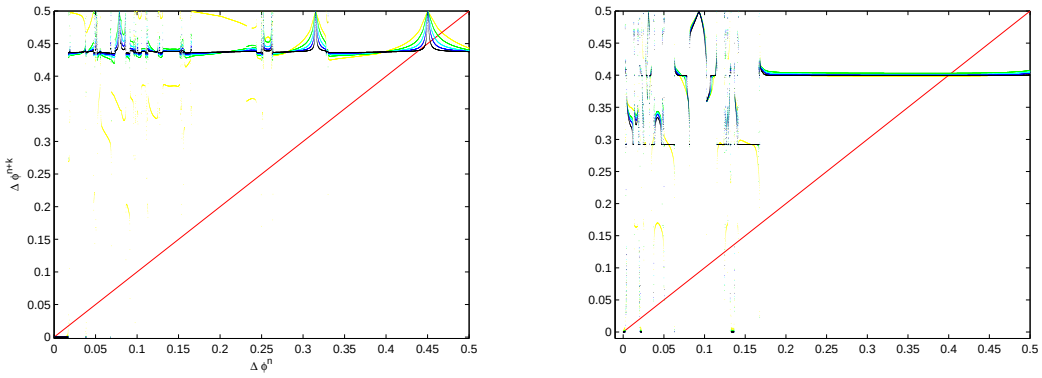

4.10.1 4.10.2

Figure 4.10. Phase return maps for the leech HCO with stronger coupling conductances, $g_s = 0.4$ (4.10.1), and constant IPSPs, that is, $I_{syn} = \bar{g}_s \Gamma(V_{pre} - \Theta_{syn})$ shown in (4.10.2). Horizontal and vertical axes represent phase-lags at the beginning ($n = 1$) and after k, number of cycles, respectively. Colors yellow, green, cyan, blue and black represent increase in k, showing transitions.

A Sequence of phase return maps is useful for studying the phase-locked states of strongly coupled HCOs. Figure 4.10.1 shows mappings for a strongly coupled leech HCO for a number of degrees $k = 1, 2, 3, 4, 5$ (corresponds to yellow, green, cyan, blue and black

dots). Most phase-lags converge to one of two attractors: in-phase synchrony with small basin of attraction and a phase-locked state at $\Delta\phi = 0.43$ with large basin of attraction. Due to strong coupling convergence is quite fast, so sequential degrees of the mapping aids one to visualize the transition to phase-locked states and reveal the fractal nature of the attraction basins.

Phase return maps are plotted in similar fashion for *a synaptic paradigm that is activity independent* (figure 4.10.2). In all other cases synaptic currents depend on the post-synaptic membrane potential ($V_{post} - E_{syn}$) which correlates with the activity of the post-synaptic neuron. This figure reveals the role of duration of inhibition as the activity dependent term that modulates the amplitude of the inhibition is removed. Multistable phase-locked states seems to be emerging but in a discontinuous fashion. Further investigation is necessary to elucidate the observed behavior.

4.2 Strongly coupled networks: stable in-phase bursting

Strong inhibition is defined through coupling that is sufficiently strong to establish anti-phase bursting rapidly, indicated by the convergence rate of the phase-lags (see figure 2.7). The rapid transitions appear as non-smooth time evolution of phase-lags leading to anti-phase bursting. This occurrence precedes or coincides with the hold-and-release mechanism (due to a saddle-node bifurcation) [56], which happens to be functionally similar to synaptic release mechanism, common for relaxation oscillator-type spiking neurons [19, 34, 48]. The hold-then-release mechanism implies that the active pre-synaptic neurons temporarily lock down the inactive post-synaptic cell at the hyperpolarized state during the half-oscillator bursting cycle. Fast inhibition implies that as soon as the active neuron ceases firing and becomes inactive, the other cell is released from inhibition, so they switch roles to produce the second half-oscillator bursting cycle. This cyclic switching between active and inactive phases in the HCO gives rise to highly robust anti-phase bursting. The details on emergent anti-phase rhythms in HCOs made of bursting neurons can be found in [64] and the references therein.

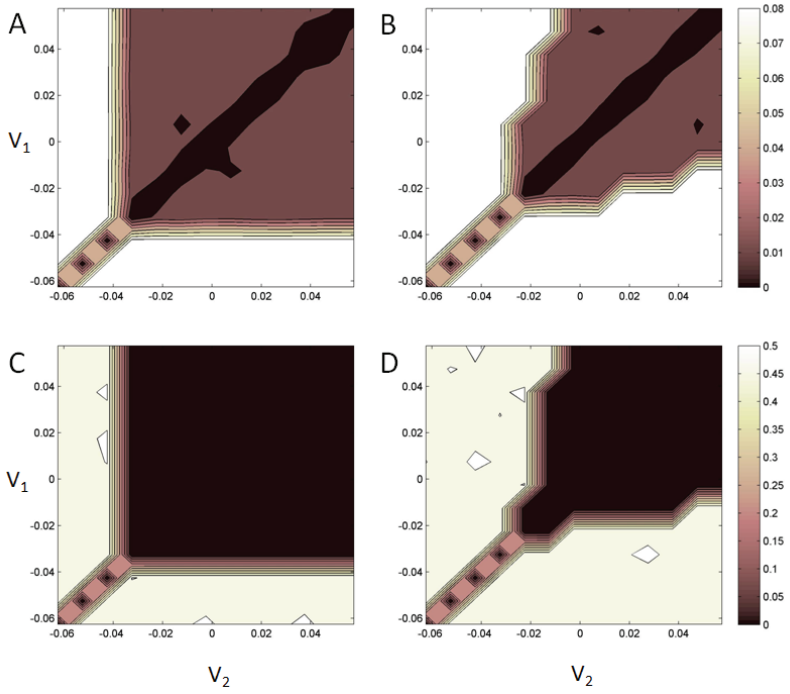

Figure 4.11. Biparametric (Θ_{syn}, g_{syn})-diagrams depicting stability zones (dark) of in-phase bursting in the strongly coupled leech HCO after hold-and-release mechanism has engaged. (A-B) has the same color bar, which depicts maximum absolute deviation in V without transients (spike synchrony); (C-D) shares the color bar for burst synchrony.

In-phase synchrony is possible despite strong inhibitions that establish the hold-and-release mechanism (see figure 4.11). When the coupling is strong and the initial conditions of bursting cells are set so that one cell is active (above the synaptic threshold) while the other is inactive, then fast non-delayed reciprocal inhibition leads ultimately to anti-phase bursting in any HCO, independent of the choice of models of individual bursters and fast synapses. Once achieved, anti-phase bursting remains highly resistant to external voltage perturbations; however, this is not true when long [periodic] inhibition is forwarded to both cells from an external source. As shown in [56], this external inhibition establishes in-phase synchronization in the HCO.

In the previous section, we have stressed that the coexistence of multiple phase-locked states is a peculiar paradigm of the weakly and reciprocally inhibitory coupled HCO made of identical cells. Increasing the coupling strength makes most, but not all, phase-locked states disappear eventually. Nevertheless, bistability can be seen for a wide range of coupling strength as shown in the figure 4.11. Both weakly and strongly coupled

HCOs exhibit anti-phase bursting generally, but the emergent mechanisms are different: a fragile balance between spike timing and IPSCs in the weak coupling case and the robust hold-then-release mechanism in the strong coupling case.

A feature of the strong coupling is the robustness of in-phase bursting that coexists with anti-phase bursting [72]. In-phase bursting emerges over a wide range of dispersed initial conditions chosen within the spiking phase of both cells. Initial conditions corresponding to the activity of one cell and inactivity of the other lead to the emergence of anti-phase bursting via the above hold-then-release mechanism [56]. In 3, it is demonstrated that the impact of inhibition on the bursting cells drastically depends on whether both cells are above the synaptic threshold, Θ_{syn}. More specifically, the variational equations for the stability of synchronized bursting is analyzed, which showed that inhibition instantaneously switches from desynchronization to synchronization as long as both cells become active. That is, if both bursting cells are initially active in the spiking phase of bursting, the inhibition, instead of desynchronizing them, will force the cells' states to come together resulting in stable synchronized bursting.

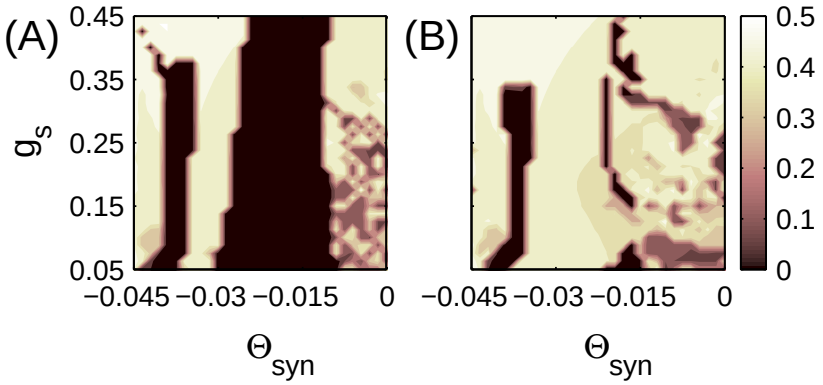

Figure 4.12. Bistability revealed in the (Θ_{syn}, g_s)-biparametric plane for a leech HCO. (A) and (B) only differs in initial conditions. Color bar indicates phase-lags in the terminal bursts after at least 100 seconds.

The synchronizing effect of the fast inhibition is specifically due to *spike interactions of the cells during the active phase of bursting.* This property is linked to the presence of two competing, desynchronizing and synchronizing, synaptic terms in the variational equations 2.14. That is, whenever one cell gets close to the threshold Θ_{syn}, the other

cell receives a short-term desynchronizing kick that causes the divergence between the cells. However, when both cells rise above the threshold, the inhibition switches its role and the cells converge. In this respect, inhibition acts as excitation during the time interval of simultaneous cell activity when both cells are above the synaptic threshold. This synchronization property of inhibitory bursting cells with spikes is in contrast with the HCO made of cells exhibiting spike-free relaxation-type bursting, such as plateau-bursting where the fast inhibition carrying only desynchronizing effects makes stable synchrony impossible.

4.2.1 Generic coexistence of in- and anti-phase bursting

In this section, it is demonstrated that in-phase bursting, co-existing with anti-phase bursting, is a generic property of the HCO, composed of endogenously bursting (nearly identical) neurons, reciprocally coupled by fast non-delayed inhibitory synapses. This property is independent from the model of the fast non-delayed inhibition, be it the instantaneous Heaviside or FTM synapse or a dynamical synapse with the synaptic constants comparable with the duration of the presynaptic spike.

In what follows, the stability and robustness of in-phase bursting with respect to transversal perturbations is examined. More specifically, how the shape of the attraction basin of in-phase bursting varies along the in-phase bursting orbit is investigated. To do so, first one parameterizes the bursting cycle with respect to a phase, defined on modulo 1, as described in the previous section. Next, the in-phase bursting cycle is discretized with a mesh, comprised of reference phase values (see figure 4.13A). Each reference phase is employed to identify a local basin of attraction by gradually advancing, $\Delta\phi > 0$, or delaying, $\Delta\phi < 0$, the initial phase of the perturbed or the non-reference member of the HCO. In the remaining panels of figure 4.13, the initial perturbations, $\Delta\phi$, that result in spike and/or burst synchrony are plotted against phase, ϕ, for the leech HCO described by the four models given in 2.

The shaded regions in the figure 4.13 B-H panels, represented by the largest deviations of the phase perturbation, $\Delta\phi$, reveal that the width of the "synchronization band" varies with the phase; it is maximized during the active or spiking period and

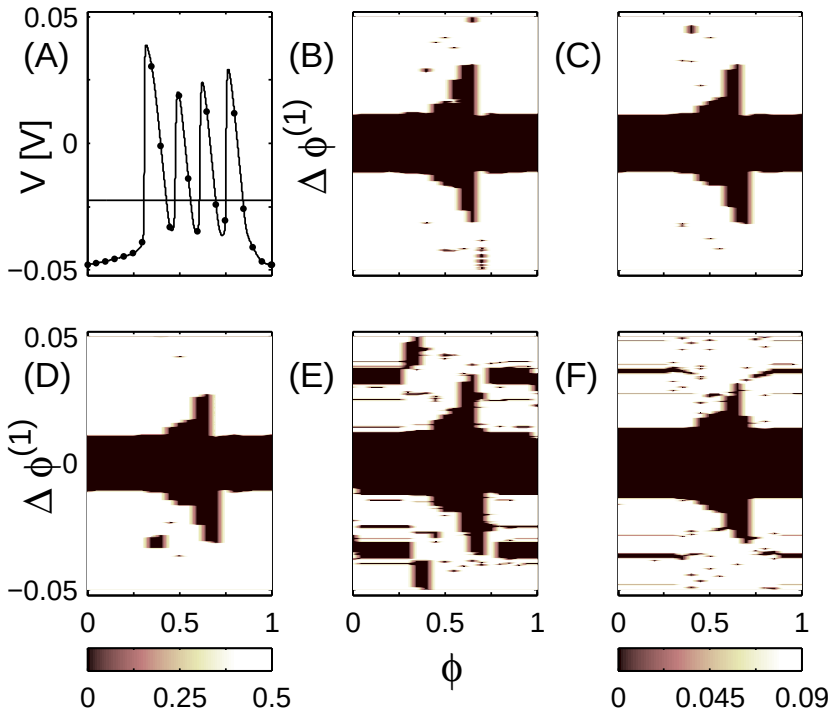

Figure 4.13. Phase dependent synchronization zone along bursting orbit in leech HCOs with various synaptic paradigms. (A) Bursting cycle of the leech heart HCO at $g_s = 0.4$ is phase-parameterized on the interval [0, 1]: dots indicate some reference phases used for identifying the attraction basins of in-phase bursting. The horizontal line across the spikes sets the level of the synaptic threshold $\Theta_{syn} = -0.0225$. Attraction basins of the in-phase state plotted against the phase along the bursting cycle for four models of inhibitory synapses: (B) Heaviside, (C) FTM coupling; (D) heterogeneous FTM coupling with $g_s^{(12)} = 0.4$ and $g_s^{(21)} = 0.44$; (E) α-dynamical synapse; (F) leech heart dynamical synapse. All cases reveal that the widest synchronization zone occurs during the tonic-spiking period of bursting, while quiescent period yields a narrow basin. In all panels the range of $\Delta\phi$ is scaled between $[-0.05, 0.05]$. Color bars represent degree of phase synchrony (left) or spike synchrony (right).

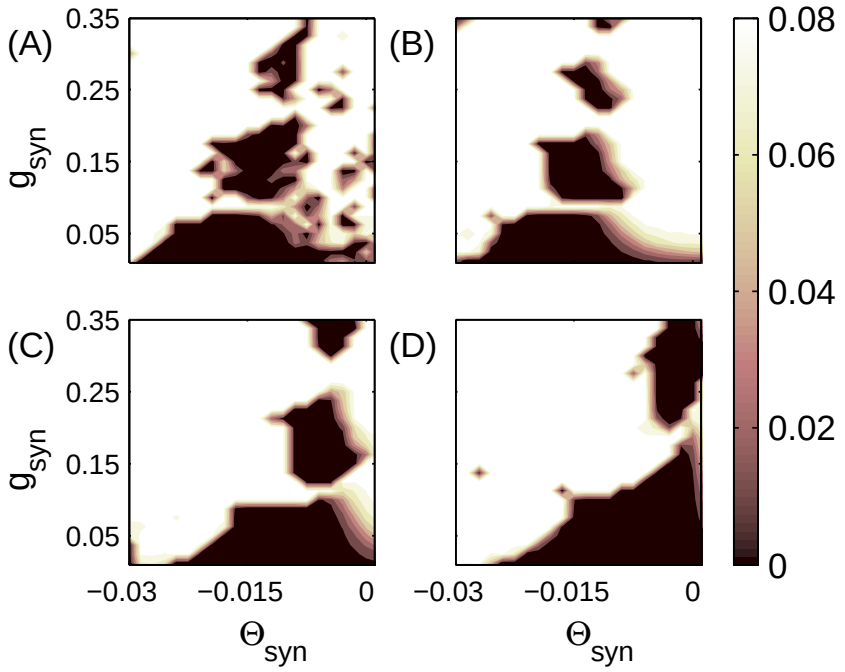

Figure 4.14. Biparametric (Θ_{syn}, g_{syn})-diagrams depicting stability zones (dark) of in-phase bursting in the leech HCO with inhibitory coupling due to (A) the Heaviside function based synapse; (B) the FTM coupling; (C) the α-dynamical synapse; and (D) the leech heart dynamical synapse. Color bar showing the maximal difference in the voltage values between the cells: zero for in-phase bursting and 0.08 for anti-phase bursting. The parameters are $\mathrm{V}_{\mathrm{K2}}^{\mathrm{shift}} = 0.02$, $I_{\text{app}} = 0.006$, $\bar{g}_{\mathrm{Na}} = 160$, $\tau_{\mathrm{K2}} = 0.9$.

shrinks during the quiescent period. For larger initial phase mismatches, the cells of the HCO will settle in anti-phase bursting. Figure 4.13 also demonstrates that all selected models of inhibitory synapses agree both quantitatively and qualitatively. Furthermore, as expected, longer lasting inhibitory inputs of the α-dynamical (2.10) and leech heart dynamical synapses (2.11) (see figure 2.1) ensure some wider synchronization zones. Indeed, beyond the critical values after which the synapse is considered slow or

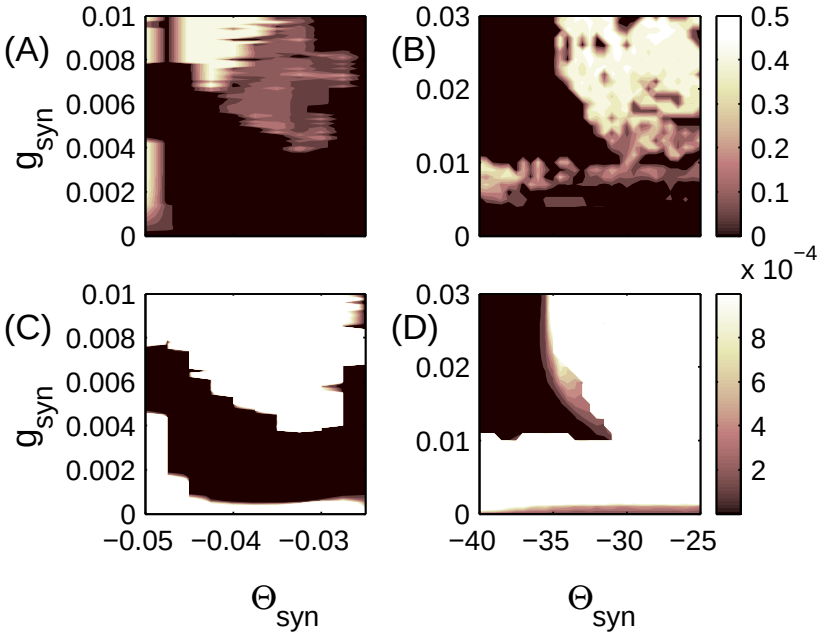

Figure 4.15. Biparametric (Θ_{syn}, g_{syn})-diagrams depicting stability zones (dark) of in-phase bursting in the pancreatic-β (A,C) and purkinje HCOs (B,D). Color bars represent phase-lags, same number of intervals in large and small scales, $(0, 0.5)$ and $(0, 0.001)$, respectively. In-phase synchrony begins with strong enough coupling. Note that shaded regions that are white in bottom panels must be at least phase-locked at 0.001.

slowly decaying in time (figure 3.12), anti-phase bursting becomes non-observable, thus leaving in-phase bursting as the only stable state; this is a classic result [33]. On the contrary, when synapses are fast, anti-phase bursting largely dominates over much weaker in-phase bursting in the inhibitory HCOs (2.6). In-phase bursting necessarily requires close initial burst overlapping. Based on the analysis done in the previous section, it is inferred that spike interactions bound the attraction basin of in-phase synchrony.

In addition to variations in the level of synaptic threshold, Θ_{syn}, that of the synaptic strength, g_{syn}, is used to examine the synchronization properties of in-phase bursting

in strongly coupled HCOs. Figure 4.14 presents bi-parametric sweeping of (Θ_{syn}, g_{syn})-bifurcation diagram for in-phase bursting in the leech heart HCO and figure 4.15 presents those for β-cell and Purkinje HCOs. Leech models are explored with the four selected models of synapses. In the diagrams, shaded areas correspond to stability islands of in-phase bursting. For the given leech interneuron model, the synaptic coupling with g_{syn} exceeding 0.02 is considered strong as it leads right away to robust anti-phase bursting via the hold-and-release mechanism [56].

The HCOs possess the largest stability islands where it can exhibit in-phase bursting within the plausible range of values for the synaptic threshold, $[-0.015, -0.005]$V for leech, $[-0.05, -0.02]$V for β-cell, and $[-40, -30]$mV for Purkinje HCOs. In this range, the synaptic threshold crosses the middle of all of the spikes, which ensures an optimal stabilizing balance for inhibiting synaptic currents to promote in-phase bursting. Lowering or raising the synaptic threshold out of this range makes in-phase bursting less robust as the contribution of the spikes becomes less significant. After the synaptic threshold is lowered below the minimum voltage level of the spikes, the HCO cells begin bursting in anti-phase, generally, similar to pairs of relaxation oscillators [19], such as Morris-Lecar or FitzHugh-Nagumo spiking neurons, where the spike interactions play no functional role.

Chapter 5

EXPERIMENT-BASED CPG ANALYSIS

Behaving animals show correlated neuronal activity in their nervous system. Recordings from single neuron to hundreds of neurons show discriminating activities that are initiated at the onset and terminated at the offset of such behaviors [3, 4, 42]. These observations lead to the question, how are the specific patterns of activities generated and used to control behaviors?

CPGs are small networks of neurons that are experimentally identified as necessary for expressions of behaviors and the core group capable of controlling various aspects of the behavior. Hence, mechanistic understanding of CPG functions is under intense investigation. It is also important for engineering equipments that are dynamically controlled by circuits, such as those in robotics and prosthetics. In this chapter, the role of network configurations of an experiment based CPG for swimming behavior in the marine invertebrate *Melibe leonina* is investigated.

5.1 Minimal configuration networks

The model for leech heart interneurons is used as the individual constituent of the CPG. The model of leech interneurons has been studied extensively and shown both mathematically and experimentally to have the ability to transition into a number of distinct patterns including square wave bursting, spiking, and chaos [26, 29, 51, 73]. In addition, multistability with two or more coexisting stable patterns for this model has been uncovered earlier in this study as well as by other researchers [55]. Due to its versatility and physiological derivation, the leech heart interneuron model is a generic candidate for modeling *Melibe* swim CPG interneurons, for which physiologically accurate model is yet to be identified. Based on experimental recordings, electrical activity patterns and the hypothesis concerning the number of constituent neurons and the nature of connections, a minimal plausible network is investigated.

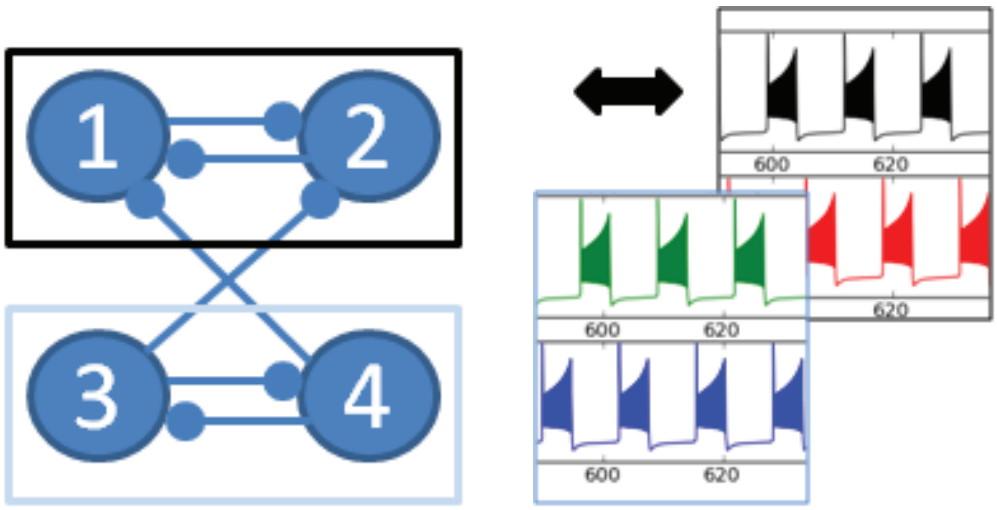

5.1.1 5.1.2

Figure 5.1. Model of an experiment based CPG from *Melibe* with only inhibitory connections (5.1.1), and schematic depiction of the outcomes (5.1.2). The color of the edge of the boxes indicate traces of corresponding HCO. Double headed arrow indicates possible bidirectional movement of each pair of traces with respect to each other, while maintaining anti-phase bursting within each HCO.

Phases and phase relations between bursting interneurons are imperative for representing the repetitive nature of activity patterns of the CPGs. The design of the model was inspired by the specific phase relations seen in experimental voltage traces, see figure 1.9 for example. In-vitro measurements identify a number of half-center oscillators and their anti-phase bursting patterns are apparent [39, 54]. Due to intrinsic symmetry, the network can be treated as two pairs of HCOs, while one pair unidirectionally inhibit the other, see figure 5.1.1. Simulations show that the traces in the HCOs remain in anti-phase, while the phase relation between the pairs shift, see figure 5.1.2.

Phase-locked state that is idiosyncratic of the experimental system is discovered in the simulations, see figures 1.9 and 5.2. Both figures show $\Delta\phi_{12} \approx 0.5$, $\Delta\phi_{13} \approx 0.75$, and $\Delta\phi_{14} \approx 0.25$ measured against $\Delta\phi_{11} \approx 1$, which is scaled by the period of the network cycles. The extra inhibition received by the driven HCO (black box in figure 5.1.1), delays it's activity compared to the driving HCO (blue box in figure 5.1.2). Anti-phase bursting of neurons 1 and 2 corresponds to $\Delta\phi_{12} = 0.5$ and that of neurons 3 and 4 corresponds to $\Delta\phi_{34} = 0.5$. Due to equal periods for all neurons, $\Delta\phi_{34} = \Delta\phi_{13} - \Delta\phi_{14}$, which explains the deviation between these two phase differences. Moreover, the value

of $\Delta\phi_{13}$ indicates that the anti-phase bursting patterns of the HCOs are shifted with respect to the opposite pair only.

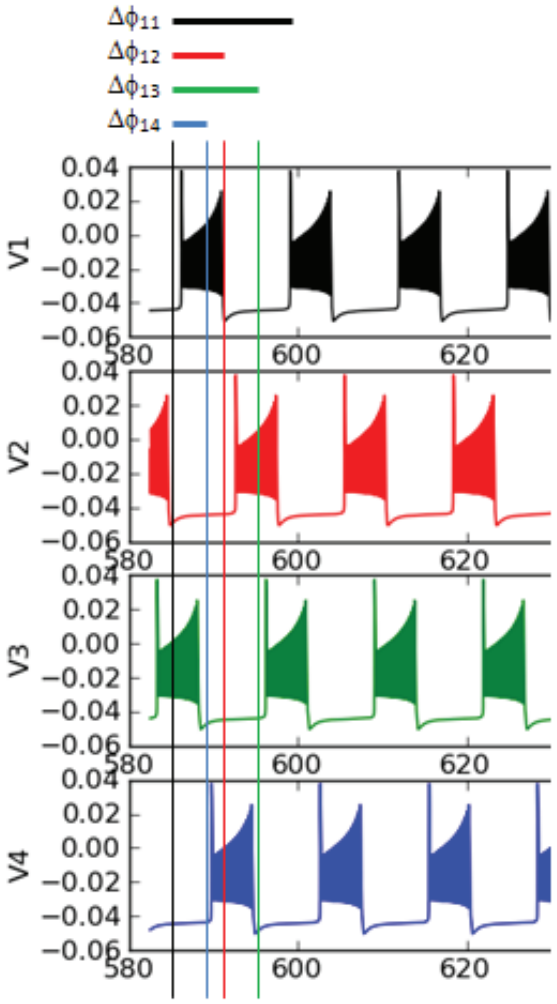

Figure 5.2. Phase-lag definition for experiment based *Melibe* CPG model. The traces are labeled by numbers matching those in (5.1.1), the bars at the top are labeled with phase-lags between neurons given in the subscript and values are scaled by the period of neuron 1, the vertical lines are meant to indicate beginning of a burst in the color matched traces.

The shift between the HCOs can be explained further by the observation that in-phase synchrony between the HCOs seems unstable. When $\Delta\phi_{13} = 0$ or 1, neurons 1 and 3 bursts in-phase and due to half-center configurations neurons 2 and 4 bursts in-phase. Similarly, when $\Delta\phi_{13} = 0.5$ neurons 1 and 4 bursts in-phase along with in-phase synchrony between neurons 2 and 3. However, these patterns are unstable due to the

fact that net inhibition is asymmetric between the pairs 1 and 3, and 2 and 3. Neuron 1 receives more inhibition through two synapses than neuron 3, and so does neuron 2. Hence, phase differences away from in-phase synchrony is preferred by the network such that $0 < \Delta\phi_{13} < 0.5$ or $0.5 < \Delta\phi_{13} < 1$ must contain the stable state.

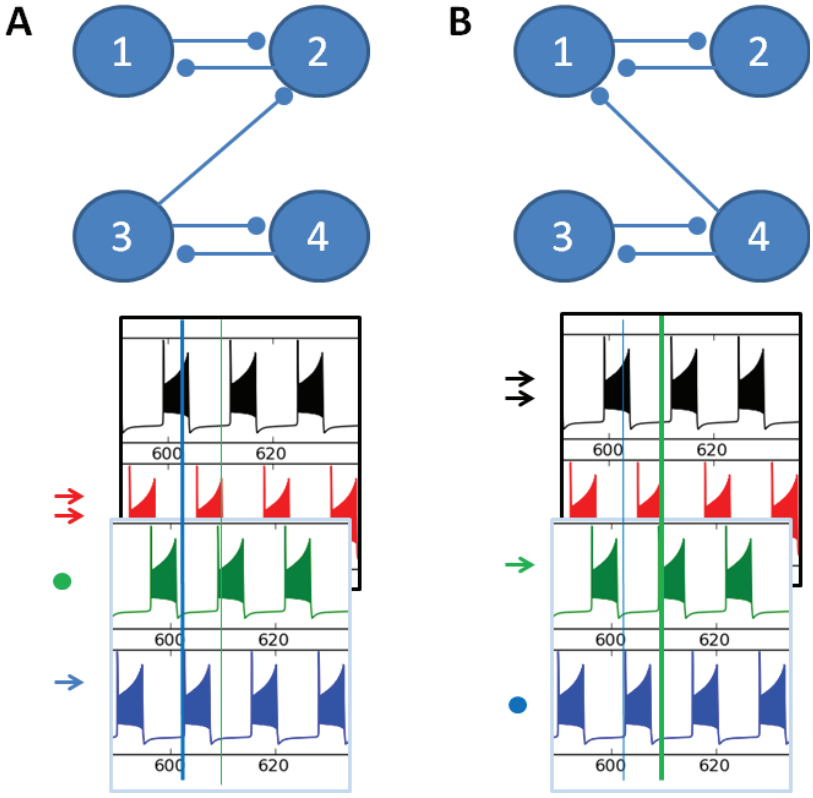

Figure 5.3. Decomposed configurations and their expected traces. Schematic network in each panel correspond to the traces below. Traces colors correspond to neurons 1 (black), 2 (red), 3 (green) and 4 (blue). Green and blue dots indicate driving neurons, and the arrows next to the traces indicate number of synaptic inhibitions. Vertical lines are inserted for visualization of burst alignments.

To answer the question why $\Delta\phi_{13}$ is in the second of the two intervals mentioned above following is suggested. Since only phase-lags with respect to the reference neuron are measured (see chapter 2), $0 < \Delta\phi_{13} < 0.5$ means neuron 3 is delayed whereas $0.5 < \Delta\phi_{13} < 1$ means neuron 3 is advanced. Here the term "delayed" means reference phase of neuron 3 is closest to neuron 1 if following the burst in neuron 1, and the term "advanced" means the nearest burst of neuron 3 is preceding that of neuron 1. The green bursts in figure 5.3 is further (long phase-lags) if measured following the black bursts,

but closer (short phase-advances) if measured preceding the black bursts. This concept is consistent since neurons 1 (black traces) and 2 (red traces) receive more inhibition, neuron 3 should advance compared to neuron 1.

The decomposed configurations shown in the figure 5.3 are expected to be unstable since the top HCO is perturbed asymmetrically. The anti-phase bursting of neuron 1 and 2 are destabilized due to uneven reciprocal inhibition within the pair. As a result, parameter space is explored by variations of symmetric connections as shown in the figures 1.11.1 and 1.11.2. It is found that $\Delta\phi_{13} = 0$ or 1 is achievable if the net inhibition received by each neuron is nearly identical. Figure 5.4 shows that $\Delta\phi_{13} \to \{0, 1\}$ when

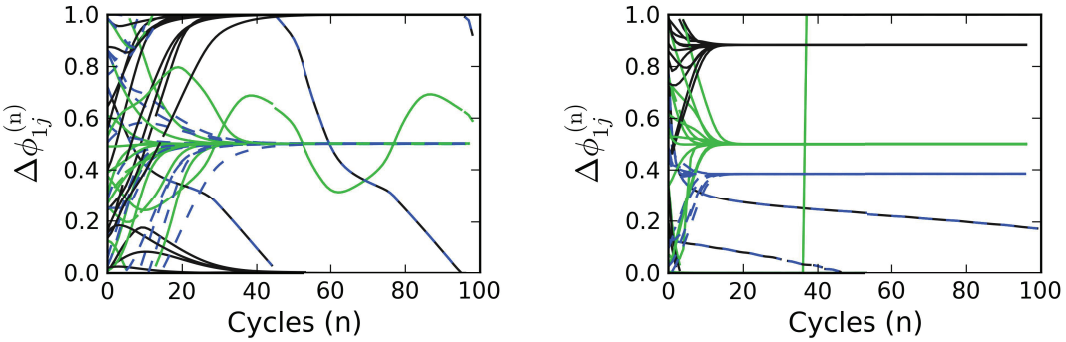

5.4.1 5.4.2

Figure 5.4. In-phase and phase-locked synchrony between HCOs in the *Melibe* CPG. The subscript j stands for 2 (green), 3 (black), 4 (blue) in reference to color coded traces. Synaptic conductances for 5.4.2 are 4-fold that of 5.4.1 for the driving inhibition between the HCOs. Following the coordinate system in 1.11 the coupling conductances are: $(0.001, 0.002, 0.003)$ for 5.4.1.

the net inhibition is balanced, whereas $\Delta\phi_{13} \to 0.87$ when the driving inhibition offsets the net inhibition received by the HCOs. This indicates one mechanism through which the experiment based phase-locked state gets generated is by the up regulation of the inhibitory connections between the half-centers.

Chapter 6

CONCLUSIONS AND FUTURE DIRECTIONS

In summary, the general ability of fast, non-delayed reciprocal inhibition to synchronize bursting cells has been discovered. This synchronizing property is independent from the type of the individual bursting cell and the model of the fast non-delayed inhibition, be it the instantaneous FTM coupling or a dynamical synapse with the synaptic constants comparable with the duration of the presynaptic spike. The exact synergetic features that make stable in-phase synchronization possible are (i) the ability of fast inhibition to switch its impact from desynchronizing to synchronizing when the spikes cross the synaptic threshold, and (ii) the presence of spikes in bursts. It is customary in biophysics to use relaxation oscillators as simplified models of bursting cells where the spikes are smoothed over and ignored.

Reciprocally coupled relaxation oscillators with fast non-delayed inhibition, however, are impossible to synchronize [19, 31]. In light of this, the finding that the addition of spikes to the individual cell model can reverse the role of fast inhibition from desynchronization to synchronization is imperative for biophysical modeling of neuronal networks. It stresses the importance of full-scale detailed models of bursting cells versus simplified models such as relaxation oscillators. The two-cell networks that are studied are the fundamental building elements of large realistic inhibitory networks. The results show that such complex networks with fast inhibitory connections also possess the hidden property to produce the in-phase synchronized rhythm, provided that the individual cells are bursters not spikers. A consequence is the enhanced multistability of complex neuronal networks resulting in richer dynamical information capacity and spatiotemporal neuronal integration.

Moreover, fast non-delayed inhibitory HCOs composed of two endogenously bursting neurons can generate multiple co-existent phase-locked states, in addition to stable anti-phase and in-phase bursting. This is an extension of the previous result that fast

non-delayed reciprocal inhibition synchronizes HCOs, which contrasts with the customary view that reciprocal inhibition has to be slow or time-delayed to establish in-phase bursting. The study shows that the multistability of the HCOs is due to spike interactions and independent of specific choice of models for endogenous square-wave bursters and fast non-delayed synapses. Fast tonic spiking and fast inhibition are the two necessary conditions for multistable bursting to exist in such HCOs.

Bursting HCOs with spikes contrast plateau-like bursting HCOs in their capacity for spike interactions. Plateau-like bursts have slow frequency and smoothed spiking magnitude relative to the plausible range of the synaptic threshold levels, leading to insignificant spike interactions in the HCOs. The *number and temporal characteristics of spikes* are found to determine the number of co-existing phase-locked states in weakly coupled HCOs. Besides, spikes are also attributed to be the necessary component for dynamically establishing the bi-stability in strongly coupled HCOs, where robust anti-phase bursting co-exists with less robust in-phase bursting. This study emphasizes the importance of detailed Hodgkin-Huxley models for credible modeling of larger CPG networks, as opposed to employing relaxation oscillators, which might give rise to simplistic cooperative properties.

The study of multiple phase locking in the HCOs and co-existing dynamical rhythms can help one better understand the origin of multistability and the nature of switching mechanisms between various neuronal rhythms that a multi-functional CPG can generate in response to changes in sensory inputs and external perturbation. Recent experimental studies [24, 37, 42] suggest that leech crawling and swimming can be generated by the same multifunctional CPG, capable of switching between the two locomotor patterns with no change in the types or strengths of connections among the coupled neurons. At the neuronal level, crawling is governed by the command neurons firing in synchrony, whereas the CPG switches to the swimming rhythm when the neurons switch to anti-phase bursting. The duty cycle of in-phase bursting, generating the crawling rhythm, is 7-10 times longer than that of the swimming rhythm [24].

The duty cycle is conjectured to be the main control parameter that determines the rhythms and can trigger the switching between the rhythms [55]. The study of the

spike interactions, whose number and frequency are controlled by the duty cycle, together with previous studies of duty-cycle induced phase locking in larger inhibitory networks [56, 64, 72], promise to shed light on the genesis of switching mechanisms for emergent bursting patterns in real multifunctional CPGs and their realistic models. Investigation of the mechanism that causes particular phase-locked states in the four-neuron CPG and the exploration of parametric regime for sensitivity, and emergence of additional phase-locking in the system would broaden the current understanding of multifunctional CPGs.

In the future, there are number of avenues that may be explored. Brain functions of vertebrate animals are thought to result from neuronal networks similar to CPGs [74]. In addition to inhibitory, excitatory synaptic coupling with various time scales, and networks with direct electrical connections through gap junctions, neuromodulatory effects resulting in synaptic plasticity is common in the mammalian brains. Hence, it is important to incorporate cellular and population level plasticity in the future theoretical investigations of neuron networks [36, 75]. In addition, the CPG models may be enhanced by including extra interneurons of other types, by introducing heterogeneity in network connections, and by increasing physiological fine details that are currently neglected.

REFERENCES

[1] E. Izhikevich, *Dynamical Systems in Neuroscience: The geometry of excitability and bursting.* The MIT Press, 2007.

[2] R. Bertram, M. Butte, T. Kiemel, and A. Sherman, "Topological and phenomenological classification of bursting oscillations," *Bulletin Mathematical Biology*, vol. 57, no. 3, pp. 413–439, 1995.

[3] R. L. Calabrese, "Motor networks: Shifting coalitions," *Current Biology*, vol. 17, no. 4, pp. R139 – R141, 2007.

[4] E. Marder and R. Calabrese, "Principles of rhythmic motor pattern generation," *Physiological Review*, vol. 76, no. 3, pp. 687–717, 1996.

[5] S. Phillips and Y. Takeda, "Frontal-parietal synchrony (phase-locking) in human eeg during visual search," *Neuroscience Reserch*, vol. 65, no. Supplement 1, pp. S192–, 2009.

[6] U. Rutishauser, I. Ross, A. Mamelak, and E. Schuman, "Human memory strength is predicted by theta-frequency phase-locking of single neurons," *Nature Letters*, vol. 464, 2010.

[7] L. E.-Keshet, *Mathematical models in biology.* Random House, 1988.

[8] L. P. Shilnikov, A. Shilnikov, D. Turaev, and L. Chua, *World Scientific Series on Nonlinear Science, Series A: Methods of qualitative theory in non-linear dynamics (Part I).* World Scientific Publishing, 1998, vol. 4.

[9] ——, *World Scientific Series on Nonlinear Science, Series A: Methods of qualitative theory in non-linear dynamics (Part II).* World Scientific Publishing, 2001, vol. 5.

[10] I. Belykh, E. de Lange, and M. Hasler, "Synchronization of bursting neurons: What matters in the network topology," *Physical Review Letters*, vol. 94, no. 18, pp. 188 101–188 104, 2005.

[11] A. Shilnikov and M. Kolomiets, "Methods of the qualitative theory for the hindmarsh-rose model: a case study," *International Journal of Bifurcations and Chaos*, vol. 18, no. 8, pp. 1–27, 2008.

[12] P. E. Paulev and G. Zubieta-Calleja, "New human physiology," *http://www.zuniv.net/physiology/book/index.htm*, 2004.

[13] E. Kandel, J. Schwartz, and T. Jessell, *Principles of Neural Science*. MacGraw-Hill Medical, 2000.

[14] A. Hodgkin and A. Huxley, "A quantitative description of membrane current and its application to conduction and excitation in nerve," *Journal of Physiology*, vol. 117, 1952.

[15] WIKIPEDIA, *http://en.wikipedia.org/wiki/Hodgkin-Huxley-model*.

[16] C. Koch, *Biophysics of Computation: Information Processing in Single Neurons*. Oxford University Press, 2004.

[17] S. J. Etherington, S. E. Atkinson, G. J. Stuart, and S. R. Williams, "Synaptic integration. in: els. john wiley & sons ltd, chichester." *http://www.els.net[doi: 10.1002/9780470015902.a0000208.pub2]*, 2010.

[18] T. Brown, "The intrinsic factors in the act of progression in the mammal," *Proceedings of the Royal Society of London. Series B*, vol. 84, no. 572, pp. 308–319, 1911.

[19] N. Kopell and G. Ermentrout, *Handbook of Dynamical Systems: Chemical and electrical synapses perform complementary roles in the synchronization of interneuronal networks*, B. Fiedler, Ed. Elsevier, 2002, vol. 2.

[20] V. E. Bondarenko, G. S. Cymbalyuk, G. Patel, S. P. DeWeerth, and R. L. Calabrese, "Bifurcation of synchronous oscillations into torus in a system of two reciprocally inhibitory silicon neurons: Experimental observation and modeling," *Chaos*, vol. 14, no. 4, pp. 995–1003, 2004.

[21] J. W. B. Kristan, "Neuronal decision-making circuits," *Current Biology*, vol. 18, no. 19, pp. R928 – R932, 2008.

[22] K. L. Briggman and J. W. B. Kristan, "Imaging dedicated and multifunctional neural circuits generating distinct behaviors," *The Journal of Neuroscience*, vol. 26, no. 42, pp. 10 925–10 933, 2006.

[23] G. Cymbalyuk, Q. Gaudry, M. Masino, and R. L. Calabrese, "Bursting in leech heart interneurons: Cell-autonomous and network-based mechanisms," *The Journal of Neuroscience*, vol. 22, no. 24, pp. 10 580–10 592, 2002.

[24] W. O. Friesen and W. B. Kristan, "Leech locomotion: swimming, crawling, and decisions," *Current Opinion in Neurobiology*, vol. 17, no. 6, pp. 704 – 711, 2007.

[25] B. J. Copeland and D. Proudfoot, "The turing archive for the history of computing: Turing's neural networks of 1948," *http://www.alanturing.net*, 2000.

[26] G. Cymbalyuk and A. Shilnikov, "Coexistence of tonic spiking oscillations in a leech neuron model," *Journal of Computational Neuroscience*, vol. 18, no. 3, pp. 255–263, 2005.

[27] V. N. Belykh, I. V. Belykh, M. Colding-Joergensen, and E. Mosekilde, "Homoclinic bifurcations leading to the emergence of bursting oscillations in cell models," *The European Physical Journal E*, vol. 3, no. 3, pp. 205–219, 2000.

[28] P. Chanell, G. Cymbalyuk, and A. Shilnikov, "Origin of bursting through homoclinic spike adding in a neuron model," *Physical Review Letters*, vol. 98, no. 13, pp. 134 101–134 104, 2007.

[29] A. Shilnikov, "Complete dynamical analysis of a neuron model," *Nonlinear Dynamics*, 2011.

[30] D. Golomb and J. Rinzel, "Dynamics of globally coupled inhibitory neurons with heterogeneity," *Physical Review E*, vol. 48, no. 6, pp. 4810–4814, 1993.

[31] J. Rubin and D. Terman, "Sychronized activity and loss of synchrony among heterogeneous conditional oscillators," *SIAM Journal on Applied Dynamical Systems*, vol. 1, no. 1, pp. 146–174, 2002.

[32] ——, "Geometric analysis of population rhythms in synaptically coupled neuronal networks," *Neural Computation*, vol. 12, no. 3, pp. 597–645, 2000.

[33] C. van Vreeswijk, L. F. Abbott, and G. B. Ermentrout, "When inhibition not excitation synchronizes neural firing," *Journal of Computational Neuroscience*, vol. 1, no. 4, pp. 313–321, 1994.

[34] X. J. Wang and J. Rinzel, "Alternating and synchronous rhythms in reciprocally inhibitory model neurons," *Neural Computation*, vol. 4, no. 1, pp. 84–97, 1992.

[35] N. Kopell and G. Ermentrout, "Chemical and electrical synapses perform complementary roles in the synchronization of interneuronal networks," *Proceedings of the National Academy of Sciences of the United States of America*, vol. 101, no. 43, pp. 15 482–15 487, 2004.

[36] S. Jalil, J. Grigull, and F. K. Skinner, "Novel bursting patterns emerging from model inhibitory networks with synaptic depression," *Journal of Computational Neuroscience*, vol. 17, no. 1, pp. 31–45, 2004.

[37] K. L. Briggman, H. Abarbanel, and J. W. B. Kristan, "From crawling to cognition: analyzing the dynamical interactions among populations of neurons," *Current Opinion in Neurobiology*, vol. 16, no. 2, pp. 135 – 144, 2006.

[38] R. Calin-Jageman, M. Tunstall, B. Mensh, P. Katz, and W. Frost, "Parameter space analysis suggests multi-site plasticity contributes to motor pattern initiation in tritonia," *Journal of Neurophysiol*, vol. 98, no. 4, pp. 2382–2398, 2007.

[39] A. Sakurai and P. Katz, "Distinct neural circuit architectures produce analogous rhythmic behaviors in related species," *Society for Neuroscience Abstracts*, vol. 37, no. 918, p. 04, 2011.

[40] A. Prinz, D. Bucher, and E. Marder, "Similar network activity from disparate circuit parameters," *Nature Neuroscience*, vol. 7, no. 12, pp. 1345–1352, 2004.

[41] D. A. Baxter, H. A. Lechner, C. C. Canavier, R. J. Butera, A. A. Franceschi, J. W. Clark, and J. H. Byrne, *Oscillations in Neural Systems: Coexisting Stable Oscillatory States in Single Cell and Multicellular Neuronal Oscillators*, D. S. Levine, V. R. Brown, and V. T. Shirey, Eds. Lawrence Erlbaum Associates, 1999.

[42] K. L. Briggman and J. W. B. Kristan, "Multifunctional pattern-generating circuits," *Annual Review of Neuroscience*, vol. 31, no. 1, pp. 271–294, 2008.

[43] J. Rubin and D. Terman, *Handbook of Dynamical Systems: Geometric singular perturbation analysis of neuronal dynamics*, B. Fiedler, Ed. Elsevier, 2002, vol. 2.

[44] T. Lewis and J. Rinzel, "Dynamics of spiking neurons connected by both inhibitory and electrical coupling," *Journal of Computational Neuroscience*, vol. 14, no. 3, pp. 283–309, 2003.

[45] R. Elson, A. Selverston, H. Abarbanel, and M. Rabinovich, "Inhibitory synchronization of bursting in biological neurons: Dependence on synaptic time constant," *Journal of Neurophysiology*, vol. 88, no. 3, pp. 1166–1176, 2002.

[46] M. Rabinovich, P. Varona, A. Selverston, and H. Abarbanel, "Dynamical principles in neuroscience," *Reviews of Modern Physics*, vol. 78, no. 4, pp. 1213–1265, 2006.

[47] M. Dhamala, V. Jirsa, and M. Ding, "Enhancement of neural synchrony by time delay," *Physical Review Letters*, vol. 92, no. 7, pp. 074 104–074 107, 2004.

[48] V. Matveev, A. Bose, and F. Nadim, "Capturing the bursting dynamics of a two-cell inhibitory network using a one-dimensional map," *Journal of Computational Neurosciense*, vol. 23, no. 2, pp. 169–187, 2007.

[49] D. Somers and N. Kopell, "Rapid synchronization through fast threshold modulation," *Biological Cybernetics*, vol. 68, no. 5, pp. 393–407, 1993.

[50] N. Kopell and D. Somers, "Anti-phase solutions in relaxation oscillators coupled through excitatory interactions," *Journal of Mathematical Biology*, vol. 33, no. 3, pp. 261–280, 1995.

[51] A. Shilnikov and G. Cymbalyuk, "Transition between tonic-spiking and bursting in a neuron model via the blue-sky catastrophe," *Physical Review Letters*, vol. 94, 2005.

[52] A. Sherman, "Anti-phase, asymmetric and aperiodic oscillations in excitable cells i. coupled bursters," *Bulletin of Mathematical Biology*, vol. 56, no. 5, pp. 811–835, 1994.

[53] M. A. Kramer, R. D. Traub, and N. J. Kopell, "New dynamics in cerebellar purkinje cells: Torus canards," *Physical Review Letters*, vol. 101, no. 6, pp. 068 103–068 106, 2008.

[54] A. Sakurai, J. Newcomb, J. Lillvis, and P. Katz, "Different roles for homologous interneurons in species exhibiting similar rhythmic behaviors," *Current Biology*, vol. 21, 2011.

[55] J. Wojcik, R. Clewley, and A. Shilnikov, "Order parameter for bursting polyrhythms in multifunctional central pattern generators," *Physical Review E*, vol. 83, no. 5, pp. 056 209–056 214, 2011.

[56] I. Belykh and A. Shilnikov, "When weak inhibition synchronizes strongly desynchronizing networks of bursting neurons," *Physical Review Letters*, vol. 101, no. 7, pp. 078 102–078 106, 2008.

[57] C. Canavier, D. Baxter, J. Clark, and J. Byrne, "Nonlinear dynamics in a model neuron provide a novel mechanism for transient synaptic inputs to produce long-term alterations of postsynaptic activity," *Journal of Neurophsysiology*, vol. 69, no. 6, pp. 2252–2257, 1993.

[58] W. Sherwood and J. Guckenheimer, "Dissecting the phase response of a model bursting neuron," *SIAM Journal on Applied Dynamica Systems*, vol. 9, no. 3, pp. 659–703, 2010.

[59] G. B. Ermentrout and D. H. Terman, *Interdisciplinary Applied Mathematics: Mathematical Foundations of Neuroscience*. Springer.

[60] J. Stewart, *Calculus: Early transcendentals*. Brooks/Cole Publishing, 1995.

[61] D. Jordan and P. Smith, *Nonlinear Ordinary Differential Equations*. Oxford University Press, 1994.

[62] E. Izhikevich, "Synchronization of elliptic bursters," *SIAM Review*, vol. 43, no. 2, pp. 315–344, 2001.

[63] S. H. Strogatz, *Nonlinear dynamics and chaos*. Westview Press, 2001.

[64] A. Shilnikov, R. Gordon, and I. Belykh, "Polyrhythmic synchronization in bursting networking motifs," *Chaos*, vol. 18, no. 3, pp. 037 120–037 133, 2008.

[65] S. Jalil, I. Belykh, and A. Shilnikov, "Spikes matter for phase-locked bursting in inhibitory neurons," *Physical Review E*, vol. 85, no. 3, pp. 036 214–036 225, 2012.

[66] R. Horn and C. Johnson, *Matrix Analysis*, 1999.

[67] G. Tancredi, A. Sanchez, and F. Roig, "A comparison between methods to compute lyapunov exponents," *www.fisica.edu.uy/ gonzalo/lyap-aj.ps*.

[68] A. Wolf, J. B. Swift, and J. A. Vastano, "Determining lyapunov exponents from a time series," *Physica D*, vol. 16, no. 3, pp. 285–317, 1985.

[69] V. N. Govorukhin, *http://www.math.rsu.ru/mexmat/kvm/matds/*.

[70] MATHWORKS, *http://www.mathworks.com/matlabcentral/fileexchange/*.

[71] R. Clewley, W. Sherwood, M. Lamar, and J. Guckenheimer, "Pydstool: a software environment for dynamical systems modeling," *http://pydstool.sourceforge.net*, 2007.

[72] S. Jalil, I. Belykh, and A. Shilnikov, "Fast reciprocal inhibition can synchronize bursting neurons," *Physical Review E*, vol. 81, no. 4, pp. 045 201(R)–045 204(R), 2010.

[73] I. Belykh, S. Jalil, and A. Shilnikov, "Burst-duration mechanism of in-phase bursting in inhibitory networks," *Regular and Chaotic Dynamics*, vol. 15, no. 2, 2010.

[74] A. I. Selverston, "Invertebrate central pattern generator circuits," *Philosophical transactions of the royal society: biological sciences*, vol. 365, 2010.

[75] D. Standage, S. Jalil, and T. Trappenberg, "Computational consequences of experimentally derived spike-time and weight dependent plasticity rules," *Biological Cybernetics*, vol. 96, no. 6, pp. 615–623, 2007.

Appendix A

PARAMETERS

Table A.1. Time scales, capacitance, maximal conductances and reversal potentials for leech heart interneuron

$\tau_{\mathrm{Na}} = 0.0405$ sec	$\bar{g}_{\mathrm{Na}} = 200$ nS	$E_{\mathrm{Na}} = 0.045$ V
$\tau_{\mathrm{K2}} = 0.25$ sec	$\bar{g}_{\mathrm{K2}} = 30$ nS	$E_{\mathrm{K}} = -0.070$ V
$C = 0.5$ nF	$\bar{g}_{\mathrm{L}} = 8$ nS	$E_{\mathrm{L}} = -0.046$ V

Table A.2. Boltzmann functions with parameters for leech heart interneuron

$$
\begin{aligned}
n^{\infty}(V) &= [1 + \exp(-150(V + 0.0305))]^{-1} \\
h^{\infty}(V) &= [1 + \exp(500(V + 0.0333))]^{-1} \\
m^{\infty}(V) &= [1 + \exp\left(-83(V + 0.018 + \mathrm{V}_{\mathrm{K2}}^{\mathrm{shift}})\right)]^{-1}
\end{aligned}
$$

Table A.3. Time scales, capacitance, maximal conductances and reversal potentials for Sherman's pancreatic β-cells

$\tau = 0.02$ sec	$\bar{g}_{\mathrm{Ca}} = 3.6$ nS	$E_{\mathrm{Ca}} = 0.025$ V
$\tau_{\mathrm{s}} = 5$ sec	$\bar{g}_{\mathrm{K}} = 10$ nS	$E_{\mathrm{K}} = -0.075$ V
$\lambda = 1$	$\bar{g}_{\mathrm{s}} = 4$ nS	

Table A.4. Boltzmann functions with parameters for Sherman's pancreatic β-cells

$$
\begin{aligned}
m^{\infty}(V) &= [1+\exp(-83.34(V+0.02))]^{-1} \\
n^{\infty}(V) &= [1+\exp(-178.57(V+0.016))]^{-1} \\
s^{\infty}(V) &= [1+\exp\left(-100(V+0.035245)\right)]^{-1}
\end{aligned}
$$

Table A.5. Maximal conductances and reversal potentials for Purkinje neurons

$\bar{g}_{\mathrm{Na}} = 152$ nS	$\mathrm{E}_{\mathrm{Na}} = 50$ mV
$\bar{\mathrm{g}}_{\mathrm{K}} = 10$ nS	$\mathrm{E}_{\mathrm{K}} = -75$ mV
$\bar{\mathrm{g}}_{\mathrm{Ca}} = 1$ nS	$\mathrm{E}_{\mathrm{Ca}} = 125$ mV
$\bar{g}_{\mathrm{M}} = 0.75$ nS	$\mathrm{E}_{\mathrm{M}} = -95$ mV
$\mathrm{g}_{\mathrm{L}} = 2$ nS	$E_{\mathrm{L}} = -70$ mV

Table A.6. Voltage dependent time scales for Purkinje neurons

$$
\begin{aligned}
\tau_{\mathrm{n}} &= 0.25 + 4.35\exp(-0.1|V+10|) \\
\tau_{\mathrm{h}} &= 0.15 + 1.15[1+\exp(0.0667(V+33.5))]^{-1} \\
\tau_{\mathrm{c}} &= [\alpha_{\mathrm{Ca}} + \beta_{\mathrm{Ca}}]^{-1}, \quad \tau_{\mathrm{M}} = [\alpha_{\mathrm{M}} + \beta_{\mathrm{M}}]^{-1}
\end{aligned}
$$

Table A.7. Voltage dependent time scales for Purkinje neurons: auxiliary function

$$
\begin{aligned}
\alpha_{\mathrm{Ca}} &= 1.6/(1+\exp(-0.072(V-5))) \\
\beta_{\mathrm{Ca}} &= 0.02(V+8.9)/(-1+\exp(0.2(V+8.9))) \\
\alpha_{\mathrm{M}} &= 0.02/(1+\exp(-0.2(V+20))) \\
\beta_{\mathrm{M}} &= 0.01\exp(-0.0556(V+43))
\end{aligned}
$$

Table A.8. Boltzmann functions with parameters for Purkinje neurons

$$
\begin{aligned}
n^{\infty}(V) &= [1+\exp(-0.1(V+29.5))]^{-1} \\
m^{\infty}(V) &= [1+\exp(-0.1(V+34.5))]^{-1} \\
h^{\infty}(V) &= [1+\exp(0.0935(V+59.4))]^{-1} \\
c^{\infty}(V) &= \alpha_{\mathrm{Ca}}\tau_{\mathrm{c}}, \quad M^{\infty}(V) = \alpha_{\mathrm{M}}\tau_{\mathrm{M}}
\end{aligned}
$$

Table A.9. Parameters for Fitzhugh-Rinzel model

$I = 0.3125$	$a = 0.7$
$\delta = 0.08$	$b = 0.8$
$\mu = 0.002$	$c = -0.7$

Appendix B

PSEUDO CODES

To calculate the **Lyapunov exponents**, following steps are followed by Govorukhin [69]. The code is available from Matlab central [70]. There are two functions files: the first function file defines the synchronous trajectory along with variational equations, the second function file integrates the equations provided in the first function file in order to calculate the Lyapunov exponent. **The pseudo code for the first function follows:**

1. Populate A to integrate $x' = Ax$ numerically.
2. Assign first n entries of A with ODEs corresponding to single neuron.
3. Set $V_1 = V_2 = V$ in the synaptic component to ensure evaluation on the synchronous manifold.
4. Allocate $n + 1$ to $n + n^2$ entries of A for the coefficients of variational equations.
5. Obtain n coefficients of each variational from every variational equation.
6. Assign coefficients of the linear part in the variational equations to $A(n + 1)$ ... $A(n + n^2)$.

The second function calculates the **Lyapunov exponents** by finding evolution of unit vectors under the linear transformation given by the variational equations evaluated on the synchronous manifold. The total time is divided into smaller time steps to prevent build up of error. Gram-Schimdt process of orthonormalization resets the unit vectors after every time step. Natural logarithm of the norms of the orthogonalized vectors give the Lyapunov exponents, when averaged over elapsed time. **The pseudo code for the second function follows:**

1. Assign $x(1), x(2)..x(n)$ with initial condition from the synchronous manifold.

2. Assign $x(n+1:n+n) = (1, 0, ..0)$, $x(2n+1:2n+n) = [0, 1, 0..0]$, and so on such that each n-tuple have orthogonal unit vector.

3. Set number of iteration: total time,T, divided by time step, dt.

4. Integrate for first time step.

5. Obtain solution x_{out}.

6. Reset $x(1), x(2)...x(n)$ equal to $x_{out}(1), x_{out}(2)...x_{out}(n)$ for integration in next iteration.

7. Apply Gram-Schimdt process to the remaining output by treating each n-tuple as vectors.

8. Get L_2 norm for each vectors, which give total n scalar values $z(1)...z(n)$.

9. Reset $x(n+1:n+n), x(2n+1:2n+n)...$ with Gram-Schimdt orthonormal vectors.

10. Lyapunov exponents,$\lambda_{1...n}$, after first time step equals $\frac{log(z(1))}{dt}...\frac{log(z(n))}{dt}$.

11. Repeat steps 6 to 11 for the next time step.

12. Lyapunov exponents after this time step equals $\frac{\sum log(z(1))}{\sum dt}...\frac{\sum log(z(n))}{\sum dt}$.

13. Continue the process until $\sum dt = T$, obtain n Lyapunov exponents, $\lambda_{1...n}$, after every time step.

An **alternate method** is also used to calculate the Lyapunov exponents. The linear transformation is used to transform the basis of unit vectors for precisely one period. Then the Floquet multipliers are calculated from the matrix formed by the transformed unit vectors. Natural logarithm of Floquet multipliers, averaged over the period, gives the Lyapunov exponents. **The pseudo code follows:**

1. Set $dt = T$, in the step 4 of second function above, where T is precisely the burst period.

2. Obtain the output x_{out}, and construct the transformed unit matrix, **S**, from each n-tuple numbers from $x(n+1)$ to $x(n+n^2)$.

3. Find the Floquet multipliers, which are the eigenvalues,$\rho_{1...n}$, of the matrix **S**.

4. Apply log, divide the result by the period to get Lyapunov exponents: $\lambda_{1...n} = log(\rho_{1...n})/T$

The process for computing **phase differences** between a pair of neurons records the time at which either neuron crosses a voltage threshold given by the Poincaré section. Subtraction of subsequent times recorded for the same neuron gives the period, while that between different neurons give the time delay, which is scaled by the period to obtain the phase differences. **The pseudo code follows:**

1. Choose one of the neurons as the reference neuron, label its membrane potential as V_1.

2. Integrate the system of ODEs representing the network, record the times when $V_{1...n}$ crosses an auxiliary threshold, Θ_{th}, such that $V'_{1...n} > 0$.

3. Suppose $\{t^{(n)}\}$ is the time sequence obtained for the reference neuron, while $\{s^{(n)}\}$ is that of another neuron.

4. Obtain $T^{(n)} = t^{(n+1)} - t^{(n)}$.

5. Set $\Delta\phi^{(n)} = \min\{|t^{(n)} - s^{(n-1)}|, |t^{(n)} - s^{(n)}|, |t^{(n)} - s^{(n+1)}|\}/T^{(n)}$.

6. Obtain $\{\Delta\phi_{1k}^{(n)}\}$ for every non-reference neuron k.

The process for setting **initial phase differences** uses points from a reference trajectory that are equally spaced in time. Exactly one cycle of burst is chosen from the last cycle of 100s of simulation to avoid the transience. The **phases** are defined by scaling the time steps within the cycle by the total time of the cycle. **The pseudo code follows:**

1. Run the full system of ODEs for 100s.

2. Find the times of last two minima in V for the reference neuron.

3. Use the time difference in step 2 as the period, set of variable values for the second minimum for the simulation in step 4.

4. Simulate for exactly one period, obtain variable values at equal time steps, $dt = 0.0001$s.

5. Obtain sequential indices of the points that are sampled at regular intervals by the above step.

6. Set $\phi = i/L$, where i is a specific index and L is the total number of indices.

7. Set ϕ_{ref} closest to 0.5, assign corresponding state variables as the initial condition for the reference neuron.

8. Select $\phi_{non-ref}$ at regular intervals between 0 and 0.5, assign the corresponding state variables as the initial condition for the non-reference neurons.

9. Initial $\Delta\phi = \phi_{ref} - \phi_{non-ref}$.

The process for **toroidal resetting** corrects the values of $\Delta\phi$ whenever it falls outside of the interval $[0, 1]$. This resetting causes an effect such that the graphs of those trajectories $\{\Delta\phi^{(n)}\}$ appear to end at one boundary and emerge from the opposite boundary. **The pseudo code follows:**

1. If $\Delta\phi < 0$ add $+1$ until $0 < \Delta\phi < 1$. For example, $\Delta\phi = -\delta$ becomes $\Delta\phi = 1 - \delta$, for $\delta > 0$.

2. If $\Delta\phi > 1$ and -1 until $0 < \Delta\phi < 1$.